UC San Diego
UC San Diego Electronic Theses and Dissertations

Title

Effect of Nano-Size on Lithium-Ion Batteries : High Voltage $LiNi_{0.5}Mn_{1.5}O_4$ Spinel and Rechargeable NiO-CuF_2 conversion materials

Permalink

https://escholarship.org/uc/item/6mq9x9jw

Author

Cho, Hyung Man

Publication Date

2015

Peer reviewed|Thesis/dissertation

UNIVERSITY OF CALIFORNIA, SAN DIEGO

Effect of Nano-Size on Lithium-Ion Batteries:
High Voltage $LiNi_{0.5}Mn_{1.5}O_4$ Spinel and Rechargeable $NiO\text{-}CuF_2$ conversion materials

A dissertation submitted in partial satisfaction of the
requirements for the degree Doctor of Philosophy

in

Materials Science and Engineering

by

Hyung Man Cho

Committee in charge:

     Professor Ying Shirley Meng, Chair
     Professor Prabhakar R. Bandaru
     Professor Eric E. Fullerton
     Professor Sungho Jin
     Professor Oleg Shpyrko
     Professor Jan B. Talbot

2015

The Dissertation of Hyung Man Cho is approved, and it is acceptable in quality and form

for publication on microfilm and electronically:

_____

_____

_____

_____

_____

<div align="right">Chair</div>

University of California, San Diego

2015

DEDICATION

To my wife and daughter,

Haemin Park and Emma Eunho Cho

To parents,

Woosik Cho and Gwangja Gong

To my parents-in-law,

Seonggon Park and Oksun Kim

TABLE OF CONTENTS

LIST OF FIGURES

LIST OF TABLES

ACKNOWLEDGEMENTS

I would like to express my gratitude to my thesis advisor Dr. Ying Shirley Meng for providing me all the opportunities to do this research. Through countless advice and encouragement, her guidance has proved to be invaluable. I will never forget her endless passion and concentration for science. I would like to extend my grateful acknowledgement to my other committee members: Dr. Sungho Jin, Dr. Eric E. Fullerton, Dr. Jan B. Talbot, Dr. Oleg Shpyrko, and Dr. Prabhakar R. Bandaru for their time and guidance.

I would also like to acknowledge my collaborators and co-authors in UCSD, with whom I had many useful and stimulating discussions. I'm also grateful to all my group mates in Laboratory for Energy Storage and Conversion (LESC) and all the senior and junior students in UCSD, who have helped and inspired me in many ways.

Chapter 4, in full, is a reprint of the material "Effect of Ni/Mn Ordering on Elementary Polarizations of $LiNi_{0.5}Mn_{1.5}O_4$ Spinel and Its Nanostructured Electrode" as it appears in the Journal of the Electrochemical Society, Hyung-Man Cho, Ying Shirley Meng, 2013, 160, A1482. The dissertation author was the primary investigator and author of this paper. All the experiment and writing were performed by the author.

Chapter 5, in full, is currently being prepared for submission for publication of the material "Effect of Surface Modification on Nano-Structured $LiNi_{0.5}Mn_{1.5}O_4$ Spinel Materials". Hyun-Man Cho, Michael Vincent Chen, Alex C. MacRae, Ying Shirley Meng, The dissertation author was the primary investigator and author of this paper. All the experiment and writing were conducted by the author.

Chapter 6, in full, is currently being prepared for submission for publication of the material "Implementation of stable surface structures; a promising key to solve capacity fading issues for the high-voltage $LiNi_{0.5}Mn_{1.5}O_4$". Hyojung Yoon, Hyung-Man Cho, Danna Qian, Ying Shirley

Meng. The dissertation author was the co-primary investigator and author of this paper. All the experiment parts were performed by the author except EELS and STEM study.

For the last but not least, my deepest gratitude goes to my parents Woosik Cho and Gwangja Gong, and parents-in-law Seonggon Park and Oksun Kim, for their love, patience and never-ending support. I specially thank to my wife, Haemin Park, and my daughter, Emma Eunho Cho for her endless support and encouragement during my Ph.D.

VITA

2008   Bachelor of Science, Pusan National University, Busan, Republic of Korea

2010   Master of Science, Pusan National University, Busan, Republic of Korea

2015   Doctor of Philosophy, University of California, San Diego, USA

PUBLICATIONS

1. **H.-M. Cho**, Y.J. Park, J.-W. Yeon, and H.-C. Shin, "In-Depth Investigation on Two- and Three-Electrode Impedance Measurements in Terms of the Effect of the Counter Electrode" ***Electronic Materials Letters*** Vol. 5, No. 4 (2009) 169.

2. **H.-M. Cho**, Y.J. Park, and H.-C. Shin, "Semi-Empirical Analysis of Time-Dependent Elementary Polarizations in Electrochemical Cells" ***Journal of the Electrochemical Society*** 157 (2010) A8.

3. **H.-M. Cho** and H.-C. Shin, *Analysis of Cell Impedance for the Design of High-Power Lithium-Ion Battery* in *Lithium Batteries: Research, Technology and Applications*, (edt., Greger R. Dahlin and Kalle E. Strom), ***Nova Science***, New York (2010) ISBN: 978-1-61668-517-1.

4. **H.-M. Cho**, W.-S. Choi, J.-Y. Go, S.-E. Bae, and H.-C. Shin, "A study on time-dependent low temperature power performance of a lithium-ion battery" ***Journal of Power Sources*** 198 (2012) 273.

5. D. Qian, B. Xu, **H.-M. Cho**, T. Hatsukade, K. J. Carroll, and Y. S. Meng, "Lithium Lanthanum Titanium Oxides: A Fast Ionic Conductive Coating for Lithium-Ion Battery Cathodes" Chemistry of Materials 24 (2012) 2744.

6. **H.-M. Cho**, and Y. S. Meng, "Effect of Ni/Mn Ordering on Elementary Polarizations of LiNi0.5Mn1.5O4 Spinel and Its Nanostructured Electrode" ***Journal of the Electrochemical Society*** 160 (2013) A1482.

7. A. Ulvestad, **H. M. Cho**, R. Harder, J. W. Kim, S. H. Dietze, E. Fohtung, Y. S. Meng and O. G. Shpyrko, "Nanoscale strain mapping in battery nanostructures" ***Applied Physics Letters*** 104 (2014) 073108.

8. H. Liu, **H.-M. Cho**, Y. S. Meng, and Q. Li, "Engineering three-dimensionally electrodeposited Si-on-Ni inverse opal structure for high volumetric capacity Li-ion microbattery anode" ***ACS Appl. Mater. Interfaces*** 6 (2014) 9842.

9. A. Ulvestad, A. Singer, **H.-M. Cho**, J. Clark, R. Harder, J. Maser, Y. S. Meng, O. G. Shpyrko, "Single particle nanomechanics in operando batteries via lensless strain mapping" *Nano Letters* 14 (2014) 5123.

10. A. Singer, A. Ulvestad, **H.-M. Cho**, J. W. Kim, J. Maser, R. Harder, Y. S. Meng and O. G. Shpyrko, "Nonequilibrium Structural Dynamics of Nanoparticles in LiNi1/2Mn3/2O4 Cathode under Operando Conditions" *Nano Letters* 14 (2014) 5295.

11. A. Ulvestad, J. N. Clark, A. Singer, D. Vine, **H. M. Cho**, R. Harder, Y. S. Meng, O. G. Shpyrko, "In situ strain evolution during a disconnection event in a battery nanoparticle" *Physical Chemistry Chemical Physics* 17 (2015) 10551.

12. A. Ulvestad, A. Singer, J. N. Clark, **H. M. Cho**, J. W. Kim, R. Harder, J. Maser, Y. S. Meng, and O. G. Shpyrko, "Topological defect dynamics in operando battery nanoparticles" *Science* 348 (2015) 1344.

13. **H.-M. Cho**, M. V. Chen, A. C. MacRae, and Y. S. Meng, "Effect of Surface Modification on Nano-Structured LiNi0.5Mn1.5O4 Spinel Materials" (2015) *in preparation.*

14. H. Yoon[1]**, H.-M. Cho[1]**, D. Qian, and Y. S. Meng, "Implementation of stable surface structures; a promising key to solve capacity fading issues for the high-voltage LiNi0.5Mn1.5O4" (2015) *in preparation*.

15. J. K. Seo, **H.-M. Cho**, M. Sina, K. Takahara and Y. S. Meng, "Understanding of the factor affecting the reaction voltage of Li-ion conversion materials" (2015) *in preparation.*

ABSTRACT OF THE DISSERTATION

Effect of Nano-Size on Lithium-Ion Batteries:

High Voltage $LiNi_{0.5}Mn_{1.5}O_4$ Spinel and Rechargeable $NiO-CuF_2$ conversion materials

by

Hyung Man Cho

Doctor of Philosophy in Materials Science and Engineering

University of California, San Diego, 2015

Professor Ying Shirley Meng, Chair

The worldwide energy crisis boosted the development of environmentally benign energy infrastructures where energy storage is one of the key components. Among various energy storage systems, lithium-ion batteries have been attracted a keen interest as the best candidate for maximizing energy efficiency, however current lithium-ion battery technology is still inadequate to satisfy the requirements of advanced applications such as electric vehicles. $LiNi_{0.5}Mn_{1.5}O_4$ spinel materials have been considered as a promising

positive electrode due to its high operating voltage ~ 4.7 V (vs. Li/Li$^+$) and relatively higher energy density (theoretical specific capacity, 146.72 mA h g^{-1}).

In this thesis, elementary polarizations of LiNi$_{0.5}$Mn$_{1.5}$O$_4$ spinel materials with disordered (space group, F d -3 m) and ordered (space group, P 4$_3$ 3 2) structures are quantitatively analyzed to clarify how the differences in crystallographic structure affect the rate performance. In order to increase the active surface area and reduce the diffusion length, the nanowire electrode was prepared via sol-gel based template synthesis. It is proved that nanostructure can improve instant discharging rate with a reduced charge-transfer and diffusion resistances. As a result of maximized surface area, however manganese ions dissolution results in capacity fading over prolonged cycling. Atomic layer deposition on the surface proved an effective surface protection method. Using a combination of X-ray absorption spectroscopy (XAS) coupled with aberration-corrected scanning transmission electron microscopy (STEM), it is found that the atomic structural transformation at the surface is the main source of the Mn dissolution problem on the conventional spinel LiNi$_{0.5}$Mn$_{1.5}$O$_4$ materials. A new synthesis method, Polyol process, is also introduced which does not suffer from the detrimental dissolution problem. As an alternative to the conventional intercalation materials, CuF$_2$ conversion materials are also investigated. NiO coated CuF$_2$ can show the promising rechargeable behavior and its mechanism was disclosed with the help of pair distribution function analysis.

Chapter 1. Introduction

1.1. Lithium-Ion Batteries (LIBs)

Portable electronics continue to drive development of advanced battery systems. The rapid growth of interest in environmental-friendly transportation systems also accelerates the battery research as an energy source of electric vehicles, ships, and aircraft that can be operated with little or no oil consumption and carbon dioxide emission. Lithium-ion batteries (LIBs) are the most auspicious candidates for it, because lithium weighs lightest, holds highest voltage, and greatest energy density of all metals.[1-2] Therefore, lithium-ion batteries highly interest industries and governments to lead abundant research in battery field.

Lithium-ion batteries are closed systems, which contain a positive (cathode) and a negative (anode) electrodes, and a separator containing an electrolyte, as shown in Figure 1.1. In the commercialized lithium-ion batteries, the positive electrodes employ the transition metal oxides which consist of transition metal oxide hosts with specific sites for lithium ions to be intercalated in. The carbonaceous materials, especially graphite, are extensively adopted negative electrodes. These two electrodes are physically disconnected by a porous separator that averts the electric short circuit and allows electrolyte to pass through. Typical electrolyte is an organic solvent and dissociated $LiPF_6$ salts, which provide stable operation range between 0.8 V (vs Li/Li$^+$) and 4.5 V (vs. Li/Li$^+$). Various solvents such as ethylene carbonate (EC), diethyl carbonate (DEC) and dimethyl carbonate (DMC) are utilized in conventional lithium-ion batteries. During the charging process, lithium ions are extracted from the positive electrode, pass through the electrolyte, and

intercalated into the negative electrode. At the same time, electrons flow through external circuit from positive electrode to negative electrode. Thus, active materials in the positive electrode are oxidized, simultaneously the reduction happened in the negative electrode. The opposite reaction happens in discharging process.

The successful development of lithium-ion batteries with high power/energy density relies on minimizing the ionic and electronic resistance related to the battery operation. It is imperative to understand the electrode reaction mechanism which shows the pathway of electrons and lithium ions in active materials. Figure 1.2 illustrates the elementary reaction steps of a general electrode reaction. When the electrochemical reaction happens, each elementary reaction step at the interface of the active materials can be roughly classified as follows: I. Mass transfer reaction due to lithium ion transport through the porous separator wetted with the electrolyte, II. Surface reaction that lithium ion transport through the surface film, such as the solid electrolyte interphase (SEI), on the active materials, III. Electron (charge) transfer reaction at the interface between the electrolyte and active materials, and IV. Diffusion step of lithium ion inside the active materials. Interfacial charge transfer and solid-state lithium diffusion through the active materials are usually the most difficult reaction steps in the lithium insertion/extraction process. Each materials, however, has different properties. Suitable characterization of active materials can develop the successful design strategy for advanced lithium-ion battery electrode materials.
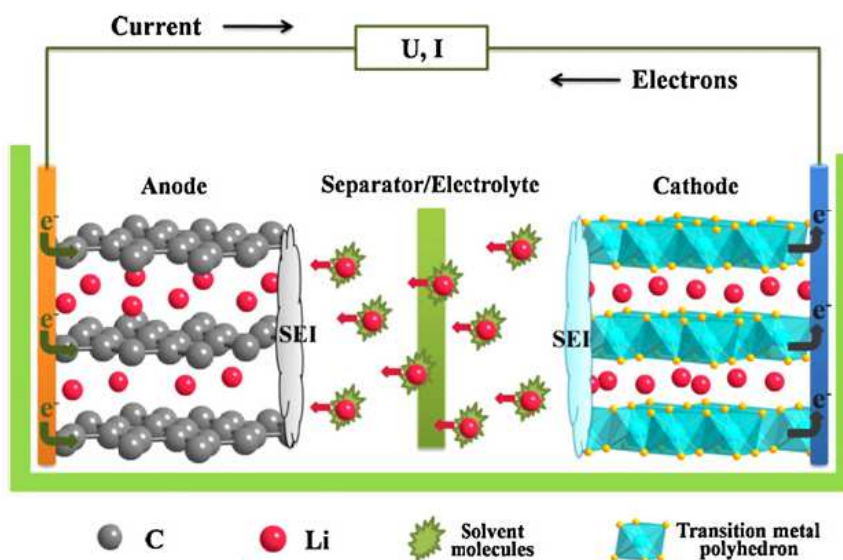
Figure 1.1 Schematics for the operating principle of lithium-ion battery (charging)[3]
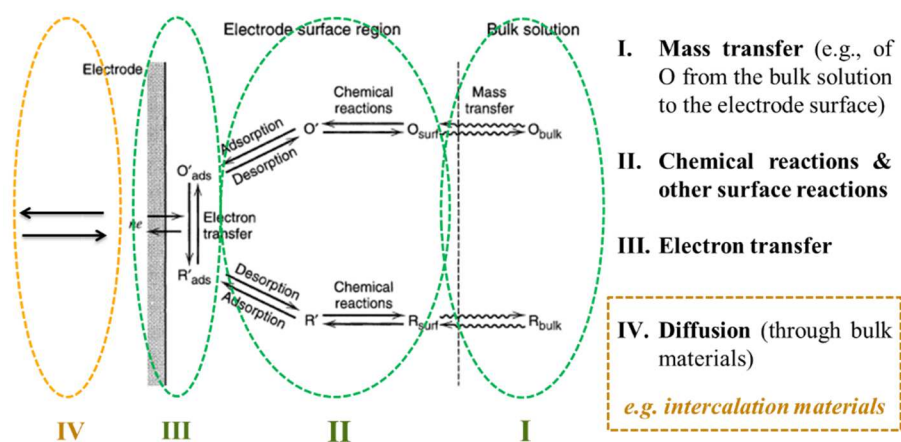
Figure 1.2 Elementary reaction steps of a general electrode reaction

1.2. High-Voltage Spinel Materials, $LiNi_{0.5}Mn_{1.5}O_4$

Selecting electrode materials has to meet various criteria: cost, energy, power, cycle life, and safety. $LiNi_{0.5}Mn_{1.5}O_4$ spinel materials have attracted particular attention as a promising candidate for replacing the current positive materials commercially available, for example, $LiCoO_2$, of lithium-ion batteries. Spinel $LiNi_{0.5}Mn_{1.5}O_4$ provides a high-voltage plateau at ~ 4.7 V (vs. Li/Li^+), which is ascribed to the redox potential of the $Ni^{2+/3+}$ and $Ni^{3+/4+}$ couples. Thus, it enables relatively higher energy density (theoretical specific capacity, 146.72 mA h g^{-1}).

Figure 1.3 represents the crystal structure of $LiNi_{0.5}Mn_{1.5}O_4$ spinel material. The spinel-framework structure inherently makes it easier for the lithium ion transportation inside the bulk materials (Solid-state diffusion) because the spinel structure is based on a three-dimensional MO_2 (M: transition metals) host and the vacancies in transition metal layer along [111] cubic structure ensure three-dimensional lithium pathways. In the structure of LiM_2O_4 spinel, M cations occupy the octahedral site, however a quarter of them are located in the lithium layer alongside $[111]_{cubic}$, leaving a quarter of the site in transition metal layer vacant. Lithium ions occupy the tetrahedral sites in lithium layer that share faces with these empty octahedral sites in the transition metal layer. Due to the differences in the charges and ionic radii of Mn^{4+} and Ni^{2+}, this material has two different crystallographic structures, which is highly influenced by the heat-treatment condition during the synthesis. One is a perfectly ordered structure in which all Ni^{2+} ions are fully coordinated by 6 Mn^{4+} nearest-neighbors in the lattices (Space group: P 4_3 3 2). The other is a disordered structure in which Ni^{2+} and Mn^{4+} are distributed randomly among the 16d octahedral sites (Space group: F d -3 m). Many researchers have endeavored to study two

different crystallographic structures of $LiNi_{0.5}Mn_{1.5}O_4$ spinel material: the disordered structure with the space group F d -3 m and the ordered structure with the space group P 4_3 3 2.[4-7] The main factors affecting the electrochemical performances have been identified: the degree of cation ordering between Mn^{4+} and Ni^{2+} ions,[4, 6, 8] composition ratio of Mn and Ni,[9-10] Mn^{3+} content,[11-13] morphology,[14] surface plane with preferred orientation,[15-17] surface compositions[18] which derived from various synthesis, and calcination/annealing conditions.
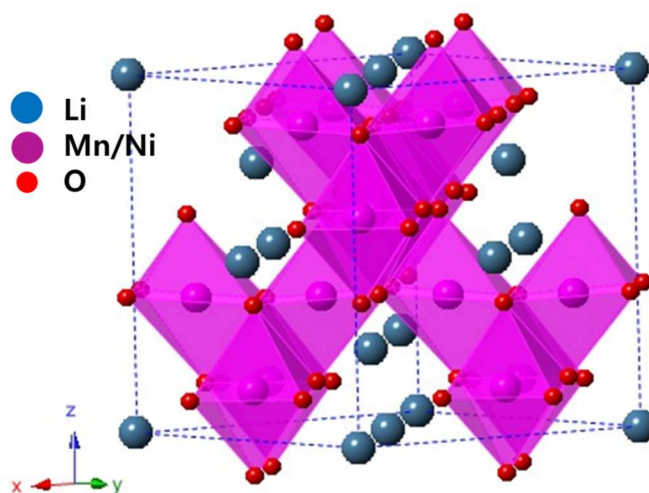
Figure 1.3 Crystal structure of $LiNi_{0.5}Mn_{1.5}O_4$ spinel (Blue: lithium ions, Purple: transition metal ions, and Red: oxygen ions)

1.3. Conversion Materials, CuF_2

Transition metal compounds M_xX_y (M=Co, Fe, Ni, Cu, etc,; X=F, O, S, N, etc.), so called "conversion" materials, have now been widely investigated for their potential use in rechargeable batteries because of their high capacity.[19] During the conversion reaction, more than one electron transfer occur per transition metal ion, which is opposed to limited < 1.0 electrons for intercalation reactions. Among all the known conversion materials, CuF_2 is of particular interest due to its high specific capacity (528 mA h g^{-1}) and voltage (3.55 V vs. Li/Li$^+$). The large band gap offers high operating voltages, but low electronic conductivity and poor rate performance. The large voltage hysteresis during the charge/discharge limits the overall energy efficiency. In particular, it has never been shown the reversible conversion reaction. This is mainly due to sintering of metal nanoparticles, huge volume change, and metal dissolution into the electrolyte. Although recent progress began to show promising results, several remaining challenges still prevent it from use. A study by Badway et al. on iron fluoride demonstrated enhanced electrochemical properties by fabricating the formation of carbon metal fluoride nanocomposites.[20] When this research was applied to copper, it showed an increase in theoretical capacity to 50%, however when the carbon was replaced with mixed conductors, such as MoO_3, the capacity was increased up to 85 %. Wang et al. suggested that origins of poor reversibility in CuF_2 conversion process was explained by the segregation of large Cu particles (5-12 nm).[21] It does not provide any pathway for local electron transport through the insulating LiF phase. To characterize the effect of protective coating on conversion mechanism, it is essential to employ techniques that are sensitive to both structure and chemistry of the materials, and

independent of long-range order. Since the conversion process involves amorphization and nanoparticle, it is limited to use standard crystallographic tools.

Chapter 2. Background

2.1. Nano-Size Effects – Active Interfacial Area

During electrochemical reactions in the lithium-ion batteries, mobile species of lithium ions transport from positive electrode to negative electrode through the electrolyte or vice versa, and there are a few different elementary reaction steps: a mass transfer reaction via separator with electrolyte, a surface film reaction, a charge transfer reaction at the interface between the active material and electrolyte, and lithium ion diffusion within solid-state materials. Among various electrode materials, solid-state diffusion of lithium ions inside the active material is generally considered to be the rate determining step of lithium-ion batteries. Previously, however, the systematic investigation in $LiCoO_2$ material disclosed that charge transfer reaction step proved to be the most important factor in high rate battery discharging.[22] Recently, Singer et al. reported a direct observation of non-equilibrium structural dynamics in spinel $LiNi_{0.5}Mn_{1.5}O_4$ materials using in situ coherent X-ray diffraction under operando conditions.[23] It is interesting that a comparison between the X-ray data and the electrochemical data disclosed a significant discrepancy. It is because the electrochemistry is governed by the surface of the electrode and X-ray diffraction is sensitive to bulk electrode material. As shown in Figure 2.1, during fast charging process the surface of the active material is actually delithiated and acts as an ionic blockade for ions trapped at the interface, hence delaying the phase-transformation inside the bulk materials.

Nano-structured active materials with nano-pores and/or particles are hopeful approaches to ensure the maximized active surface area, thereby significantly accelerating

lithium ions insertion/extraction.[24-25] However, a difficulty of uniform dispersion and an unwanted charge consumption during the initial surface film formation because of its extremely large surface area need to be resolved for the practical use.
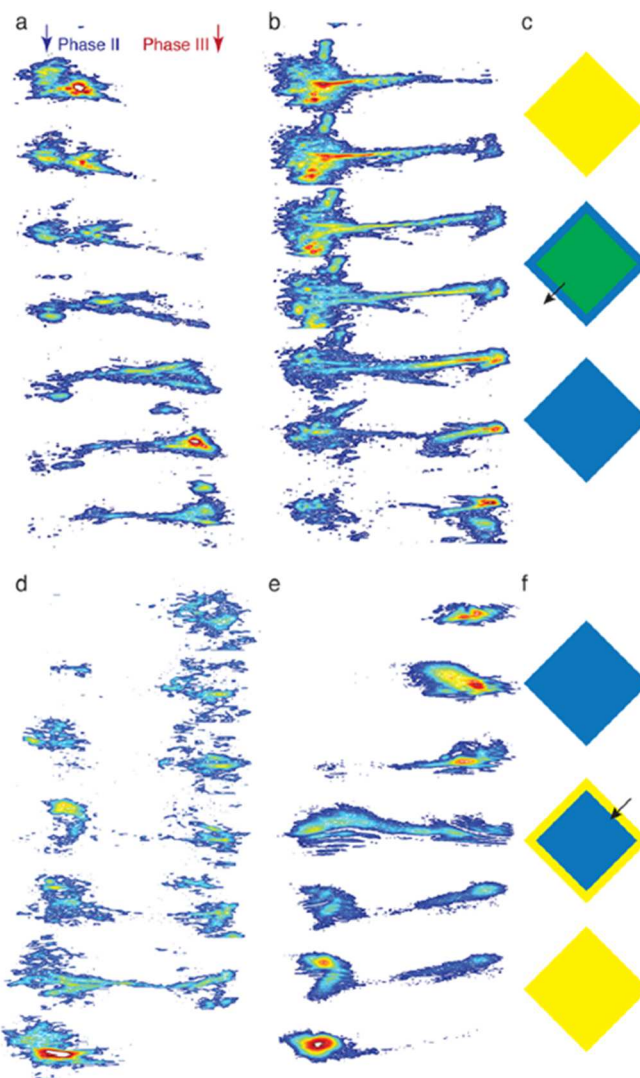
Figure 2.1. Phase transformation of different particles during (a,b) charging and (d,e) discharging. Discrepancy between X-ray and electrochemistry explained by ionic blockade during the fast rates for ions trapped at the surface of materials (c,f)[23]

2.2. Nano-Size Effects – Diffusion / Phase-Transformation

Diffusion process is crucial reaction step when interfacial charge transfer is relatively facile and thus the total intercalation is governed by the solid-state diffusion inside active materials. Fundamentally, the activation energy for diffusion step highly relates to the length of the diffusion path, and the electrostatic interaction between lithium ions and coordinated neighbors. Much work has been done to improve lithium diffusivity by compositional and/or structural modification at atomic scale on the basis of ab initio calculation.[26-27] Application of nano-size active materials for the lithium-ion batteries has a genuine benefit to improve solid-state diffusion of lithium ions.[28] The improvement of lithiation/delithiation kinetics can be attributed to a reduction in the characteristic time constant ($t = L^2/D$; L = diffusion length, D = diffusion constant). The time t for intercalation decreases with the square of the particle size upon reduction of dimensions.

As a result of diffusion process, the active materials encounter the structural dynamics during charging and discharging process. Many electrode materials including $LiFePO_4$,[29-30] $Li_4Ti_5O_{12}$,[31] and $LiNi_{0.5}Mn_{1.5}O_4$[13, 32] are known to coexist in two structural phases with different lattice parameters at particular lithium contents. Phase separation is a reluctant phenomenon due to a slow nucleation of a new phase, diffusion limited across the phase boundary, and strain from phase separation, which leads to defect formation and capacity fade. Ulvestad et al. studied in-situ three-dimensional strain evolution of a single $LiNi_{0.5}Mn_{1.5}O_4$ particle during charging and discharging process with coherent X-ray diffractive imaging.[33] The study reported direct observation of both stripe morphologies and coherency strain at nanoscale. Figure 2.2 presents the interior strain distribution on selected cross sections. The diffuse width of the stripe boundary, estimated from the images

as 50 nm, indicates the minimum size for two-phase coexistence. It is plausible that the particle less than 50 nm would not involve the phase separation but exist entirely as one phase or the other.
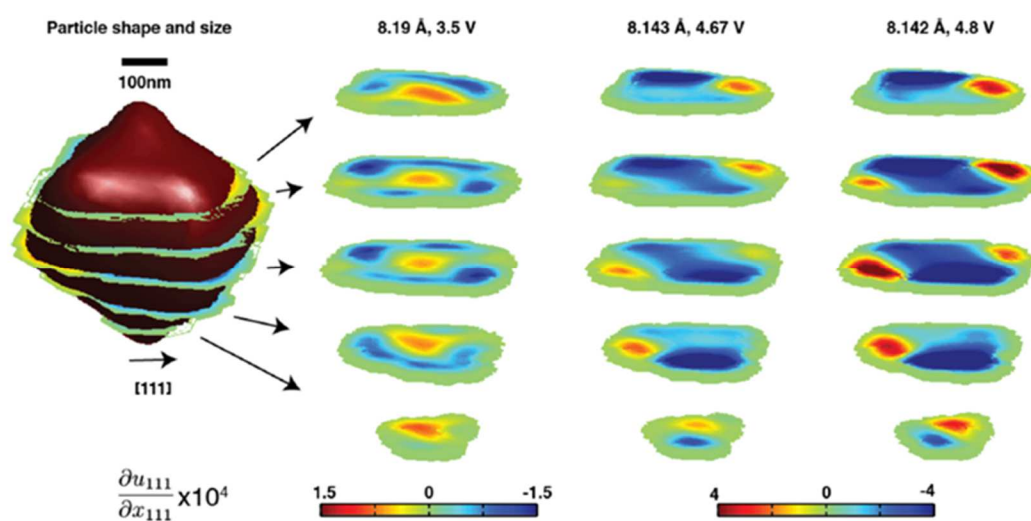
Figure 2.2. Interior strain distribution on selected cross sections at positions shown by the leftmost figure[33]

2.3. Nano-Size Effects – Volume Change

Energy density as well as power density and safety are important issues in lithium-ion battery applications. It is straightforward that batteries with high energy density enable the electric devices to operate for a longer time. Therefore, it is required to increase specific capacity in order to obtain higher energy density. Alternative electrode materials, which have alloying reaction, such as Sn and Si, are considered to be promising candidates for negative electrode.[28, 34] The theoretical capacities of Sn and Si are 990 and 4200 mA h g^{-1}, respectively, which is much higher than that of graphite, 370 mA h g^{-1}. This type of electrode materials suffer from expanding and contracting as lithium ions are inserted and extracted, respectively. The repetition of this volume change during charging and discharging process generates fatigue of the materials, and eventually they are cracked out or pulverized, resulting in severe capacity fading. One of simple solution for this volume change problem is nano-size materials. Yang et al. reported that nano-size Sn electrode show better cycling performance than bulk-size Sn electrodes due to a smaller absolute volume change.[35] This finding provoked lots of nano-structured materials in lithium-ion batteries. Transition metal compounds M_xX_y (M=Co, Fe, Ni, Cu, etc,; X=F, O, S, N, etc.), so called "conversion" materials, also go through the volume change during charging and discharging process. Badway et al. inform that nano-size metal fluoride composite with carbon shows improved electrochemical properties.[36]

Chapter 3. Synthesis and Characterization

3.1. Sol-Gel based Template Method

Martin opened up the nanofabrication strategy of template synthesis.[37-38] This method has been employed to synthesize nano-structured materials, for instance, carbon, gold, semiconductors, polymers, and battery electrode materials. This method generally involves deposition of precursor materials into a micro- or nano-porous template. This template is commercially available track-etch polymer membranes or anodic aluminum oxides. Both the pore diameter and the specific chemical interaction between the pore wall and the precursor result in different structures such as tubes or wires.

Figure 3.1 illustrates the schematics of the sol-gel based template synthesis. A precursor impregnated polycarbonate template is placed on top of platinum foil. The foil not only serves as a substrate during its synthesis, but also plays a role of a current collector during the electrochemical characterization. After drying up of the gelation process, the template is removed by the plasma etching. Finally, with the help of heating or aging process, the precursor turns into the desired product. The result is a nano-structured electrode that reflects the geometry of pores of the template, such as length, diameter, and number density. Nanowires protrudes from the surface of the current collector like bristles of a brush. In the conventional electrode of lithium-ion batteries, active materials are mixed with polymeric binder (PVdF) and a conductive additive (carbon). In this template method, those inactive components are not necessary and are excluded. Therefore, this nano-structured electrode can be a good candidate for the investigation of true nano-size effects.
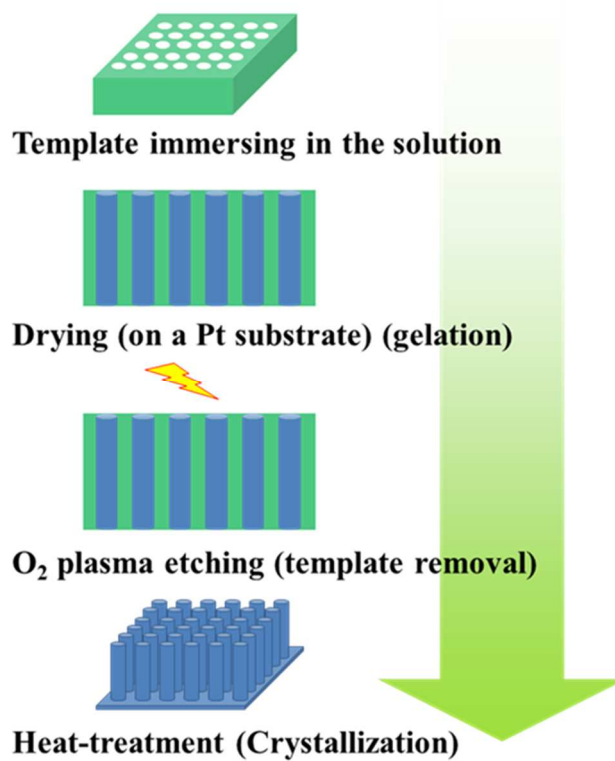
Figure 3.1. Schematics of the sol-gel based template synthesis

3.2. Electrochemical Impedance Spectroscopy

In practical batteries, the influence of current rate on the electrochemical cell is controlled by polarization, which is derived from the elementary reaction steps. The most common are direct measurement of instantaneous current and voltage characteristics on charge and discharge curves. The curve can be utilized to calculate the cell capacity, the effect of charge and discharge rates, and any information on state of health of batteries.

Another technique to characterize the battery behavior is the electrochemical impedance spectroscopy, which can reveal a significant amount of information about battery operation characterization.[39-40] The impedance of an electrode is given by

$$Z = R + j\omega X$$

where $X = \omega L - 1/(\omega C)$, $j = \sqrt{-1}$, and ω is the angular frequency ($2\pi f$); L is the inductance, and C is the capacitance. A typical impedance spectra and corresponding equivalent circuit, illustrating the behavior of intercalation electrode processes, are shown in Figure 3.2 and 3.3. Activation processes present a semicircular behavior with frequency that is characteristic of relaxation processes. Concentration processes exhibit a characteristic 45° behavior of diffusion processes, referred to as Warburg behavior. Ohmic components have no capacitive character and are independent of frequency. The frequency of the maximum, f_{max}, of the semicircle gives the relaxation time, where $\tau = 1/f_{max} = RC$. Some electrochemical capacitors take advantage of this capacitance to enhance its performance of supercapacitors, such as electrochemical double-layer capacitor.
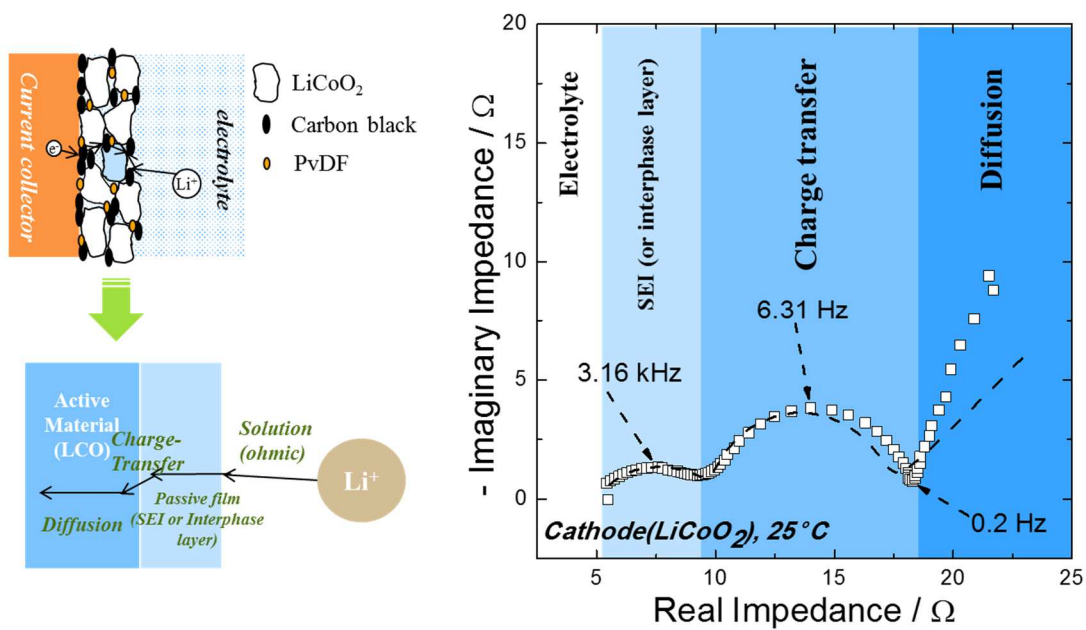
Figure 3.2. Typical impedance spectra of intercalation material (LiCoO$_2$)
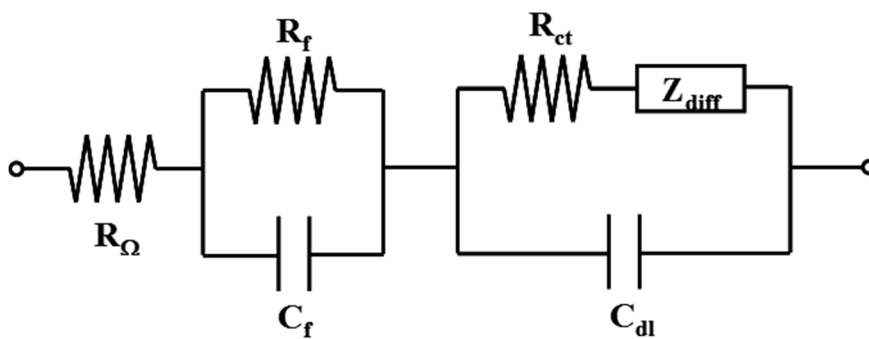
Figure 3.3. Typical equivalent circuit for the intercalation electrode reaction

3.3. X-ray Diffraction

X-ray diffraction (XRD) is a powerful method to uniquely identify crystalline phases in materials of interest and to measure the structural properties, such as grain size, phase composition, preferred orientation, and defect structures.[41] X-ray diffraction is a noncontact and nondestructive method. Materials consists of any element can be successfully investigated with X-ray diffraction, however it is more sensitive to high-Z elements, because the diffracted intensity from these high-Z elements is much larger than from low-Z elements. Therefore, the sensitivity of X-ray diffraction relies on materials. With in-house X-ray source, the sensitivities down to thickness of ~ 50 Å are achievable, but synchrotron radiation allows the characterization of much smaller size.

The most common X-ray source of the in-house experiments is copper with a characteristic wavelength of 1.54 Å. Synchrotron radiation sources that contain a large cyclic particle accelerator with magnetic fields guide electrons. Electric fields accelerate the electrons that are synchronized with the travelling particle beam. The brilliance of a synchrotron source is about 10 orders of magnitude greater than in-house X-ray diffractometers. In addition, synchrotron radiation uses photon energies that are two orders of magnitude higher than in-house X-ray sources.

Crystals consist of planes of atoms that are spaced a distance, d, but can be resolved into various atomic planes with a different d-spacing. The certain atomic plane can be uniquely identified by the Miller index. These are the three reciprocal intercepts of the plane with the a, b, and c, and are reduced to the smallest integers with the same ratio. Therefore, a (hkl) plane intercepts the crystallographic axes at a/h, b/k, and c/l. The d-spacing between (hkl) planes is denoted d_{hkl}, and for cubic crystals, it is

$$d_{hkl} = a_0 / \sqrt{(h^2 + k^2 + l^2)}$$

where a_0 is the lattice constant of the crystal.

When there is constructive interference from X-ray scattered by the atomic planes in the crystalline material of interest, a diffraction peak is observed. Bragg's law allows a condition for constructive interference from planes with spacing d_{hkl},

$$\lambda = 2 \, d_{hkl} \sin \theta_{hkl}$$

where θ_{hkl} is the angle between the atomic planes and the incident and diffracted X-ray beam, as shown in Figure 3.4. In order to observe the diffraction, the detector should be positioned for the diffraction angle at $2 \, \theta_{hkl}$. The crystalline material must be oriented so that the normal to the diffracting plane is coplanar with the incident and diffracted X-rays. The angle between the diffracting plane and the incident X-rays is equal to the Bragg angle θ_{hkl}.
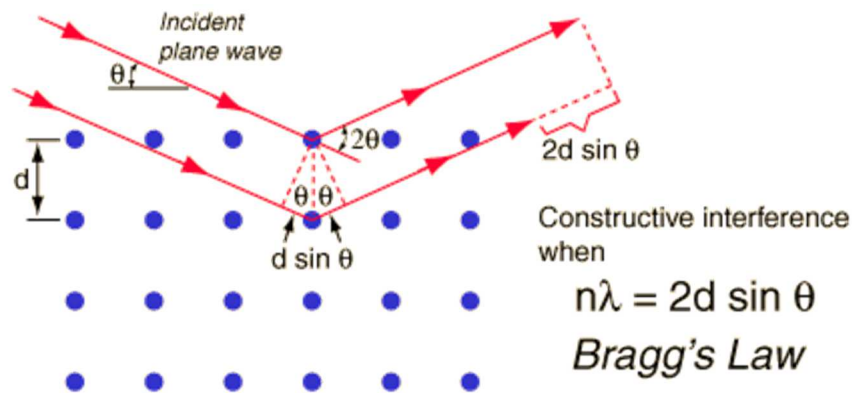
Figure 3.4. Schematics of Bragg's Law

3.4. Pair Distribution Function Analysis

The traditional crystallographic structure characterization of X-ray diffraction is no longer sufficient to investigate properties of materials on an atomic scale. The limitation of the traditional method is that it only yields the long-range average structure of the material. The pair distribution function (PDF) analysis, however, gives more information about local arrangements, because it uses the total scattering pattern, which includes Bragg and diffuse scattering. The pair distribution function gives the probability of finding an atom at a given distance from another atom. Therefore, the study of the pair distribution function on different length scales allows researchers to get the information about the nano-scale structure of materials.

From the powder diffraction data, the pair distribution function is achieved by a sine Fourier transform of normalized scattering intensity S(Q),[42-43]

$$G(r) = 4\pi r \left[\rho(r) - \rho_0\right] = \left(\frac{2}{\pi}\right) \int_0^\infty [S(Q) - 1] \sin(Qr) \, dQ$$

Where $\rho(r)$ is the microscopic pair density, ρ_0 is the average number density and Q is the magnitude of the scattering vector.

The pair distribution function analysis provides atomic scale structural insights, from the local coordination geometry to several nanometers. The pair distribution function analysis has an advantage of describing the short- as well as medium-range local structure, compared with the X-ray absorption fine structure (XAFS) method, which only enables to determine the first and second nearest neighbor distances. The peaks in the pair distribution function are related to the bond lengths and atom to atom distances. The spatial extent of well-defined peaks corresponds to the length scale, which is over the ordered structures,

such as, particle size or local structure within an amorphous system. The intensities of peaks come from relative abundance of each atom to atom distance, which are coordination number and relative abundance of a particular elements. Figure 3.5 shows a good example of the pair distribution function analysis. The diameter of the bucky ball, C_{60}, is 7.1 Å. Sharp peaks are observed in the pair distribution function pattern coming from the characteristic C-C pairs on the ball up to 7.1 Å. Thereafter only broad featureless structure exists. The sharp peaks are intra-molecular structure and the broad feature is inter-molecular structure, or ball-ball correlations.
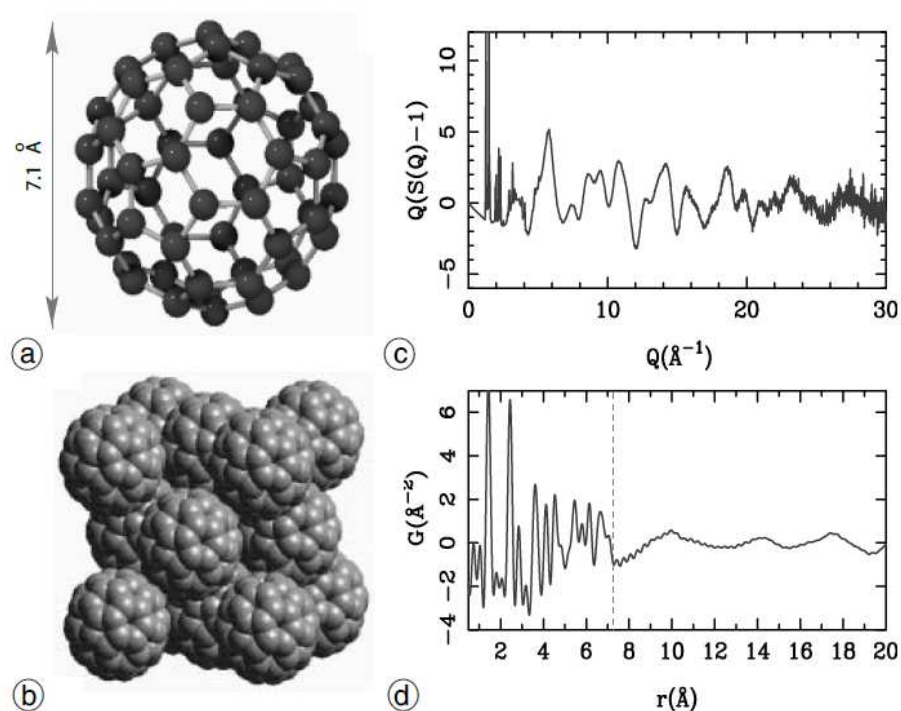
Figure 3.5. (a, b) C_{60}, (c) its normalized neutron diffraction pattern, and (d) the corresponding PDF. The vertical dotted line in (d) is at 7.1 Å the diameter of the ball[42]

Chapter 4. Effect of Ni/Mn Ordering on Elementary Polarizations of LiNi$_{0.5}$Mn$_{1.5}$O$_4$

Spinel and Its Nanostructured Electrode

Elementary polarizations of LiNi$_{0.5}$Mn$_{1.5}$O$_4$ spinel materials with disordered structure (space group, F d -3 m) and ordered structure (space group, P 43 3 2) are quantitatively analyzed in order to clarify how the differences in crystallographic structure affect the rate performance of the cathode materials. Furthermore, the ordinary approach to increase the rate performance of an electrode through a reduction of the diffusion lengths and an enlargement of the active surface area with the nano-structured electrode is systematically investigated.

4.1. Introduction

LiNi$_{0.5}$Mn$_{1.5}$O4 spinel materials have attracted particular attention as a promising candidate for replacing the current commercially available positive materials, e.g. LiCoO$_2$, of lithium-ion batteries.[10, 13, 44] Spinel LiNi$_{0.5}$Mn$_{1.5}$O$_4$ provides a high-voltage plateau at ~ 4.7 V (vs. Li/Li$^+$) and thus enables relatively higher energy density (theoretical specific capacity, 146.72 mA h g^{-1}). Inherently, the spinel-framework structure makes the lithium ion transportation inside the bulk materials (solid-state diffusion) easier because the spinel structure is based on a three-dimensional MO$_2$ (M: transition metals) host and the vacancies in transition metal layer along [111] cubic structure ensure three-dimensional lithium pathways. In the structure of LiM$_2$O$_4$ spinel, M cations occupy the octahedral site but ¼ of them are located in the lithium layer along [111]cubic, leaving ¼ of the sites in transition

metal layer vacant. Lithium ions occupy the tetrahedral sites in lithium layer that share faces with these empty octahedral sites in the transition metal layer.[3]

Many researchers have endeavored to study the two different crystallographic structures of $LiNi_{0.5}Mn_{1.5}O_4$ spinel material: the disordered structure with the space group F d -3 m and the ordered structure with the space group P 4_3 3 2.[12-13, 45-46] Despite its importance to the overall performance, there is still a lack of understanding of how ordering of nickel and manganese on the octahedral sites affects the elementary reactions steps involved in their electrochemical operation. In this work, we have used a combination of electrochemical impedance spectroscopy and the theoretical analysis of their equivalent circuits,[22, 47-48] to quantitatively analyze and compare the proportional contribution of the elementary reaction steps to the total polarization of the disordered and ordered structures. Furthermore, the nano-structured electrode is prepared in order to improve its rate performance, and the variation of its elementary reaction steps are analyzed and compared to those in the conventional composite electrodes. Since the instantaneous power density is one of the key performance factors for designing the battery for transportation application, we focus on the analysis of the elementary reaction steps at the charged state of the battery at the initial discharging time. This work serves as a good starting point to fundamentally understand the nano-structured electrode kinetics, with the goal of designing batteries possessing the ideal performance.

4.2. Experimental

$LiNi_{0.5}Mn_{1.5}O_4$ spinel materials were synthesized using a sol-gel method.[10] The resulting gel precursors were decomposed at 500 ºC for 12 hours in air and then calcinated

at 900 °C for 14 hours in air. The as-prepared disordered structure powders were made to the ordered structure by annealing at 700 °C for 48 hours in air. For the composite electrode fabrication, the slurry consisting of 80 wt. % active materials, 10 wt. % acetylene carbon black, and 10 wt. % poly(vinylidene fluoride) (PVdF) in N-methyl pyrrolidone (NMP) were pasted on the aluminum foil current collector, dried overnight in a vacuum oven at 80 °C, and punched and pressed uniaxially. In order to minimize the effect of the porosity, the similar loading weights of the cathode electrodes are employed in this work (0.01378 g and 0.01384 g for the disordered and ordered structures, respectively).

LiNi$_{0.5}$Mn$_{1.5}$O$_4$ spinel materials were also prepared as a nano-fiber/-wire structure via a sol-gel based template-assisted synthesis method. Commercially available polycarbonate porous membrane (Whatman, P/N: 7060-2502) of 200 nm (= 0.2 μm) pore diameter as a template was immersed into a precursor sol. Fully soaked templates were placed on a platinum foil current collector, and gelation was carried out in the drying oven. The oxygen plasma etching system (Trion RIE/ICP dry etcher) was used to remove the template. Eventually, as-prepared protruding nano-structured electrode was crystallized with 900 °C heat-treatment for only 2 hours. The active weight of the nano-structured electrode is estimated from the calculated volume and the observed porosity, the value is in good agreement with the measured value by an electronic balance with 0.1 mg accuracy.

The morphologies and size distributions were examined with a scanning electron microscope (SEM, Phillips, XL30) and a transmission electron microscope (TEM, FEI Tecnai G2 Sphera cryo-electron microscope). For the TEM, the nano-structured fibers were suspended on a 300 mesh copper grid with lacey carbon. In order to identify the crystalline phase of the synthesized materials, powder X-ray diffraction (XRD, Bruker D8)

measurements using Cu Kα radiation were employed. XRD data were obtained for the range $2\theta = 10 - 80$ º, with a scan rate of 0.02 º s^{-1}. XRD data analysis was carried out by the Rietveld refinement using the FullProf software package. The molar ratio of Ni and Mn of the samples were analyzed by inductive coupled plasma optical emission spectroscopy (ICP-OES Perkin-Elmer Plasma 3700).

The methodology to analyze quantitatively the effect of the elementary impedances on the total dc polarization was introduced in the previous work.[22, 47-48] In this work, with the use of such methodology, the effect of the crystalline structure difference (disordered and ordered structures) was compared. In addition, the effects of nano-structured electrode on the rate performance were investigated. For the electrochemical experiments, the custom-made three-electrode cell configuration was employed.[22, 47-49] The prepared electrodes and lithium metal were used for the positive and negative electrodes, respectively. For the reference electrode, the copper wire was placed in between separators (Celgard C480). Before the tests, elemental lithium was cathodically coated on the bare copper wire by taking lithium metal electrode as a counter electrode. The electrolyte was a 1 M solution of lithium hexafluorophosphate (LiPF$_6$) in a 1:1 volume mixture of ethylene carbonate (EC) and dimethyl carbonate (DMC). All the cells used for the electrochemical tests was assembled in a glove box (MBraun, Germany) filled with purified argon gas (H$_2$O level of <1 ppm).

The as-prepared cell was charged and discharged three times between 3.5 and 4.85 V (vs. Li/Li$^+$) at a rate of 0.1 C (= C/10) (the theoretical specific capacity of 146.72 mA h g^{-1} of LiNi$_{0.5}$Mn$_{1.5}$O$_4$ was assumed to convert the current density into C rate). The electrochemical impedance measurement was carried out in the frequency range of 100

kHz to 10 mHz at a cell potential of 4.85 V (vs. Li/Li$^+$) using a signal with an amplitude of 10 mV. Pulse discharge tests were performed right after the impedance test. For the pulse discharge test, a variety of pulse discharge currents were applied when a constant potential of 4.85 V (vs. Li/Li$^+$) was obtained at the open circuit. In order to get the open circuit voltage with negligible lithium contents, all the cells was charged with the application of the low constant current rate, C/20, and the constant voltage was applied subsequently until it has an equilibrated potential after an extended rest at open circuit. We chose low lithium content (high voltage) because it is well known that the electrode/electrolyte interface is less stable at the high voltage where surface film is formed.[50] A Solatron 1287 electrochemical interface was employed to carry out all of the galvanostatic/potentiostatic tests. For the electrochemical impedance measurements, the Solartron 1287 electrochemical interface was coupled with a Solartron 1455A frequency response analyser.

4.3. Results and Discussion

4.3.1. Characterizations of Powder Materials and Nano-Structured Electrodes

Typical morphologies of the LiNi$_{0.5}$Mn$_{1.5}$O$_4$ spinel materials with disordered and ordered structures are shown in the SEM images of Figure 4.1(a) and (b). When disordered structure powders calcinated at 900 °C, the primary particles formed polygonal morphology with the dust-like small particles at the surface as shown in Figure 4.1(a). The average particle size was about 700 nm (in the range of 400-1000 nm). After further annealing at 700 °C, as-prepared ordered structure powders (Figure 4.1(b)) also had polygonal morphology and similar particle size, ca 700 nm (in the range of 400-1000 nm).

(a)
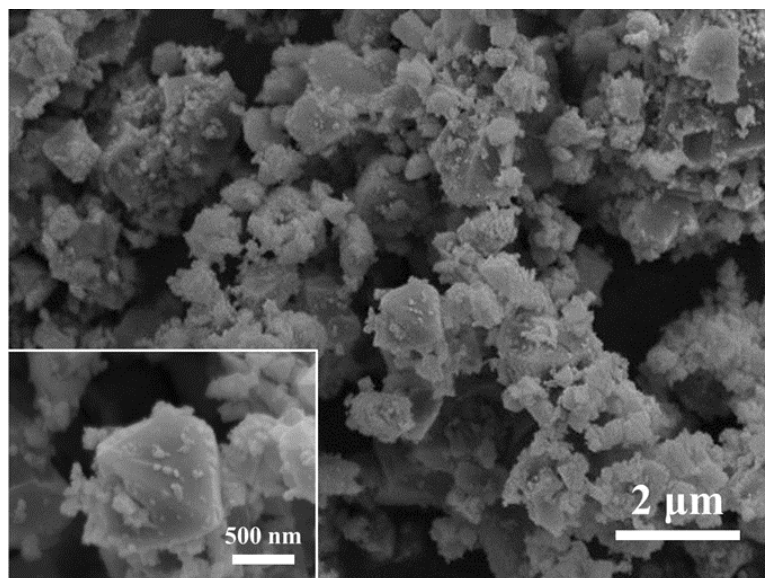
(b)
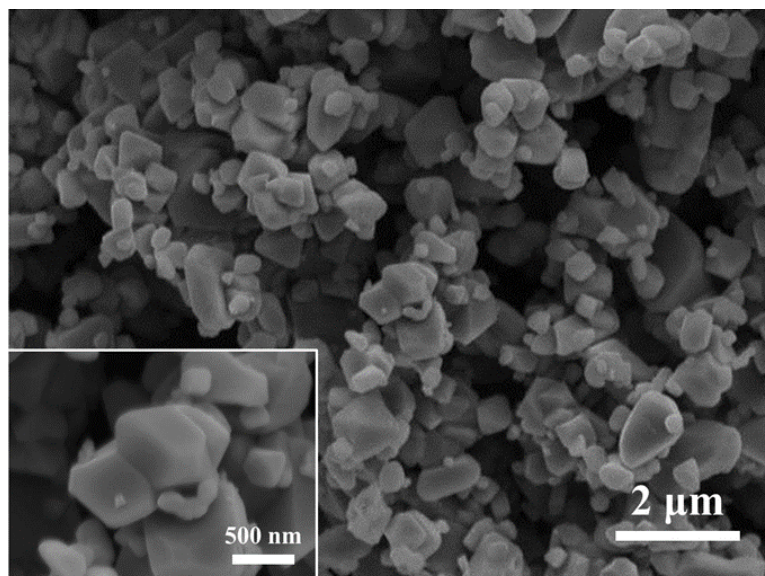
Figure 4.1. Scanning electron micrographs of $LiNi_{0.5}Mn_{1.5}O_4$ (a) disordered structure and (b) ordered structure powders synthesized via a sol-gel method, and (c) top views of nanowire prepared via sol-gel based template synthesis method

(c)
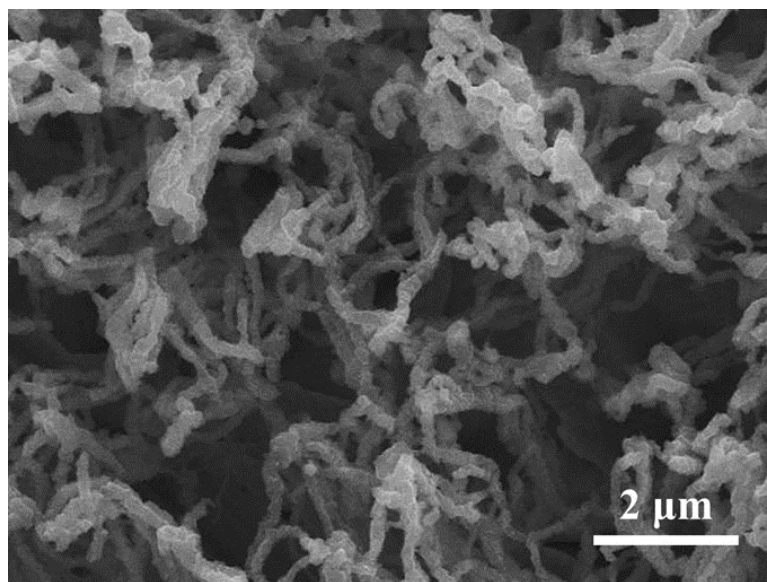
Figure 4.1. Scanning electron micrographs of LiNi$_{0.5}$Mn$_{1.5}$O$_4$ (a) disordered structure and (b) ordered structure powders synthesized via a sol-gel method, and (c) top views of nanowire prepared via sol-gel based template synthesis method, continued.

It is notable that the tiny particles at the surface of the disordered structure disappeared completely with the transformation from the disordered structure to ordered structure. It has been reported that the separate small particles are the rock-salt phase that is commonly observed in the synthesis of LiNi$_{0.5}$Mn$_{1.5}$O$_4$ spinel materials, especially over 700 ºC calcination temperatures.[12, 45-46]

For the nano-structured electrode of LiNi$_{0.5}$Mn$_{1.5}$O$_4$ spinel materials, sol-gel based template synthesis method[38, 51-52] was employed in this work, as described in the experimental section. Figure 4.1(c) shows the SEM image of as-prepared nano-structured electrode, depicting the nano-fibers protruding from the surface of the platinum current collector, like shrubs with twisted branches. The average diameter of the nano-fibers and

length were approximately 160 nm and 12 µm, respectively. A closer look at the nano-structured electrodes with the TEM images in Figure 4.2 reveals that it is constructed with a series of connected particles (ca. 160 nm of the average particle size in the range of 50-200 nm).

In order to identify the structural properties of the materials, the XRD patterns are collected and compared as shown in Figure 4.3. The nominal $LiNi_{0.5}Mn_{1.5}O_4$ spinel material is cubic close packed with lithium on the tetrahedral sites. The disordered structure with nickel and manganese disordering on the octahedral sites has the space group, F d -3 m, while, the ordered structure has the space group, P 4_3 3 2.[4, 6] The Rietveld refinement patterns of the XRD for both disordered and ordered structures indicated an excellent agreement with those reported previously in the literatures.[4, 46, 53] In the case of the disordered structure (Figure 4.3(b)), small peaks were observed at 2θ = 37.6 °, 43.7 °, and 63.5 °, indicative of a cation-rich rock salt phase (as mention in the Figure 4.1(a)). Recently, it is reported that this rock salt phase contains both manganese and nickel in a lower ratio than in the spinel phase.[12] The superstructure peaks of the ordered structure (Figure 4.3(c)) were confirmed with the small peaks observed at 2θ = 15.3 °, and 39.7 °, consistent with the literature report.[4] The lattice parameter of the disordered structure, 8.1739 Å, is larger than that of the ordered structure, 8.1653 Å. The presence of Mn^{3+} in the spinel phase, which can be derived from the 4 V (vs. Li/Li^+) plateau shoulder in charge/discharge curves, results in a larger lattice parameter.[45, 54] The XRD patterns of the nano-structured electrode discloses that the nano-structured electrode consists of the $LiNi_{0.5}Mn_{1.5}O_4$ spinel materials, as shown in Figure 4.3(a). Since the peaks of the nano-structured electrode are relatively weak and broad, attempts to account for them by introducing the phase into the Rietveld

(a)
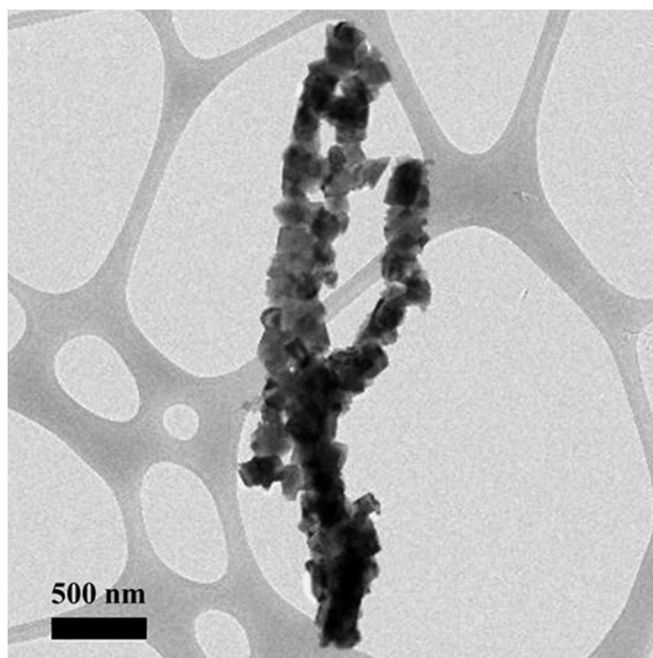
(b)
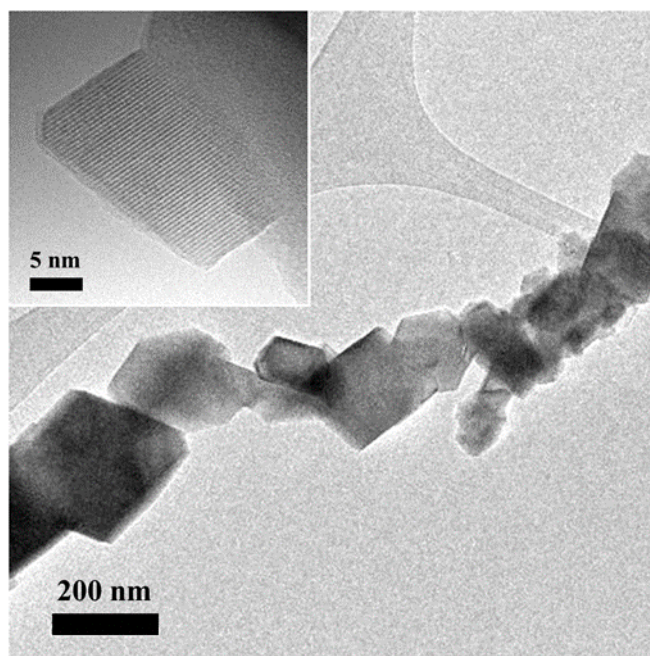
Figure 4.2. Transmission electron micrographs of (a) and (b) nanowire prepared via sol-gel based template synthesis method
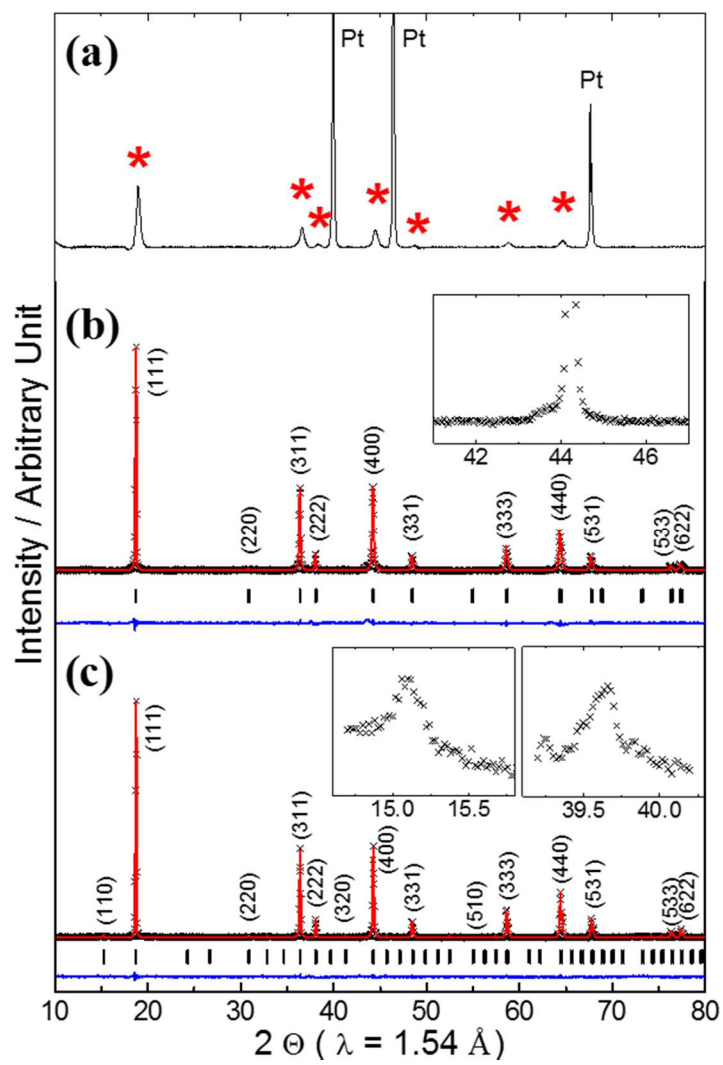
Figure 4.3. XRD patterns of (a) as-prepared nanowire electrode. The Rietveld refinement results from XRD patterns collected from $LiNi_{0.5}Mn_{1.5}O_4$ (b) disordered structure and (c) ordered structure powders synthesized via a sol-gel method

refinements did not yield satisfactory results. Nevertheless, all the peak positions are well-matched with the powder materials synthesized via a sol-gel method, except the peaks from the platinum current collector (see asterisks in Figure 4.3(a))

The Ni and Mn molar ratio of the pristine materials were checked by ICP-OES analysis (Table 4.1). Although a cation-rich rock salt phase appeared in the disordered structure, the molar ratio of Ni and Mn is in good agreement with the theoretical ratio in all samples.

Table 4.1. Ni : Mn molar ratio of the pristine $LiNi_{0.5}Mn_{1.5}O_4$ materials, disordered structure (F d -3 m), ordered structure (P 4_3 3 2), and nanowires as measured by ICP-OES

Sample	Ni:Mn ratio experimental (ICP-OES)	Theoretical
Disorder (F d -3 m)	3.02	
Order (P 4_3 3 2)	3.05	3.00
Nano-wires	3.01	

4.3.2. Effect of the Crystalline Structures on the Elementary Electrode Reactions

Figure 4.4 presents the cell potential (or cathodic polarization) transients of the as-prepared disordered and ordered structures during constant current discharging for 10 seconds at different discharging rates. Right after the pulse discharging, the transients showed a rapid drop and a relatively slow decrease in potential with time. The transients

of the disordered structure (solid lines) fell slower than those of the ordered structure (dotted lines). The maximum discharging rate of the disordered structure was 30 C; the cell potential still remained above the low cut-off voltage of 3.5 V (*vs.* Li/Li$^+$) throughout the whole discharging time. However, at the discharging rate of 15 C, the cell potential transient of the ordered structure reached the cut-off voltage before 10 seconds. This means that the disordered structure enables a more prolonged operation at high current drains compared to the ordered structure; i.e., the disordered structure shows better rate performance than the ordered structure, which is consistent with earlier reports.[4, 6, 12-13, 45, 53]
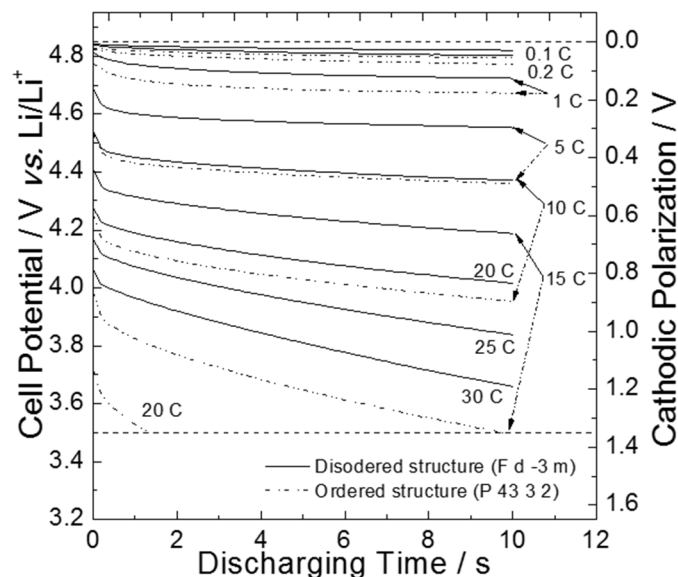
Figure 4.4. Experimental cell potential (or cathodic polarization) transients during the cathodic pulse discharging for 10 s at different discharging rates obtained from LiNi$_{0.5}$Mn$_{1.5}$O$_4$ disordered and ordered structure
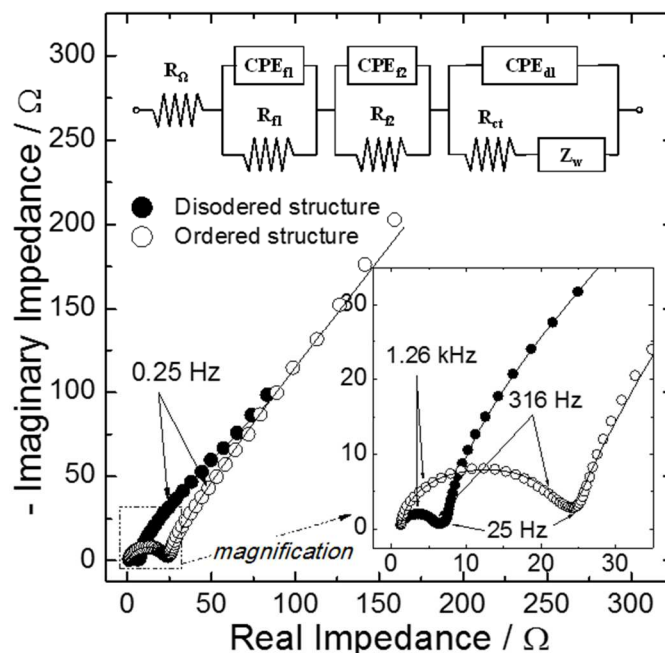
Figure 4.5. Impedance spectra of the positive electrodes from the disordered (solid) and ordered (hollow) structures, obtained at a cell potential of 4.85 V (vs. Li/Li$^+$). The inset is the equivalent circuits to model its reactions

To explore how a dissimilarity of nickel and manganese ordering in the crystal structure affects the elementary reaction steps and their contribution to the total dc polarization, the differentiation of the resistive elements was done by using the electrochemical impedance spectroscopy, as shown in Figure 4.5. For the positive electrodes (intercalation process, Figure 4.5), it is generally agreed that the depressed semicircle in the high-frequency range reflects lithium-ion migration though multilayer surface films, and, in the medium-frequency range, nearly perfect (undepressed) semicircle is attributed to charge-transfer resistance coupled with the double layer capacitance at the interface between the surface film and intercalation materials. Also, the inclined line in the low-frequency range is responsible for the solid-state lithium diffusion through the

intercalation materials, known as the Warburg impedance.[40, 55-58] On the other hand, the origin and mechanism of lithium negative electrode reactions are not clear at this point. The detailed analysis of the lithium negative electrode is beyond the scope of this work.

To quantitatively analyze the obtained impedance spectra, the mechanism-based equivalent circuits which model the elementary reactions was adopted, as shown in the insets of Figure 4.5. First resistance, R_Ω, indicates the uncompensated ohmic resistance. A series of the resistance and constant phase element (CPE), R_{f1}-CPE_{f1} and R_{f2}-CPE_{f2}, represents the lithium migration through multilayer surface films, which can be simplified into porous part and compact interphase. From the reported literatures,[57-61] it is demonstrated that Li intercalation processes of Li_xMO_y materials, such as $Li_xMn_2O_4$, Li_xNiO_2, and Li_xCoO_2, show similarity with the graphite materials, and thus, typical impedance spectra of Li_xMO_y materials are also similar with that of the graphite materials. Therefore, those impedance spectra were nicely fitted with the multilayer surface film model. In this work, the impedance spectra of $LiNi_{0.5}Mn_{1.5}O_4$ spinel are also analogous to other intercalation materials, which contain a high frequency semicircle which is basically potential invariant. This similarity justifies the adoption of the impedance model with the multilayer surface films. And a pair of the resistance and CPE, R_{ct}-CPE_{dl}, shows the charge-transfer resistance and double layer capacitance. In addition, the Warburg impedance, Z_w, indicates the solid-state diffusion. All the electrical parameters in the equivalent circuit were determined from the CNLS (complex non-linear least squares) fitting method, and are summarized in the Table 4.2. The equivalent circuit based on the obtained electrical parameters was re-constructed towards the circuit simulation, as explained in the previous literatures.[47-48]

Table 4.2. Electrical parameters of the working electrodes, determined from the complex non-linear least squares (CNLS) fitting of impedance spectra to the equivalent circuit. This also includes the diffusion coefficient, diffusion length and some calculated values

	R_Ω	R_{f1}	CPE_{f1} [1]		R_{f2}	CPE_{f2} [1]		R_{ct}	CPE_{dl} [1]		A_ω [2]	D [3]	L [4]	R_D [5]	C_D [5]	r [5]	c [5]
			C	η		C	η		C	η							
	Ω	Ω	$\mu F\,s^{\eta-1}$		Ω	$\mu F\,s^{\eta-1}$		Ω	$mF\,s^{\eta-1}$		$\Omega\,s^{-0.5}$	$\times 10^{-12}\,m^2\,s^{-1}$	nm	Ω	mF	$\times 10^6\,\Omega\,m^{-1}$	$\times 10^6\,F\,m^{-1}$
Disorder (F d -3 m)	1.01	4.86	12.01	0.88	1.65	4103	0.73	18.73	6.26	0.99	51.14	7.76	700	12.85	4.91	18.36	0.007
Order (P 4$_3$ 3 2)	1.19	6.67	3.41	1	15.85	27.06	0.85	99.27	5.56	0.79	87.57	1.91	700	44.32	5.78	63.31	0.008
Nano-wires	3.05	18.8	71.44	0.92	78.62	104.6	0.90	12.44	7.88	1	10.55	14.7	160	0.44	3.95	2.75	0.025

[1] Constant phase element (CPE) was expressed in the form of $C(j\omega)^\eta$ ($0.5<\eta<1$).
[2] A_ω is the Warburg coefficient.
[3] D at 4.85 V (vs. Li/Li$^+$) was estimated from the GITT[67-68].
[4] L was roughly estimated to be the radius of particle from the SEM and TEM observation.
[5] $R_D=A_\omega \cdot L \cdot D^{-0.5}$, $C_D=L^2 \cdot R_D^{-1} \cdot D^{-1}$, $r=R_D \cdot L^{-1}$, $c=C_D \cdot L^{-1}$.

Using the circuit simulation, the variations in the total elementary polarizations of the disordered and ordered structures were obtained with the discharging time at a discharging rate of 5 C, and then, its time-dependent contributions of the elementary resistances to the total polarization were obtained as shown in Figure 4.6(a) and (b). The charge-transfer reaction and solid-state diffusion step are the first and second largest contributions of the total dc polarization for both the disordered and ordered structures. It also proved that the contribution of lithium migration through the surface films is relatively trivial. In addition, it is noteworthy that the contribution of the charge-transfer resistance of the ordered structure shows over 50 % at 10 s discharging, which is considerably higher than that of the disordered structure.

(a)
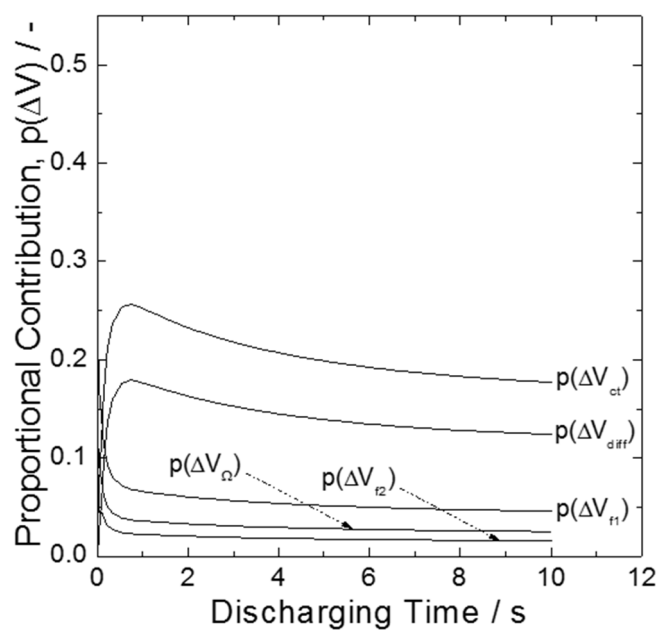
(b)
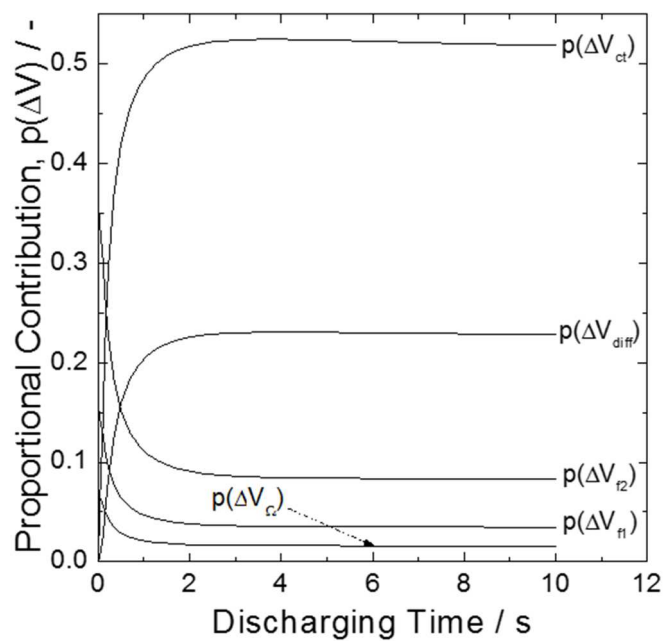
Figure 4.6. Time-dependent proportional contribution of elementary impedances to total polarization at a discharging rate of 5C for $LiNi_{0.5}Mn_{1.5}O_4$ (a) disordered structure and (b) ordered structure

4.3.3. Elementary Reaction Behaviors of the Nano-Structured Electrode

The above results demonstrated that the charge-transfer and diffusion stsep are the two major sources responsible for the power density. Especially, it showed that the nickel and manganese ordering in the spinel structure aggravated the charge-transfer reactions. Now, it would be interesting to see what happens to the nano-structured electrode. The nano-structured electrode has been considered as a promising way to achieve utmost power density without much sacrifice of energy density. Its short diffusion lengths and relatively large surface area will reduce the resistance to interfacial reactions and thus accelerate electrode kinetics.[24, 28, 62-63] In this work, the nano-structured electrode was prepared via the sol-gel based template synthesis,[38, 51-52] as shown in Figure 4.1(c). The conventional composite electrodes consisting of nano-size materials, such as nano-particles, and nano-rods, might be insufficient due to the inherent imperfection of the structure. When the active species around the nano-particles become exhausted, the overall electrode reactions deteriorate rapidly by the transport of the species toward the porous structure. However, the one-dimensional nano-structured electrodes, which stand up from the current collector, not only secure the straight path for the facile movement of the active species in the electrolyte, but also provide continuous pathways for electron transport.

The cell potential (or cathodic polarization) transients of the as-prepared nano-structured electrode during the 10 s current pulse at a variety of discharging rates are shown in the Figure 4.7. All the transients show an abrupt drop at the moment of the application of the current, followed by a gentle decrease in potential with time. It is noted that even at the very high discharging rate of 30 C, its cathodic polarization, 0.5 V, was less than half of the maximum polarization, 1.35 V. There is no doubt that the nano-structured electrode
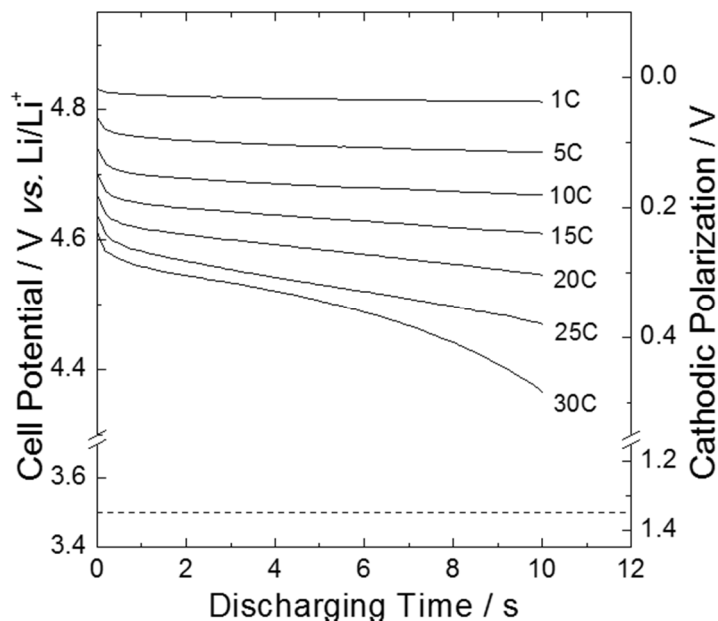
Figure 4.7. Experimental cell potential (or cathodic polarization) transients during the cathodic pulse discharging for 10 s at different discharging rates obtained from nanowire prepared via sol-gel based template synthesis method
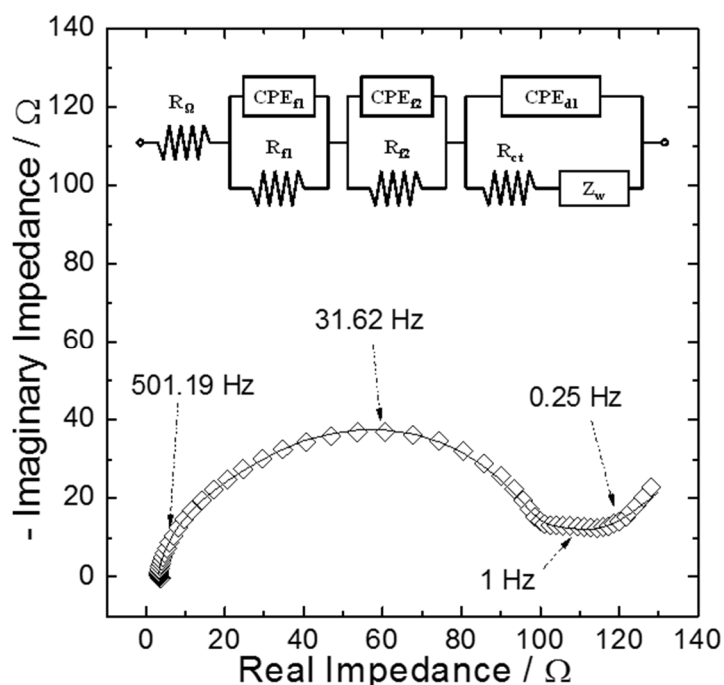
Figure 4.8. Impedance spectra of from the nanowire prepared via sol-gel based template synthesis method. The inset is the equivalent circuit to model the working electrode reaction

improved the power density significantly. The differentiation of the resistive elements was further investigated in the same manner as described above.

Figure 4.8 shows the impedance spectra of the nano-structured $LiNi_{0.5}Mn_{1.5}O_4$ spinel materials obtained after three charge and discharge cycles. Using the same equivalent circuit model, all the electrical parameters were estimated by the CNLS fitting method (Table 4.2). When comparing between the nano-structured electrode and the previous powder composite electrodes, the real impedances of lithium migration from internal compact interphase, R_{f2}, and charge-transfer reaction, R_{ct}, and Warburg coefficient, A_w, are summarized in Figure 4.9.
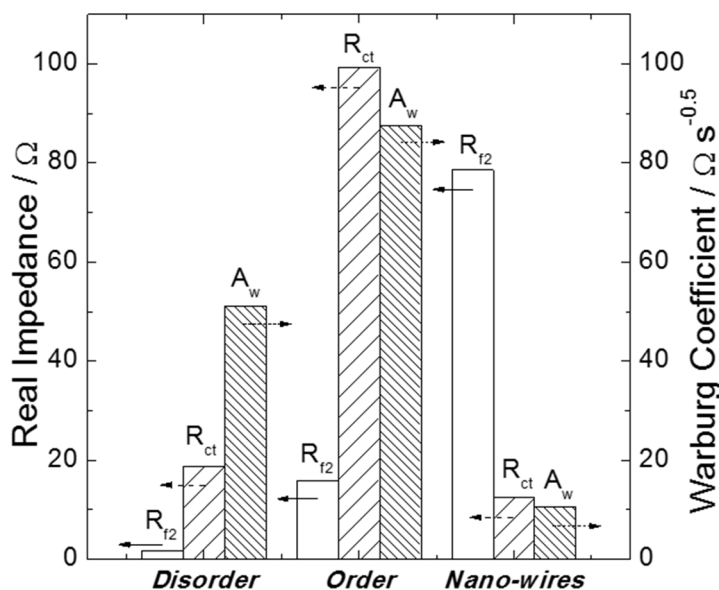
Figure 4.9. Changes in individual real impedances and Warburg coefficient with the disordered and ordered structure, and its nano-structured electrode

A closer look at the changes in the resistances measured in the composite electrodes and nano-structured electrode shows that the resistance R_{ct} from the charge-transfer reaction and the Warburg coefficient Aw reduced. In the case of the charge-transfer reaction, the resistance of the nano-structured electrode was ca. 1.5 times smaller than that of the disordered structure composite electrode. In addition, the Warburg coefficient of the nano-structured electrode was ca. 4.8 times lower compared to the disordered structure composite electrode. This indicates that the strategy employed to reduce the impedances with the reduced diffusion length and the increased active surface area is successful.

However, it is also noteworthy that the resistance from the lithium migration through the multilayer surface films increased significantly. Especially, the resistance of the inner compact interphase, R_2, became the largest elementary impedance. It is increased by ca. 5.0 times compared to that of the ordered structure. The most probable reason for this increase of the surface film resistances is the oxidation of the electrolyte. It is well-known that the high voltage operation of the $LiNi_{0.5}Mn_{1.5}O_4$ spinel materials over 4.3 V (vs. Li/Li^+) oxidizes the liquid-carbonate electrolyte.[64] This detrimental reaction occurs during cycling, and thus leads to increasing the passivation layers on the surface. The increased surface area of the nano-structured electrode aggravates this undesirable process.[11-12]

Notwithstanding the deteriorated surface film resistance, the origin of the improved rate performance (or power density) in the nano-structured electrode (Figure 4.7) is still reasonably explained with the reduced the charge-transfer and diffusion resistances. The highest frequencies of the arc from the charge-transfer reaction and the inclined line for the diffusion step were estimated to be 2.5 Hz and 0.25 Hz, respectively (Figure 4.8). This

implies that the charge-transfer reaction starts to dominate the discharging transient only after 0.4 seconds; and, the diffusion step after 4 seconds. However, for the further enhancement of the nano-structured $LiNi_{0.5}Mn_{1.5}O_4$ spinel materials as battery electrodes, it is quite clear that the surface modifications, which stabilize the interface between the electrode and electrolyte, should be followed. The nano-structured electrode shows strong evidence of Mn^{3+} ions at the surface of $LiNi_{0.5}Mn_{1.5}O_4$, which can lead to Mn^{2+} dissolving into the electrolyte and migrating to the anode.[13, 45, 65-66] The long term cycling of the nano-structured $LiNi_{0.5}Mn_{1.5}O_4$ spinel and its surface characteristics will be discussed in a separate paper.

4.4. Conclusion

In this work, dependence of the contribution of elementary impedances to total dc polarization on battery discharging process was successfully analyzed with two different structures of the $LiNi_{0.5}Mn_{1.5}O_4$ spinel materials, disordered (space group, F d -3 m) and ordered (space group, P 4_3 3 2) structures, from a combination of electrochemical impedance spectroscopy and theoretical analysis of the equivalent circuit. The charge-transfer and solid-state diffusion resistances proved to be the important factors in the course of high-rate battery discharging of the $LiNi_{0.5}Mn_{1.5}O_4$ spinel materials. Especially in the case of the ordered structure, it was demonstrated that the charge-transfer resistance has the most severe effect on the total dc polarization. Moreover, in order to increase the electrochemically active surface area and reduce the diffusion lengths, the one-dimensional nano-structured electrode was prepared via sol-gel based template synthesis. The nano-structured electrodes prepared in this study significantly improved the rate performance of

the $LiNi_{0.5}Mn_{1.5}O_4$ spinel materials with the reduced charge-transfer and diffusion resistances, even though the resistances from the multilayer surface films were deteriorated.

Chapter 4, in full, is a reprint of the material "Effect of Ni/Mn Ordering on Elementary Polarizations of $LiNi_{0.5}Mn_{1.5}O_4$ Spinel and Its Nanostructured Electrode" as it appears in the Journal of the Electrochemical Society, Hyung-Man Cho, Ying Shirley Meng, 2013, 160, A1482. The dissertation author was the primary investigator and author of this paper. All the experiment and writing were performed by the author.

Chapter 5. Effect of Surface Modification on Nano-Structured LiNi$_{0.5}$Mn$_{1.5}$O$_4$ Spinel Materials

In this chapter, the spinel-phase oxide LiNi$_{0.5}$Mn$_{1.5}$O$_4$ (LNMO), a high energy electrode material currently being explored for use in lithium-ion batteries, was prepared using a sol-gel based template synthesis to yield nanowire morphology. Research has shown that extensive electrolyte decomposition and the formation of a surface passivation layer results when LiNi$_{0.5}$Mn$_{1.5}$O$_4$ is implemented in electrochemical cells. As a result of the high surface area associated with nanoparticles, manganese ions dissolution results in capacity fading over prolonged cycling. In order to prevent these detrimental effects and not compromise electrochemical performance, TiO$_2$ and Al$_2$O$_3$ thin films were deposited using atomic layer deposition (ALD) on the surface of LiNi$_{0.5}$Mn$_{1.5}$O$_4$ particles.

5.1. Introduction

The improvement of lithiation/delithiation kinetics can be ascribed to a sharp reduction in the characteristic time constant (t=L^2/D; L = diffusion length, D = diffusion constant). The time t for intercalation decreases with the square of the particle size upon reduction of micrometer dimensions. In addition, a large surface area permits extensive electrode-electrolyte contact, leading to a high lithium-ion flux across the interface. As a result of the shortened electron pathway through the active electrode material, the electrical resistance of nano-sized materials is significantly less than particles of micron-sized regime. The implementation of nano-particulate materials results in various benefits,

however deleterious aspects can be intensified. For example, the increase in surface area results in an escalation in electrode-electrolyte side reactions. This phenomenon is augmented at both high (> 4.3 V vs. Li/Li$^+$) and low (< 1.0 V vs. Li/Li$^+$) operating potentials.[59] For this reason, most of previous nano-structured materials research was limited to the electrodes with the low operating voltages, such as, most of anodes[69-71], LiFePO$_4$[72], etc.

To overcome this problem, surface modification of the material is required for the stable interface between the electrolyte and electrodes.[73-75] Recently, various materials have been investigated as possible coatings on the LiNi$_{0.5}$Mn$_{1.5}$O$_4$ electrodes. Metal oxides[74, 76-81] and polymer[82-83] coatings have been employed as possible materials to prevent manganese dissolution. Carbon has been explored as an additive to both prevent dissolution as well as increase electronic conductivity.[84] Various surface modification methods, such as physical vapor deposition or wet-chemistry have been utilized with the aim of improving interfacial properties. However, those methods have limitations that include nonconformity and unwanted phase transformations due to inter-diffusion of the elements during high temperature operation. Unlike other surface modification methods, atomic layer deposition (ALD) is a particularly useful method for deposition of conformal thin films with a high degree of thickness tenability.[85-89] The low temperature process implements a coating only at the surface, thus preventing unpredictable changes in the bulk. While the use of ALD to deposit protective layers on conventional LiNi$_{0.5}$Mn$_{1.5}$O$_4$ electrodes containing both carbon and binding additives,[80-81] there exists an absence of publications concerning electrodes without such additives. In the present study, the

nanowire $LiNi_{0.5}Mn_{1.5}O_4$ cathode material is prepared and probed without such additives, allowing for investigation of nano-size effects.

Prior studies indicate that strong deviation of electrochemical properties will result when cathode particles are reduced from the micron-regime to that of the nano.[71, 90] However, there remains a dearth of quantitative understanding of the degree that reduction to nano-size affects elementary electrochemical parameters. This work provides critical insights in the analysis of lithium-ion transport kinetics of nano-structured materials and analytical studies concerning ALD surface modifications to successively inhibit deleterious side-reactions. Following surface modification of the $LiNi_{0.5}Mn_{1.5}O_4$ cathode material, the elementary resistances involved in cell operation have been quantitatively investigated.

5.2. Experimental

The spinel-phase material $LiNi_{0.5}Mn_{1.5}O_4$ with nanowire morphology was prepared using a sol-gel based template synthesis[38] (Figure 3.1). A commercially available polycarbonate membrane with a nominal pore diameter of 200 nm (Whatman, P/N : 7060-2502) was used as the template. The sol solution was prepared using a stoichiometric mixture of nickel acetate tetrahydrate (1.867 g), manganese acetate tetrahydrate (5.514 g), and lithium acetate diacetate (1.530 g) dissolved in deionized water (100 ml) with 0.5 wt.% polyvinylalcohol (PVA). All chemicals were purchased from Aldrich and used as received. The template filled with the as-prepared solution was placed on a Pt foil current collector, and dried overnight at 70 °C. The template was removed using an oxygen plasma etching system (Trion RIE/ICP dry etcher) under the following operating conditions: 50 sccm O_2

flow rate, 100 mTorr O_2 pressure, 150 W RF power, and an etching time of 2 hours. Finally, the nanowire electrode was crystallized at 800 °C for 1 hour.

TiO_2 and Al_2O_3 thin films were deposited on the as-prepared nanowire electrodes using atomic layer deposition (Beneq TFS200). Titanium tetrachloride and water were used as the precursors for the TiO_2 deposition. Deposition of Al_2O_3 required the use of trimethylaluminum and water as precursor reagents. Both deposition experiments employed N_2 as the carrier gas and were carried out at 250 °C.

Scanning electron microscope (SEM) (Phillips, XL30) and transmission electron microscope (TEM) (FEI Tecnai G2 Sphera cryo-electron microscope) were utilized in order to examine particle morphology and size distribution. The chemical composition was determined using an energy dispersive X-ray detector (EDX) equipped in the SEM. Crystallinity of the samples was examined by X-ray diffraction (XRD) (Bruker D8) with Cu Kα radiation. XRD data was gathered in the range of $2\theta = 10 - 80$ °, at a scan rate of 0.02 ° s^{-1}. The refinement of the XRD data was carried out using the Rietveld method in the FullProf software package suite. The Ni/Mn molar ratio in the solid and electrolyte samples was characterized by inductively coupled plasma optical emission spectroscopy (ICP-OES) (Perkin-Elmer Plasma 3700).

A custom-made three-electrode cell was employed for electrochemical experiments.[47-48, 91] In order to remove the effect of the lithium metal counter electrode on the electrochemistry, a three-electrode cell configuration is necessary. This effect is reflected in impedance analysis, as the impedance from the counter electrode can influence the working electrode properties. As a result, we employed the three-electrode cell configuration for impedance experiments. Electrochemical experiments such as

galvanostatic cycling and C-rate determination, a two electrode cell configuration was employed using the $LiNi_{0.5}Mn_{1.5}O_4$ nanowire cathode and lithium metal anode. Nano-structured electrodes and lithium metal foil were used for the positive and negative electrodes, respectively. A 1 M solution of lithium hexafluorophosphate ($LiPF_6$) dissolved in a 50/50 (v/v) mixture of ethylene carbonate (EC) and dimethyl carbonate (DMC) was used as electrolyte. The electrochemical cells were assembled in an argon filled glove box (MBraun) (H_2O concentration < 1 ppm). The specific capacity in this work was calculated on the basis of the active mass of nanowire electrode. The mass of each electrode including Pt substrate was estimated statistically by measuring ten times, respectively, using a micro balance (Shimadzu, AUW120D), followed by calculation of the average mass value and variance. The active mass of each nanowire electrodes was obtained by mechanical removal from the Pt substrate. The average loading of active mass in the electrodes was found to be 0.00081 g (= 0.81 mg) and had a range of 0.00080 – 0.00082 g (= 0.80 – 0.82 mg). A Solartron 1287 electrochemical interface was used to perform the galvanostatic/potentiostatic experiments. Electrochemical impedance experiments utilized the Solartron 1287 electrochemical interface, coupled with a Solartron 1260 frequency response analyser. Electrochemical impedance spectroscopy was performed in the frequency range from 100 kHz to 10 mHz at a cell potential of 4.77 V (vs. Li/Li^+) using a signal with an amplitude of 10 mV.

5.3. Results and Discussion

5.3.1. Characterization of Nano-Structured Electrode Materials

(a)
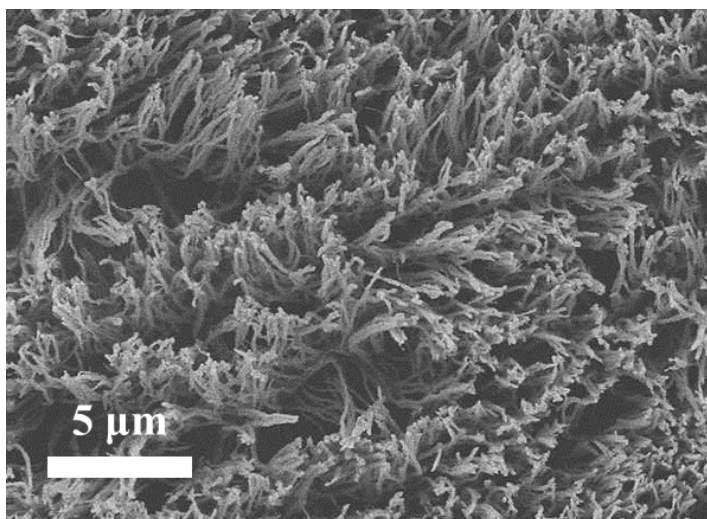
(b)
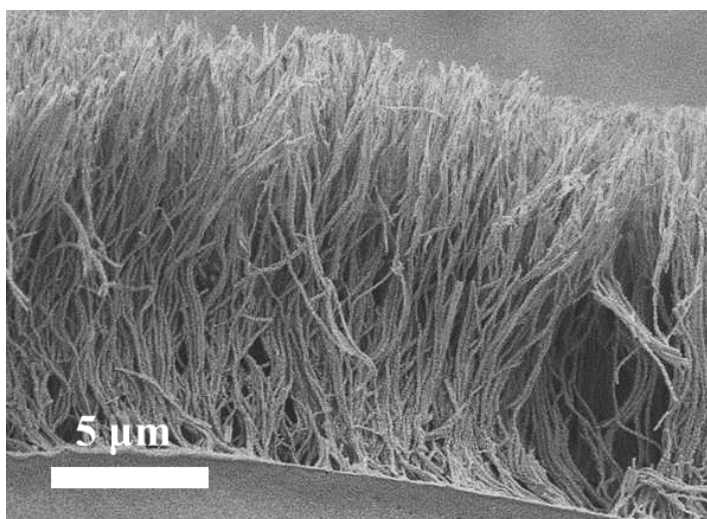
Figure 5.1. Scanning electron micrographs of (a) top and (b) cross-sectional views of LiNi$_{0.5}$Mn$_{1.5}$O$_4$ nanowire electrode prepared via the sol-gel based template synthesis method
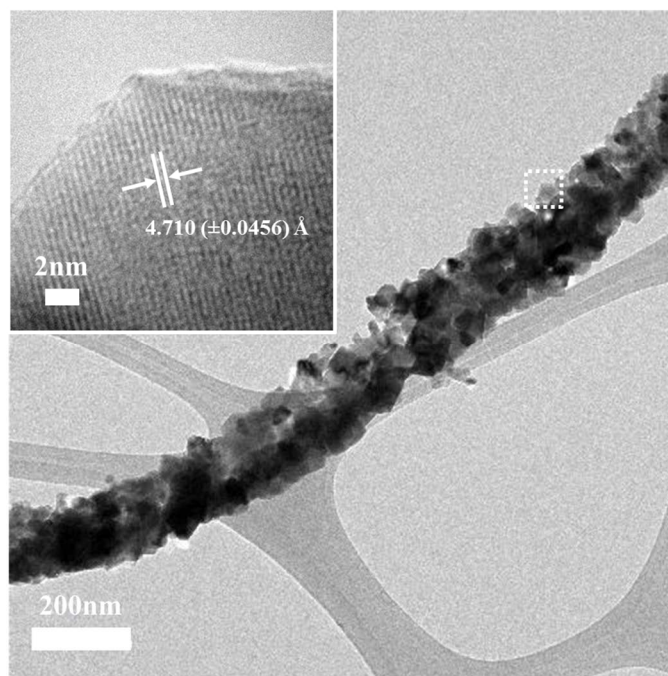
Figure 5.2. Transmission electron micrographs of electron micrographs of LiNi$_{0.5}$Mn$_{1.5}$O$_4$ nanowire electrode prepared via sol-gel based template synthesis method
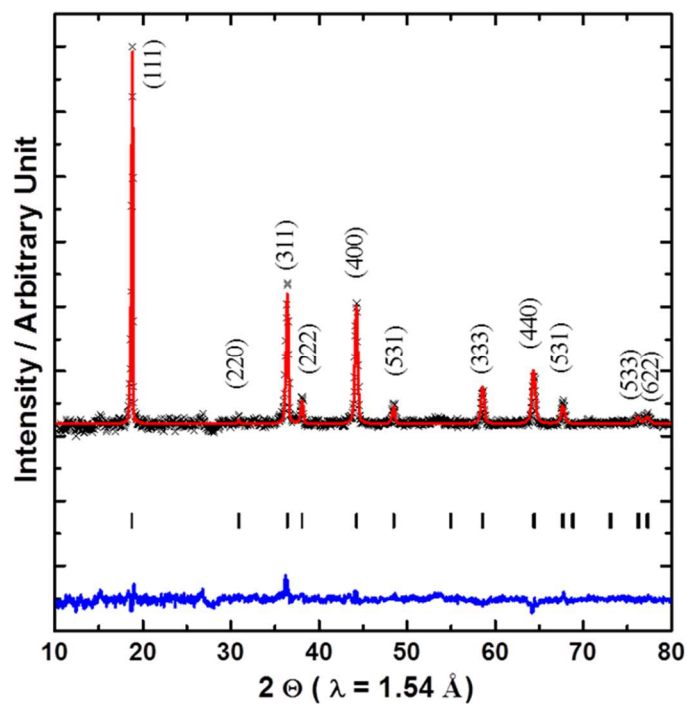
Figure 5.3. The Rietveld refinement results from XRD patterns collected from LiNi$_{0.5}$Mn$_{1.5}$O$_4$ nanowire electrodes. The black crosses represent the observed pattern, the red line corresponds to the calculated diffraction pattern and the blue is the difference

The sol-gel based template synthesis is shown schematically in Figure 3.1. Typical morphology of the as-prepared nanowire electrode is observed by SEM (Figure 5.1(a) and (b)). From the cross-sectional view of Figure 5.1(b), it is revealed that the nanowires are uniformly protruding from an underlying Pt current collector substrate. The average diameter of each nanowire was determined to be ~140 nm with a length of approximately 13 μm. The TEM images in Figure 5.2 detail the fine morphology of the nanowire, which is composed of crystalline particles with an average size of 47 nm and range within 30 - 80 nm. The particle size was estimated statistically by counting at least 30 different sample regions from the TEM images, followed by calculation of the average size. The nanowires have a polycrystalline structure with nano-size crystallites of different orientations. A legible lattice fringe of 0.47 nm can be observed from the locally magnified TEM images (the inset of Figure 5.2), which is consistent with the (111) inter-planar spacing of the disordered structured $LiNi_{0.5}Mn_{1.5}O_4$ spinel materials. It should be noted that the nanowire electrodes in this study offer an unbiased ability to study the nano-size effect, as additives to improve electronic conductivity and binding agents have been removed.

The structure of the as-prepared nanowires was characterized using powder X-ray diffraction following mechanical removal from the Pt current collector, as shown in Figure 5.3. The disordered $LiNi_{0.5}Mn_{1.5}O_4$ spinel material has a cubic crystal structure with space group F d -3 m. The lithium atoms occupy the tetrahedral sites (Wyckoff position: 8a) while the disordered nickel and manganese atoms occupy the octahedral sties (Wyckoff position: 16d).[4] Rietveld refinement was performed and the refined parameters with reliability factors are presented in Table 5.1. A relatively high R_b factor was obtained in the refinement, which is likely the result of broadened XRD peak patterns due to nano-size

Table 5.1. Parameters and reliability factors obtained by the Rietveld refinement of nanowire electrode, from Figure 5.3

a = b = c = 8.192043 Å , α = β = γ = 90 ° , F d -3 m S						
Label	Atom	X	Y	Z	B	Occ
Li1	Li	0.37500	0.37500	0.37500	0.00000	0.96074
Ni1	Ni	0.37500	0.37500	0.37500	0.00000	0.03926
Li2	Li	0.00000	0.00000	0.00000	1.77179	0.03926
Ni2	Ni	0.00000	0.00000	0.00000	1.77179	0.46074
Mn2	Mn	0.00000	0.00000	0.00000	1.77179	1.50000
O3	O	0.24183	0.24183	0.24183	0.00000	4.00000
Conventional Rietveld Reliability Factor : R_{wp}: 3.63, R_b: 10.06						

effect.[41] The particle size was calculated to be 41 nm using Scherrer's formula[41, 92] (against the (111) peak):

$$L = 0.9\,\lambda\,/\,B\cos\theta$$

where λ is the wavelength of the X-ray and B is full width at half maximum (FWHM) value. This calculated value is consistent to the estimated particle size obtained from the TEM images.

Electrochemical charge and discharge was performed in the potential range of 3.5 - 4.85 V (vs. Li/Li^{+}) with applied current rate of C/7.5 using $LiNi_{0.5}Mn_{1.5}O_4$ (non-coated) nanowires as the positive electrode (Figure 5.4(a)). The plateau at ~4.7 V (vs. Li/Li^{+}) arises from the $Ni^{2+/4+}$ redox couple while the plateau at ~4.0 V is the result of the $Mn^{3+/4+}$ couple.

Capacity arising from the voltage plateau at ~4.0 V (vs. Li/Li$^+$) has been used to estimate the amount of Mn^{3+} in the LiNi$_{0.5}$Mn$_{1.5}$O$_4$ spinel materials. The origin of Mn(III) ions has been ascribed to transition metal (TM) ion substitutions[10, 93], various crystallization temperatures[12, 94], and different cooling rates[45] during heat treatment. In this work, all the nanowire electrodes was prepared at the same calcination temperature, 800 °C, and same cooling rate. ALD is also a well-known method which prevent any unpredictable changes on the coated materials because of its low operating temperature. Therefore, we can easily estimate that the amount of Mn^{3+} is same on those samples. Moreover, our group previously studied non-equilibrium structural dynamics in LiNi$_{0.5}$Mn$_{1.5}$O$_4$ spinel materials under operando conditions using coherent X-ray diffraction imaging (CXDI) and it was revealed that there is the sharp discrepancy between electrochemistry and structural changes during fast charging/discharging process.[23] It disclosed that during the fast charging process the ionic blockade layer formed at the surface of the materials, thus actual overall phase transformation does not reached at that specific state which the electrochemical signal indicates. In this study, as-prepared nano-wire LiNi$_{0.5}$Mn$_{1.5}$O$_4$ electrode without carbon and binding additives has the benefit allowing for investigation of nano-size effects, but the poor electrical conductivity leads large polarizations. Hence, in the present study, the plateau at ~4.0 V (vs. Li/Li$^+$) cannot properly represent the amount of Mn^{3+} in the nanowire electrodes. While the electrochemical profiles show similar plateau regions with the typical composite electrodes (with added carbon additive and binder), the irreversible capacity occurs not exclusively in the first cycle, but also in consecutive cycles. It is hypothesized that this is the result of a side reaction between the electrolyte and active electrode material at the electrode/electrolyte interface. By plotting the differential capacity (dQ/dV) vs. cell

(a)
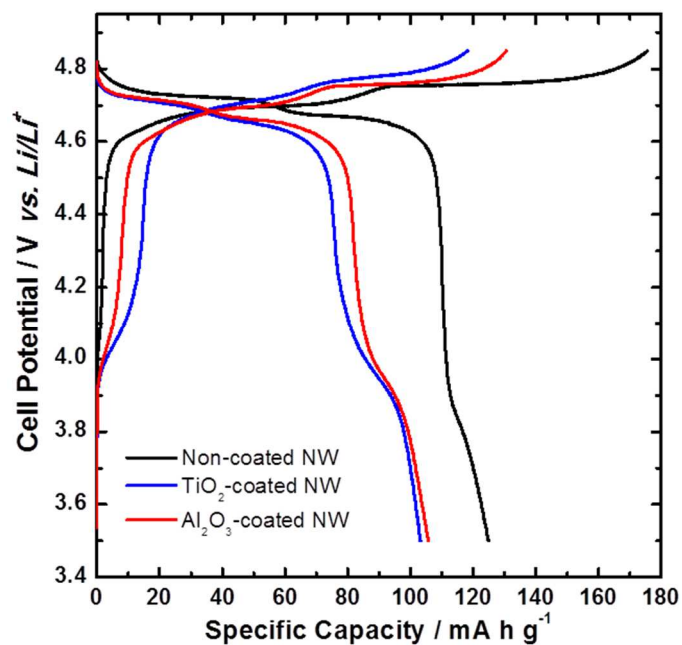
(b)
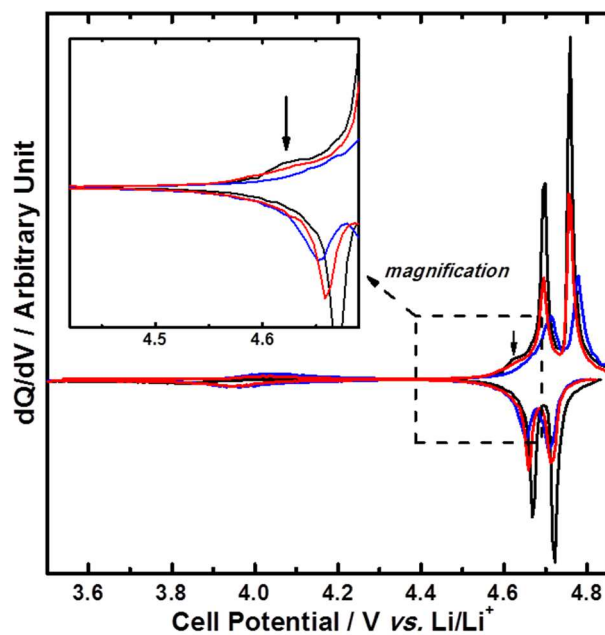
Figure 5.4. (a) Electrochemical voltage profiles between 3.5 – 4.85 V (vs. Li/Li$^+$) for non-coated nanowire at 1/7.5 C rate (black), and TiO$_2$-coated (blue) and Al$_2$O$_3$-coated (red) nanowires. (b) Differential capacity (dQ/dV) plot of nanowires

potential (V), a peak is observed above 4.6 V in the first charging profile, indicating that a side reaction is indeed occurring. This peak is not observed when using conventional powder $LiNi_{0.5}Mn_{1.5}O_4$ and we purport its evolution to be related to electrode activation. At particularly high potentials, the electrolyte can decompose and form a layer on the surface of the electrode particles. Previous reports have described that this can be significantly detrimental to lithium-ion conduction through the electrode/electrolyte interface.[45, 92] Prolonged operation at this high voltage can exacerbate these types of side reactions. In addition, reduction of the manganese(III) ions at the surface of $LiNi_{0.5}Mn_{1.5}O_4$ leads to manganese(II) ions, which can dissolve in the electrolyte. Manganese(II) ions proceed to diffuse through the electrolyte to the lithium metal anode and plate on the surface.[13, 45, 66] This leads to an increase in the internal resistance of the cell and as a result, poor battery performance. The particle morphology does not change following electrochemical cycling, but Rietveld refinement shows that the lattice parameter and R_b increase. This is likely the result of augmentation of the nanosize effect and Manganese(II) dissolution. In addition, a recent publication reports structural changes in the electrode during the first cycle, which has been purported to be migration of transition metal ions into empty octahedral sites to form Mn_3O_4-like and rocksalt-like structures.[95] In the case of $LiNi_{0.5}Mn_{1.5}O_4$ nano-wire, the surface area is remarkably higher, which can result in a large side reaction peak in the charging profile. However, the exact nature of 4.6 V peak in dQ/dV profile in the charging process is still open to discussion.

5.3.2. Surface Modification – Atomic Layer Deposition (ALD)

In order to prevent the deleterious effects of electrolyte decomposition and cation dissolution, the interface between the electrolyte and the active materials must be modified. Atomic layer deposition (ALD) is a technology that has been repeatedly shown to be extremely useful in the surface modification of complex nano-structured materials.[88, 96] This technique is based on successive, surface-controlled reactions from gaseous reagents to produce thin films and overlayers in the nanometer range with perfect conformality and controllability. Figures 5.5(a) and (b) show images obtained using SEM as well as energy dispersive X-ray spectroscopy (EDX) analysis of the TiO_2 and Al_2O_3 coated nanowire electrodes. Following successful deposition of TiO_2 and Al_2O_3 thin films, the nanowires were found to be in the same protruding fashion from the Pt substrate. The thickness of the thin film is directly proportional to the number of ALD cycles. The growth rate of both TiO_2 and Al_2O_3 thin films on the nanowire electrodes was calculated as shown in figure 5.5c. Each ALD cycle deposits a uniform TiO_2 and Al_2O_3 thin film layer of approximately 0.0389 nm (= 0.389 Å) and 0.0816 nm (= 0.816 Å) in thickness, respectively on the nanowire $LiNi_{0.5}Mn_{1.5}O_4$ surface. As shown by TEM (Figure 5.6(a) and (b) for TiO_2 and Al_2O_3, respectively), the surface of the coated nanowires is highly smooth and uniform.

To determine the effect of the deposition layers on the electrochemical performance of nanowire $LiNi_{0.5}Mn_{1.5}O_4$ electrodes, galvanostatic charge/discharge experiments were performed with an applied current rate of C/7.5 in the potential range of 3.5 – 4.85 V (vs. Li/Li$^+$). Figure 4a details a TiO_2-coated nanowire electrode with an approximate coating thickness of 0.43 nm (= 4.3 Å; 11 cycles), and an Al_2O_3-coated nanowire electrode with a coating thickness of ~0.41 nm (= 4.1 Å; 5 cycles). Electrodes layered with either thin film material were found to exhibit typical redox behavior of $LiNi_{0.5}Mn_{1.5}O_4$ spinel material,

(a)
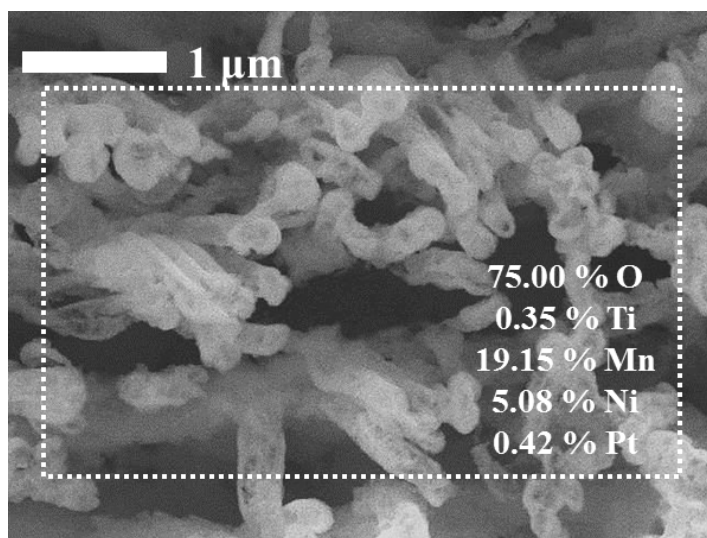
(b)
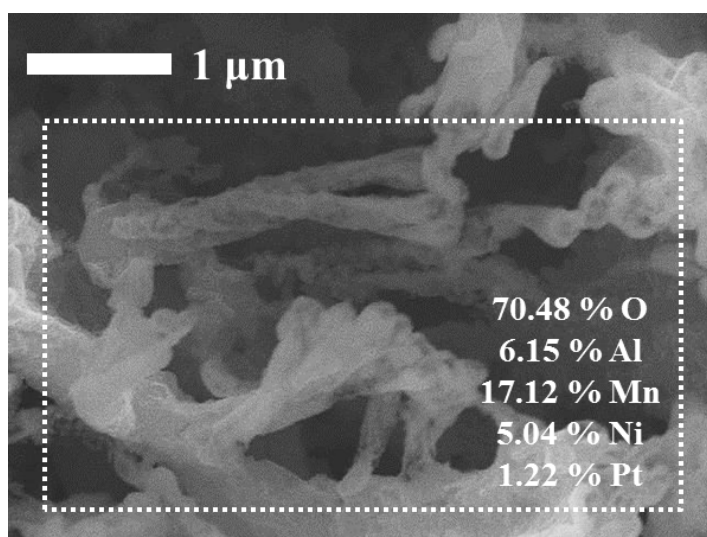
Figure 5.5. Top views (SEM) of ALD coated nanowire electrodes (a) TiO_2 ALD 11 cycles (b) Al_2O_3 ALD 30 cycles. The insets indicate the percentage of each component from EDX analysis. (c) Various deposition thickness as a function of ALD cycles

(c)
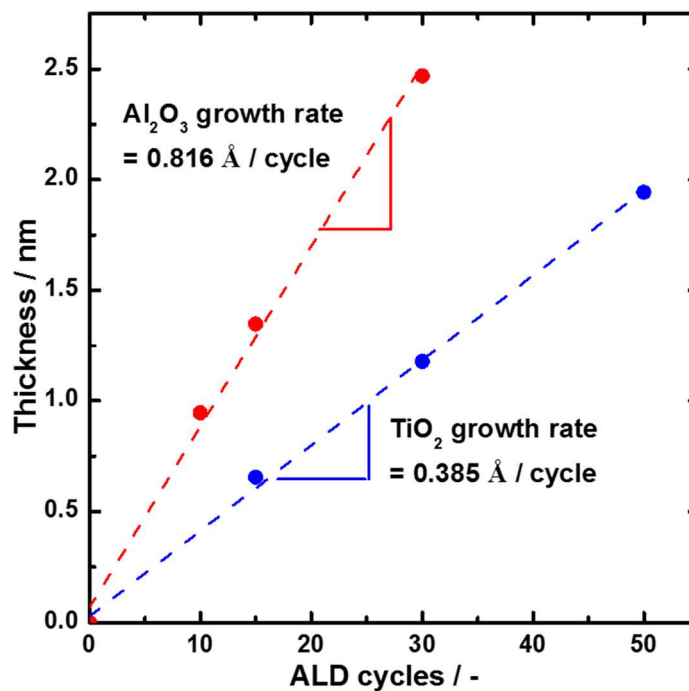
Figure 5.5. Top views (SEM) of ALD coated nanowire electrodes (a) TiO_2 ALD 11 cycles (b) Al_2O_3 ALD 30 cycles. The insets indicate the percentage of each component from EDX analysis. (c) Various deposition thickness as a function of ALD cycles, continued.

(a)
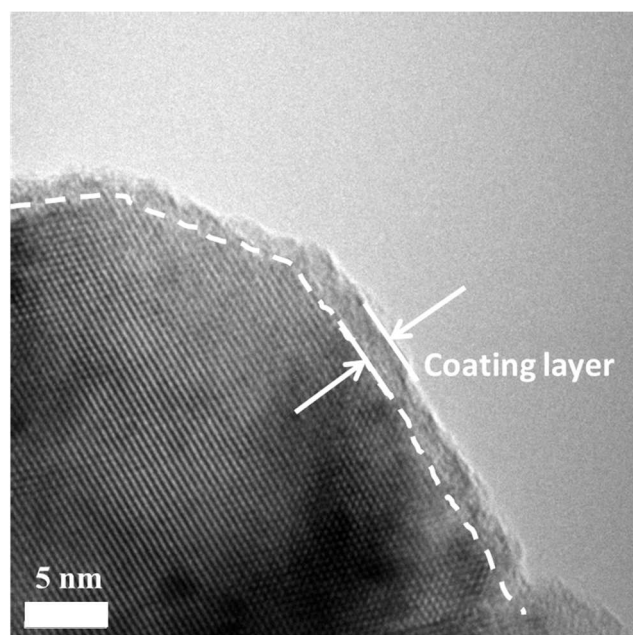
(b)
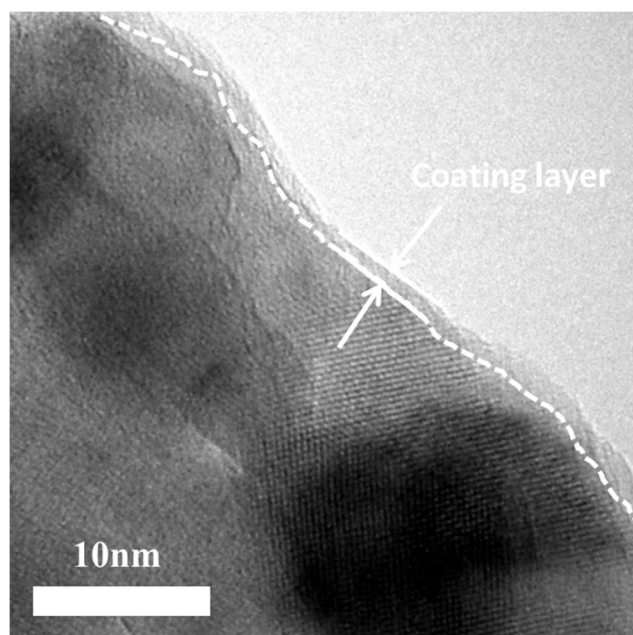
Figure 5.6. Transmission electron micrographs of (a) TiO_2 ALD coated (50 ALD cycles) and (b) Al_2O_3 ALD coated (15 ALD cycles) nanowires

such as the $Ni^{2+/4+}$ and $Mn^{3+/4+}$ plateaus at around 4.7 V and 4.0 V (vs. Li/Li^+), respectively. It was found that the irreversible capacity fade is significantly reduced as a result of coating the nanowire $LiNi_{0.5}Mn_{1.5}O_4$ material using atomic layer deposition.

In spite of the considerable effects of volume and surface area of the nano-wire electrode on the electrochemical performance, there is no existing testing method that would allow for the accurate determination of these quantities without damaging the one-dimensional morphology. In lieu of an experimental measurement, the surface area was calculated as follows: as the average diameter of the nanowire is 140 nm (= 2r) and the length is 13 µm (= L), the outer rectangular area of a nanowire is 5.72 x 10^{-8} cm^2 (= $2\pi r$ x L). The average number of pores in the polycarbonate (PC) template is 4.7 x 10^8 pores/cm^2. In addition, the diameter of the electrode cutout is 14 mm, leading to a surface area of 1.54 cm^2 (= π x 0.7^2). Hence, the number of nanowires in the electrode is 7.24 x 10^8 wires (= 4.7 x 10^8 x 1.54), leading to a total outer rectangular area of nanowires to be 41.41 cm^2 (= (7.24 x 10^8) x (5.72 x 10^{-8})). Therefore, the total surface of area is 42.95 cm^2 (= 41.41 + 1.54). Using the aforementioned values, the superficial volume of a single nanowire is calculated to be 8.005 x 10^{-13} cm^3 (=πr^2 x L) and the total volume of nanowires is 5.79 x 10^{-4} cm^3 (= (8.005 x 10^{-13} cm^3) x (7.24 x 10^8 wires)). The average thickness of substrate layer is 200 nm, leading to the volume of 0.308 x 10^{-4} cm^3 (= 1.54 x (200 x 10^{-7})). Therefore, the total volume of electrode is 6.098 x 10^{-4} cm^3. Accordingly, as shown in Figure 5.4 (a), the discharge capacity of non-coated nanowire is 101.12 mA h g^{-1}, 134.31 mA h cm^{-3}, and 1.907 x 10^{-3} mA h cm^{-2}. The discharge capacity of the TiO_2-coated electrode is 103.17 mA h g^{-1}, 138.73 mA h cm^{-3}, and 1.969 x 10^{-3} mA h cm^{-2}. Nanowire electrodes coated with

Al_2O_3 lead to discharge capacities of 105.72 mA h g^{-1}, 140.43 mA h cm^{-3}, and 1.994 x 10^{-3} mA h cm^{-2}.

In addition, the electrode/electrolyte side reaction was effectively prevented, as shown by the absence of a peak at ~4.6 V in the differential capacity plot (Figure 5.4b). Aluminum oxide is a well-known insulating material, and as such it was hypothesized that a thick layer of Al_2O_3 would inhibit lithium ion movement and dramatically increase the internal resistance. However, the formation of a Li-Al-O film was found to be an effective lithium ion conductor and electronic insulator.[87, 97] The surface modification by TiO_2 coating is widely adopted in order to prevent cation dissolution and electrolyte decomposition. However, there are no reports about the lithium ionic conduction mechanism through TiO_2 phase. As the thickness of the TiO_2 coating layer is less than 0.5 nm, we purport that this TiO_2 can form a Li-Ti-O glass phase during the lithiation, analogous to that of Li-Al-O films. This resulted in a retention of electrochemical performance as well as prevention of electrolyte decomposition and manganese ion dissolution.

To further investigate the effect of the ALD coating on the nanowire electrodes, experiments correlating capacity retention with various discharge rates were performed, as shown in Figure 5.7. A cell utilizing a non-coated nanowire electrode shows not merely inferior rate capability (less than 10 mA h g^{-1} at a rate of 1 C), but also significant capacity fading during prolonged cycling. In addition, the coulombic efficiency was found to be exceptionally poor, dropping to nearly 60 % at the 30th cycle. It has been postulated that the poor electrochemical performance is a result of increased electrolyte decomposition and cation dissolution associated with the increased active surface area of the nanowires.
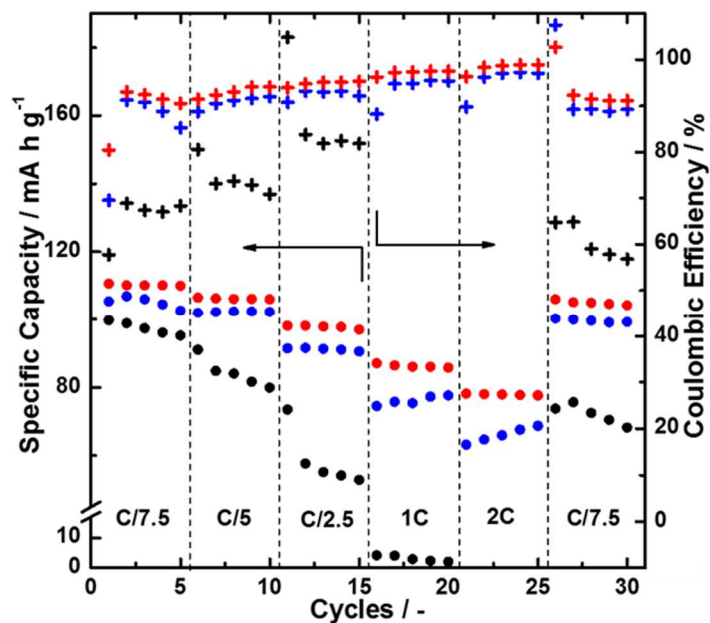
Figure 5.7. Specific capacity versus cycle number plot at different charge and discharge rates. (black: non-coated NW, blue: TiO_2-coated NW, red: Al_2O_3-coated NW)
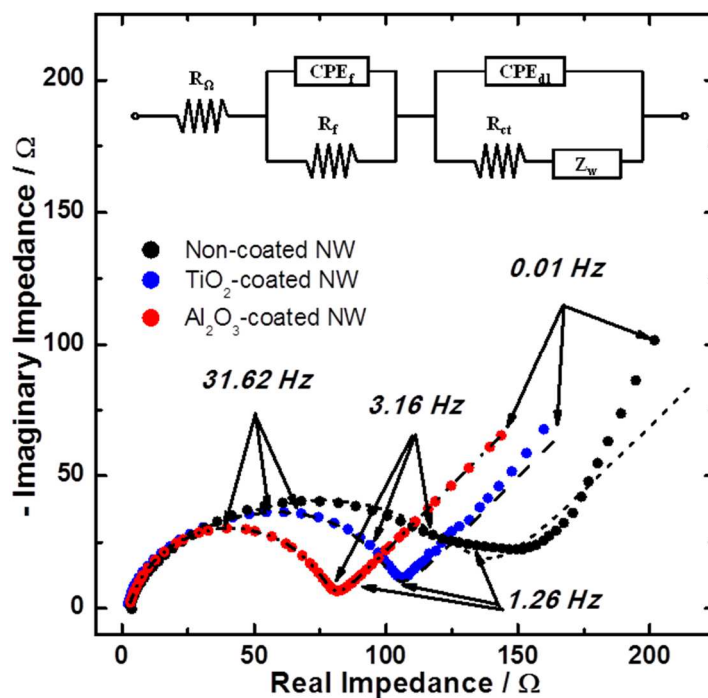
Figure 5.8. Impedance spectra of nano-structured electrodes, obtained at a cell potential of 4.77 V (vs. Li/Li^+). The insets are the equivalent circuits to model its reactions. Dotted lines were determined from the CNLS fittings

Coating the nanowire with either TiO_2 or Al_2O_3 resulted in starkly different electrochemical performance compared to non-coated $LiNi_{0.5}Mn_{1.5}O_4$ nanowire electrode. This is exemplified in a much improved observed coulombic efficiency of > 90 % at 25th cycle in Figure 5.7 (e.g. 98.8 % in the Al_2O_3 coated nanowire). In the case of the Al_2O_3 coated nanowire electrode, the discharging capacity at a 1 C rate still presents 99 mA h g^{-1}.

In order to probe the effect of surface modification by ALD on the electrochemical reaction mechanism, electrochemical impedance spectroscopy (EIS) measurements were performed in the charged state at 4.77 V (vs. Li/Li$^+$), as shown in Figure 5.8. These experiments can help to elucidate the elementary resistances that strongly affect electrochemical performance. The impedance spectra (Nyquist plots) consist of two semicircles: one each in the high and intermediate frequency ranges, and an inclined line at a constant angle to the abscissa. The first semicircle in the high frequency is the result of the lithium migration through the surface film, and the second semicircle in the intermediate frequency originates from the interfacial charge transfer reaction. The inclined line is attributed to solid-state lithium ion diffusion into the active electrode materials. The impedance spectra were modelled using a simplified equivalent circuit as shown in the inset of Figure 5.8. The resistance, R_Ω, represents the uncompensated ohmic resistance. The first pair of resistance and constant phase element (CPE), R_f-CPE_f, indicates that lithium migration occurs through the surface film region. The second pair of resistance and CPE, R_{ct}-CPE_{ct}, is indicative of charge-transfer resistance and double layer capacitance. The Warburg impedance, Z_W, describes the solid-state diffusion step.[40, 56-57] All the electrical parameters in the equivalent circuit were determined from the complex non-linear

least squares (CNLS) fitting method[48, 98-99], and are summarized in the Table 5.2. It is particularly noteworthy that the resistance R_f from the TiO_2 and Al_2O_3 coated nanowires, reduced by about 50 Ω and 70 Ω, respectively. This corresponds to a reduction of approximately 44 % and 67 % when compared to that of the non-coated nanowire electrode. Impedance spectroscopy results indicate that the resistance originating from the surface film region in the charged state (4.77 V vs. Li/Li$^+$) can be significantly reduced by ALD coating on the active materials. A reduction in resistance suggests that electrolyte decomposition at high voltage operation and manganese(III) dissolution have been curtailed.

Table 5.2. Electrical parameters of the working electrodes, determined from the complex non-linear least squares (CNLS) fitting of impedance spectra to the equivalent circuit. This also includes the diffusion coefficient, diffusion length and some calculated values

Positive electrode									
Cell potential	R_Ω	R_f	CPE$_f$		R_{ct}	CPE$_{dl}$		A_ω	
			C	η		C	η		
V (vs. Li/Li$^+$)	Ω	Ω	mF s$^{\eta-1}$		Ω	μF s$^{\eta-1}$		Ω s$^{-0.5}$	
Bare NW		2.82	105	0.295	0.751	24.37	96.5	0.888	30.29
TiO$_2$ ALD	4.77	2.06	58.99	0.158	0.923	39.66	77.5	0.862	25.11
Al$_2$O$_3$ ALD		2.57	34.14	0.108	0.823	41.93	56.9	0.871	23.10

(a)
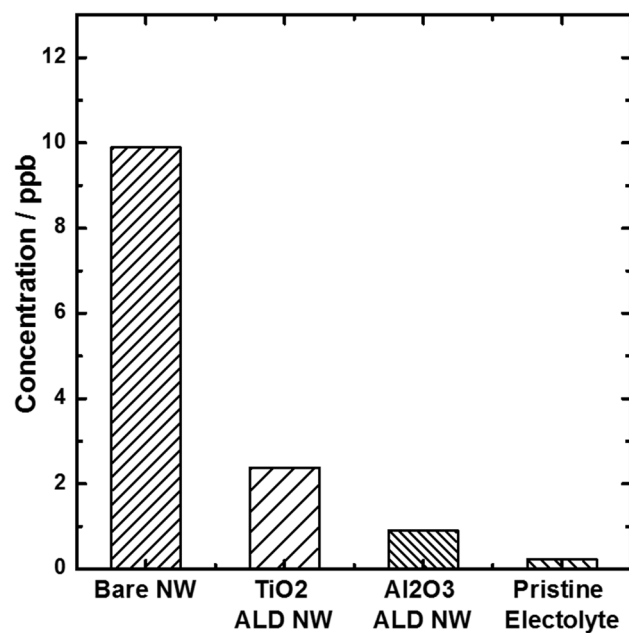
(b)
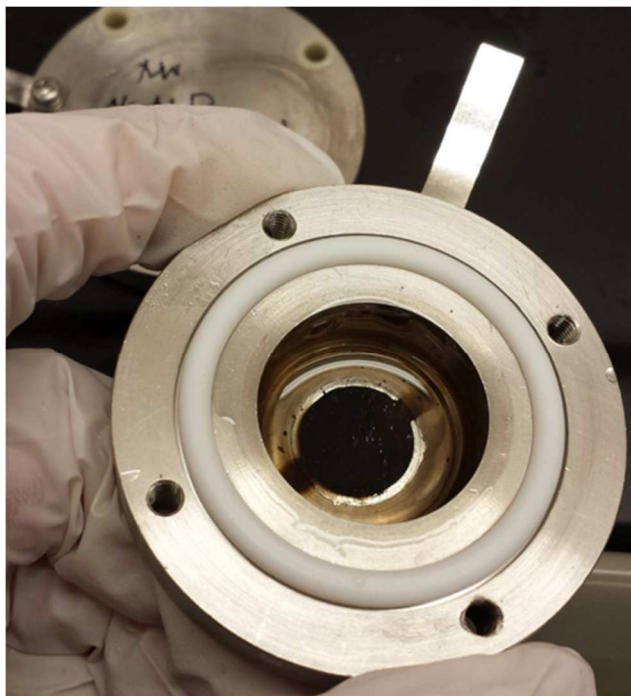
Figure 5.9. (a) Mn dissolution into the electrolytes with the various nanowire electrodes from ICP-OES analysis. Photographs of Li metal counter electrodes after the electrochemical tests (b) without ALD deposition (c) with Al$_2$O$_3$ ALD

(c)
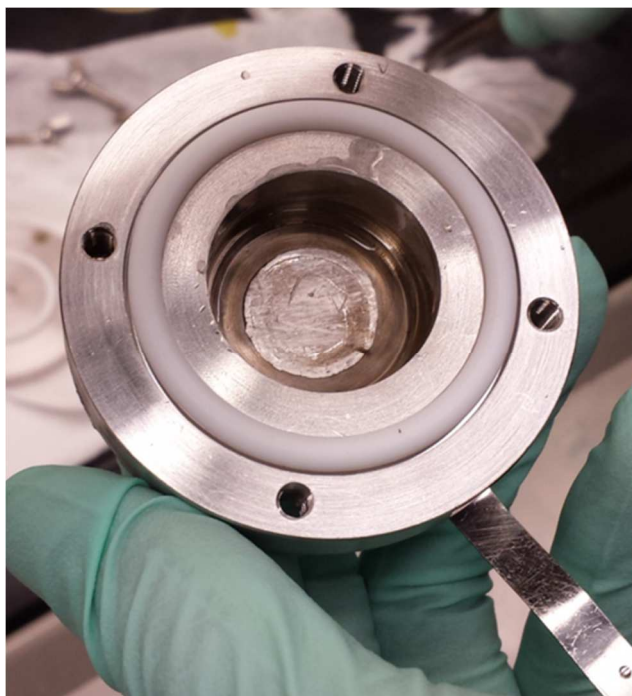
Figure 5.9. (a) Mn dissolution into the electrolytes with the various nanowire electrodes from ICP-OES analysis. Photographs of Li metal counter electrodes after the electrochemical tests (b) without ALD deposition (c) with Al_2O_3 ALD, continued.

In order to investigate the extent of cation dissolution into the electrolyte, the electrochemical cells were disassembled in an argon filled glove box and the electrolyte was separated from the other battery components. Elemental analysis of the electrolyte was performed using inductively coupled plasma optical emission spectrometry (ICP-OES). It was determined that manganese ion dissolution into the electrolyte is alleviated when electrodes are coated with either TiO_2 and Al_2O_3 (Figure 5.9(a)). The concentration of manganese in the electrolyte when using non-coated $LiNi_{0.5}Mn_{1.5}O_4$ electrode was determined to be ~10 ppb after 30 cycles of electrochemical charging and discharging. However, when the nanowires are coated with Al_2O_3 (5 ALD cycles, ~4 nm thickness), the concentration of manganese in the electrolyte decreased to a mere ~1 ppb. Increased cation dissolution was found to result in severe darkening of the lithium metal anode. However, cells using an aluminum oxide coated $LiNi_{0.5}Mn_{1.5}O_4$ cathode resulted in a relatively clean and shiny lithium anode surface. This qualitative observation further reveals how significant a reduction in Manganese(III) dissolution results when coating the nanowires with insulating thin films.

5.4. Conclusion

Our studies have indicated that an increase in surface area of one-dimensional nanowire electrode results in detrimental interfacial side reactions. Protective thin films composed of either titanium dioxide or aluminum oxide were successfully deposited on $LiNi_{0.5}Mn_{1.5}O_4$ nanowire electrodes using atomic layer deposition. The protective layer at the surface of the nanowire makes it possible to not merely decrease the irreversible capacity fade, but also diminish the manganese dissolution during electrochemical cycling.

This results in an acceleration of lithium ion migration through the surface film and a reduction in resistance. Our work gives significant insight in the importance of interface protection for high voltage nano-structured electrode materials.

Chapter 5, in full, is currently being prepared for submission for publication of the material "Effect of Surface Modification on Nano-Structured $LiNi_{0.5}Mn_{1.5}O_4$ Spinel Materials" Hyun-Man Cho, Michael Vincent Chen, Alex C. MacRae, Ying Shirley Meng, The dissertation author was the primary investigator and author of this paper. All the experiment and writing were conducted by the author.

Chapter 6. Implementation of stable surface structures; a promising key to solve capacity fading issues for the high-voltage LiNi$_{0.5}$Mn$_{1.5}$O$_4$

In this chapter, the structural changes at the surface and bulk of LiNi$_{0.5}$Mn$_{1.5}$O$_4$ spinel materials were extensively investigated. The structural stability related to the transition metal migration are compared with LiNi$_{0.5}$Mn$_{1.5}$O$_4$ spinel materials via conventional sol-gel method versus polyol process. The surface and bulk of as-synthesized and cycle-aged disordered LiNi$_{0.5}$Mn$_{1.5}$O$_4$ structures at the fully lithiated/delithiated state were explored using a combination of in situ X-ray absorption spectroscopy (XAS) coupled with aberration-corrected scanning transmission electron microscopy (STEM).

6.1. Introduction

Unique among various high-voltage cathode materials, spinel structured LiNi$_{0.5}$Mn$_{1.5}$O$_4$ materials allow three-dimensional lithium-ion diffusion in its lattice. This has drawn remarkable attention because it enables enhanced diffusion kinetics and makes high-rate capabilities possible.[13, 23, 32-33, 91-92, 100] However, this material exhibits degradation with extended cycling. For example, it is well documented that the LiNi$_{0.5}$Mn$_{1.5}$O$_4$ spinel shows capacity fade, related to Mn^{3+} dissolution from the active materials and electrolyte decomposition during the high voltage operation.[45, 65, 92] There is another possibility that the capacity fading could be derived from the loss of crystallinity during the electrochemical charging/discharging process. In order to prevent the possible degradation mechanisms and subsequently attempt to improve the performance of this material, our group has adopted the polyol process as a new method of synthesizing

$LiNi_{0.5}Mn_{1.5}O_4$ materials. This method, commonly described as the polyol process, is composed of reductive metallic compounds in a liquid alcohol medium, maintained at its boiling point.[101-103] The polyol medium itself acts not only as a solvent in the process but also as a stabilizer, limiting particle growth and prohibiting agglomeration.[66] Especially, this innovative process provides a superior reducing environment, especially for synthesizing $LiNi_{0.5}Mn_{1.5}O_4$ spinel materials..

6.2. Experimental

$LiNi_{0.5}Mn_{1.5}O_4$ nanoparticles with same stoichiometries were prepared via two different synthetic methods; conventional sol-gel method[10, 50, 91] and polyol process. Sol-gel methods: The sol solution were prepared from the stoichiometric mixture of $Ni(CH_3COO)_2 \cdot 4H_2O$ (Aldrich), and $Mn(CH_3COO)_2 \cdot 4H_2O$ (Aldrich) in distilled water. A solution of $LiOH \cdot 2H_2O$ (Aldrich) in distilled water and aqueous solution of citric acid was added dropwise to the metal precursor mixture with a continuous stirring. Next, the pH of the mixed solution was adjusted to 7 by adding an ammonium hydroxide solution. As-prepared sol solution was dried at 70 ^{o}C with a vigorous mechanical stirring. After gel formation, the precursor was further dried in vacuum oven at 120 ^{o}C for overnight, eventually, the resulting gel precursors were decomposed at 500 ^{o}C for 12 hours in air and then calcinated at 900 ^{o}C for 14 hours in air, in sequence. Polyol process: $Ni(CH_3COO)_2 \cdot 4H_2O$, $Mn(CH_3COO)_2 \cdot 4H_2O$, $LiOH \cdot 2H_2O$, and citric acid were added to 100 ml tetraethylene glycol (TTEG) in a stioichiometric molar ratio. The mixture was heated at 280 oC for 3 h in a round bottom flask connected to a refluxing condenser to ensure full activation of the polyol medium. The resulting solution was centrifuged several

times with methanol and subsequently dried at 80 ºC for overnight. The resulting precursors were decomposed at 500 ºC for 12 hours in air and then calcinated at 800 ºC for 1 hour in air.

Powder x-ray diffractions (XRD) of all samples were collected by a laboratory x-ray diffractometer (XRD, Bruker D8) using a Cu Kα radiation. The conditions for the data collection were: continuous scanning of a detector covering an angular range from 10.0 ° to 80.0 ° with a scan rate of 0.02 ° s-1 and wavelengths of λ= 1.54 Å. The Rietveld refinement was done by FullProf.

The chemical compositions of the samples were analyzed by inductive coupled plasma atomic emission spectroscopy (ICP-OES Perkin Elmer Plasma 3700). The instrument is equipped with two monochromators covering the spectral range of 167-785 nm with a grated ruling of 3600 lines/mm. The system is capable of analyzing materials in both organic and aqueous matrices with a detection limit range of less than 1 part per million.

The particle size and morphologies were checked using field emission-scanning electron microscope (FE-SEM, Phillips, XL30) at an acceleration voltage of 15 kV after sputter-coating all the samples with iridium for 6s.

For the composite electrode fabrication, the slurry consisting of 80 wt.% active materials, 10wt. % acetylene carbon black, and 10 wt.% poly(vinylidene fluoride) (PVdF) in N-methyl pyrrolidone (NMP) was pasted on the aluminum foil current collector, and then, dried overnight in a vacuum oven at 80 ºC, and followed by punching and pressed uniaxially. As-prepared electrodes were dried again at 80 ºC for 6 hours before storing them in an argon-filled glovebox (H_2O level of <1 ppm) (MBraun, Germany). For the

electrochemical characterizations, lithium metal (Aldrich) was used for the negative (counter) electrode, and Celgard model C480 separator (Celgard Inc., US) was used as separator. The electrolyte was a 1- M solution of lithium hexafluorophosphate ($LiPF_6$) in a 1:1 volume mixture of ethylene carbonate (EC) and dimethyl carbonate (DMC). The cell used for the electrochemical tests was assembled in a glove box (MBraun, Germany) filled with purified argon gas. The as-prepared cell was charged and discharged between constant potential of 3.50 V and 4.85 V (vs. Li/Li^+) at a rate of C/10 (the theoretical specific capacity of 146.72 mA h g^{-1} of $LiNi_{0.5}Mn_{1.5}O_4$ spinel material was assumed). An Arbin battery cycler was employed to carry out all of the galvanostatic cycling tests.

Electron microscopy work was carried out on a Cs-corrected FEI Titan 80/300-kV TEM/STEM microscope equipped with a Gatan Image Filter Quantum-865. All EELS spectra were acquired at 300 KV and with a beam size of ~0.7 Å. The spectra shown in this work were acquired from a square area of ~ 0.5 × 0.5 nm with an acquisition time of 3 sec and a collection angle of 35 mrad. To minimize possible electron beam irradiation effects, EELS data were acquired from areas without prebeam irradiation. Mn L3 to L2 intensity ratio analysis was done by averaging over 8 to 12 spectra using the method described by Wang et al.[104]

X-ray photoelectron spectrum (XPS) experiment was performed with a monochromatic Al Ka X-ray source (hν = 1486.6 eV) operating at a pressure lower than 10^{-10} Torr. For high-resolution spectra, constant analyzer energy (CAE, pass energy: 50.0 eV) mode was applied, leading to a resolution of 0.1 eV. The acquired spectra were calibrated by fitting C1s photopeak at 285.0 eV and then deconvoluted using CasaXPS software package. All peaks were fit using a Shirley-type background.

In situ XAS experiments were carried out at beamline X-18B at the National Synchrotron Light Source (NSLS). A Si (111) double-crystal monochromator detuned to 30 % of its original maximum intensity to eliminate the high-order harmonics. Mn K-edge (~6539 eV) XAS spectra were collected simultaneously in both fluorescence yield (FY) mode, utilizing a gas ionization chamber as a detector, and in total electron yield (TEY) mode under He gas flow. The cycled cathode electrodes were first washed by the DMC solvent and then mounted on the sample holder of a specially designed cell.[105] Reference spectra of Mn foil were used to maintain energy calibration. X-ray absorption near edge structure (XANES) and extended X-ray absorption fine structure (EXAFS) data were analyzed by the ATHENA software package.[106] The extracted EXAFS signal, $\chi(k)$, was weighted by k^3 to emphasize the high-energy oscillations and then Fourier-transformed in k-ranges of 2.5 to 7 $Å^{-1}$ for Mn to obtain the magnitude plots of the EXAFS spectra in R-space (Å).

Electron microscopy was carried out using the double aberration-corrected scanning TEM (TEAM0.5) microscope operated at an acceleration voltage 80 kV installed at the National Center for Electron Microscopy (NCEM) at the Lawrence Berkeley National Laboratory (LBNL). The images were recorded on a 3 mm diameter specimen mounted to a double-tilt holder in a conventional compu-stage that enables a tilting range of $\pm$ 20 - 25 $^{\circ}$ in combination with the ultrahigh-resolution pole-piece lens employed.

6.3. Results and discussion

In this work, the resulting $LiNi_{0.5}Mn_{1.5}O_4$ via polyol process shows outstanding capacity retention compared to conventional $LiNi_{0.5}Mn_{1.5}O_4$ prepared by sol-gel method.

(a)
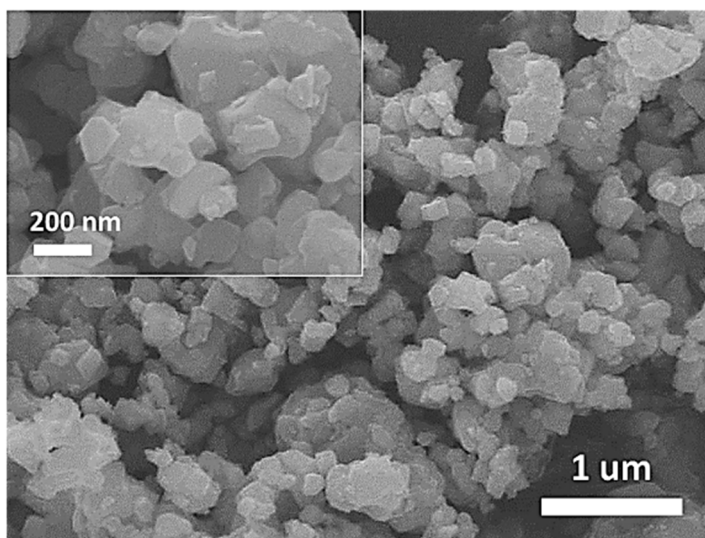
(b)

Figure 6.1. (a) & (b), SEM images of LiNi$_{0.5}$Mn$_{1.5}$O$_4$ via sol-gel and polyol methods. (c) & (d), Rietveld refinement results from XRD patterns. (e) Dependence of capacity retention with cycles at 25 & 55 °C. (f) Mn dissolution into the electrolyte with the cell ageing by ICP-OES analysis

(c)

(d)
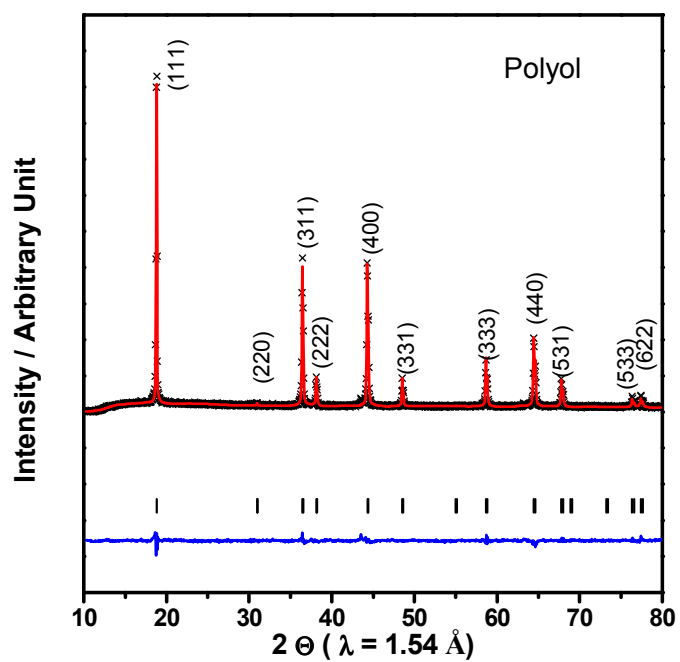
Figure 6.1. (a) & (b), SEM images of LiNi$_{0.5}$Mn$_{1.5}$O$_4$ via sol-gel and polyol methods. (c) & (d), Rietveld refinement results from XRD patterns. (e) Dependence of capacity retention with cycles at 25 & 55 °C. (f) Mn dissolution into the electrolyte with the cell ageing by ICP-OES analysis, continued.

(e)
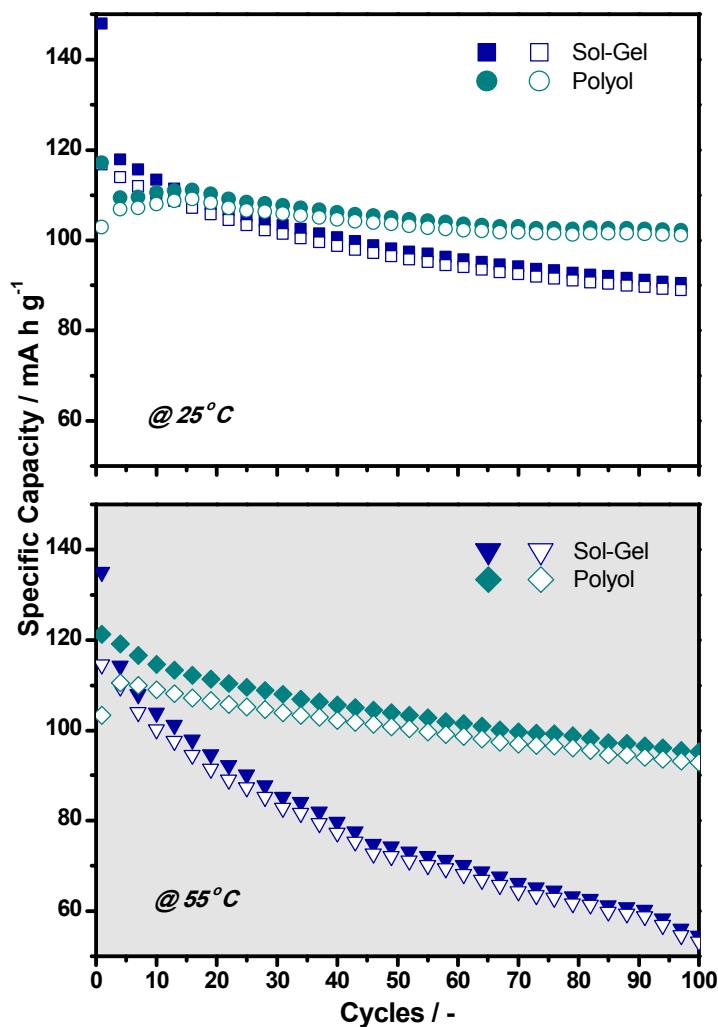
Figure 6.1. (a) & (b), SEM images of $LiNi_{0.5}Mn_{1.5}O_4$ via sol-gel and polyol methods. (c) & (d), Rietveld refinement results from XRD patterns. (e) Dependence of capacity retention with cycles at 25 & 55 °C. (f) Mn dissolution into the electrolyte with the cell ageing by ICP-OES analysis, continued.

(f)

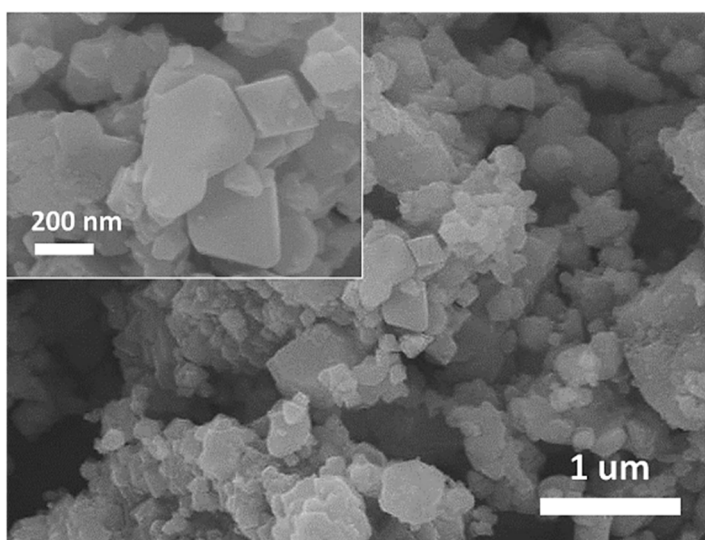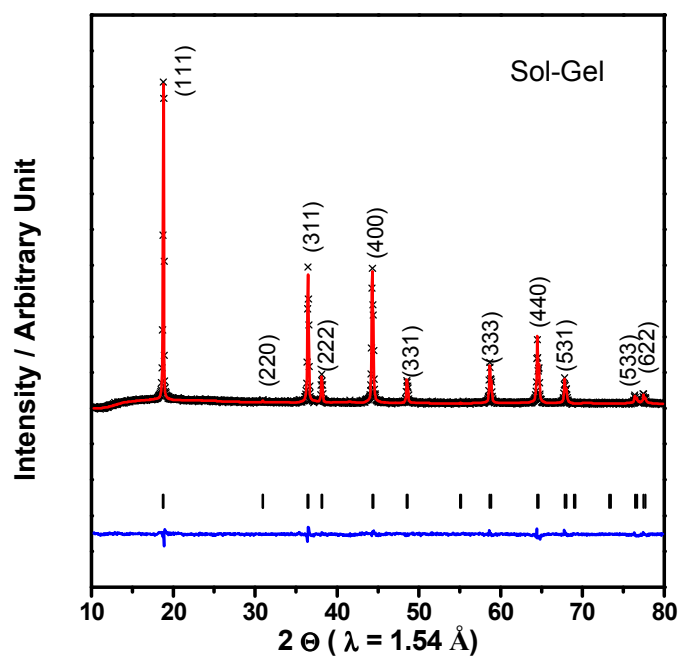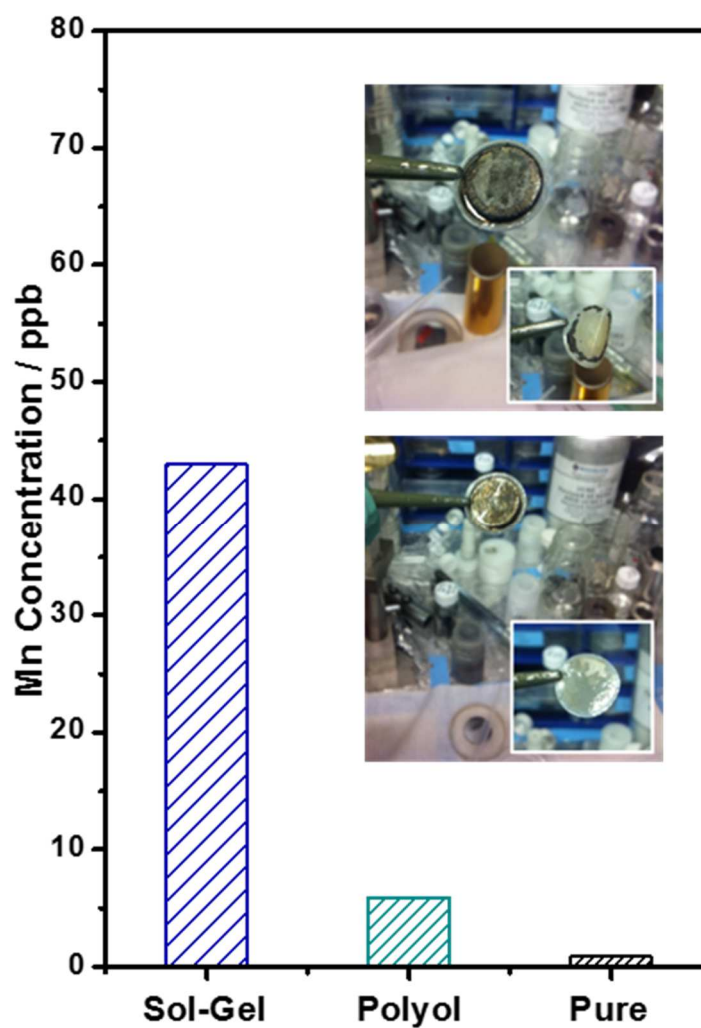Figure 6.1. (a) & (b), SEM images of LiNi$_{0.5}$Mn$_{1.5}$O$_4$ via sol-gel and polyol methods. (c) & (d), Rietveld refinement results from XRD patterns. (e) Dependence of capacity retention with cycles at 25 & 55 °C. (f) Mn dissolution into the electrolyte with the cell ageing by ICP-OES analysis, continued.

Typical morphologies of the materials from sol-gel and polyol synthesis are shown in the scanning electron micrograph (SEM) images of Figure 6.1(a) and (b), respectively. Both $LiNi_{0.5}Mn_{1.5}O_4$ materials had a similar particle size of approximately 200 nm in a range of 70 – 280 nm. To investigate the structural properties of the materials, the XRD patterns were collected and compared as shown in Figure 6.1(c) and (d). $LiNi_{0.5}Mn_{1.5}O_4$ spinel material is cubic close packed with lithium on the tetrahedral sites. The disordered structure with nickel and manganese disordering on the octahedral sites has the space group, F d -3 m. The Rietveld refinement patterns of the XRD obtained from both materials exhibit a good agreement with those reported in the literatures.[91] From the Rietveld refinements, it is noteworthy that the cation mixing of lithium and nickel for $LiNi_{0.5}Mn_{1.5}O_4$ prepared by sol-gel method is 1.39 %, which is lower than that for $LiNi_{0.5}Mn_{1.5}O_4$ via polyol, 2.48 %. The nickel and manganese molar ratio of the as-prepared $LiNi_{0.5}Mn_{1.5}O_4$ spinel materials were also confirmed by ICP-OES analysis. The molar ratio of nickel and manganese from both synthesis is in relatively good agreement with the theoretical ratio, Ni : Mn = 1 : 3. From these material characterizations, we cannot notice any significant discrepancy between those powders from two different synthesis. Interestingly, however, electrochemical properties of these two materials are somewhat different. Electrochemical charge and discharge voltage profiles between 3.50 and 4.85 V (vs. Li/Li^+) with applied current of C/10 rates show the typical electrochemical behavior of the $LiNi_{0.5}Mn_{1.5}O_4$ spinel material with around 4.7 V (vs. Li/Li^+) plateau related to the redox couple of $Ni^{2+/4+}$ and 4.0 V (vs. Li/Li^+) plateau to the redox couple of $Mn^{3+/4+}$. However, the discharging capacity of $LiNi_{0.5}Mn_{1.5}O_4$ via polyol, 113.0 mA h g^{-1}, is smaller than that of $LiNi_{0.5}Mn_{1.5}O_4$ prepared by sol-gel, 126.5 mA h g^{-1}. This discrepancy is ascribed to the

different cation mixing with lithium and nickel sites as mentioned in the XRD analysis. Figure 1(e) presents the relation between specific capacity and cycle number of $LiNi_{0.5}Mn_{1.5}O_4$ spinel materials at the rate of C/10. Initially, $LiNi_{0.5}Mn_{1.5}O_4$ prepared by sol-gel had larger capacity, but the capacity fading occurs with the following charge and discharge cycles. On the other hand, even though $LiNi_{0.5}Mn_{1.5}O_4$ via polyol had a relatively smaller capacity, but its capacity retention is much better than $LiNi_{0.5}Mn_{1.5}O_4$ prepared by sol-gel.

Many researchers reported previously that this $LiNi_{0.5}Mn_{1.5}O_4$ spinel materials is notorious for the Mn dissolution problem at the surface.[45, 65-66] It is insisted that Mn^{3+} ions at the surface undergo a disproportionation reaction, $2\ Mn^{3+} = Mn^{2+} + Mn^{4+}$, and the Mn^{2+} tends to dissolve into the electrolyte causing the degradation of the cell performance. In order to explore how much concentration of Mn in the electrolyte exists after the electrochemical charge and discharge cycles, ICP-OES analysis was carried out with the electrolyte, which was re-collected from the disassembled electrochemical cells in the Ar filled glove box, as shown in Figure 1(f). It proved that the Mn dissolution happens severely only in the case of $LiNi_{0.5}Mn_{1.5}O_4$ prepared by sol-gel.

In order to investigate the surface chemistry disparity, which we believed at the beginning that it might highly related to the dissolution problem, EELS analysis of valence state was carried out in reference to the spectra acquired from standard specimens with known cation valence states, as shown in Figure 6.2(a) and (b). Due to the intensity ratio of L3/L2 is sensitive to the valence state of the corresponding element, an experimental plot of these data serves as the reference for determining the valence state of the element in the materials.[107-108] The bulk region of both $LiNi_{0.5}Mn_{1.5}O_4$ materials exhibit the Mn

(a)
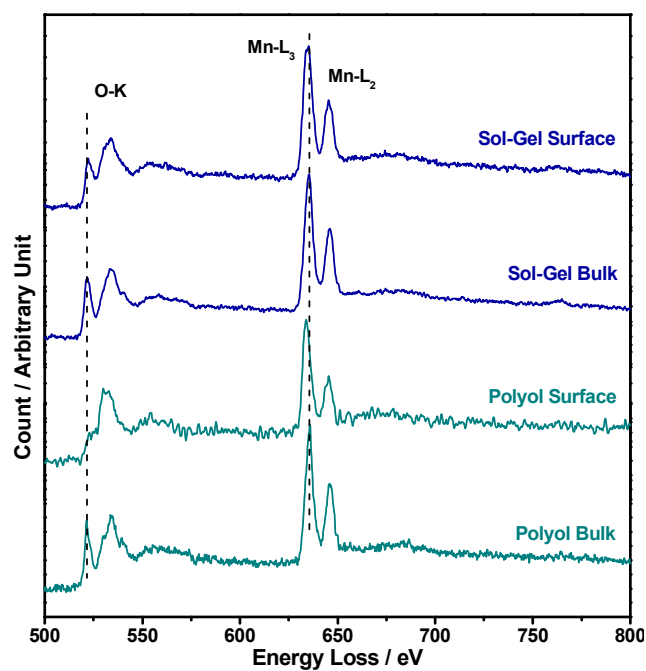
(b)
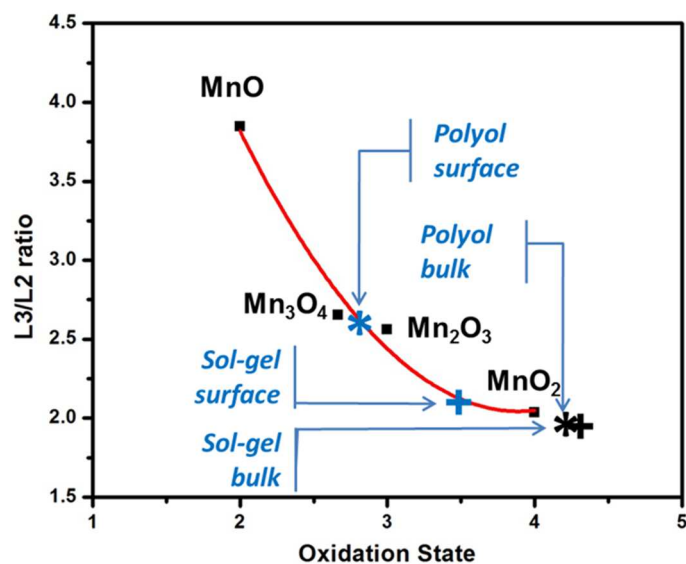
Figure 6.2. (a) EELS spectra of the O K- and Mn L-edge from the surface and bulk of LiNi$_{0.5}$Mn$_{1.5}$O$_4$ (b) Intensity ratios of L3/L2 calculated from the spectra. (c) XPS results for the Mn 2p and Mn 3p region scans from LiNi$_{0.5}$Mn$_{1.5}$O$_4$ powders via a sol-gel and polyol method

(c)
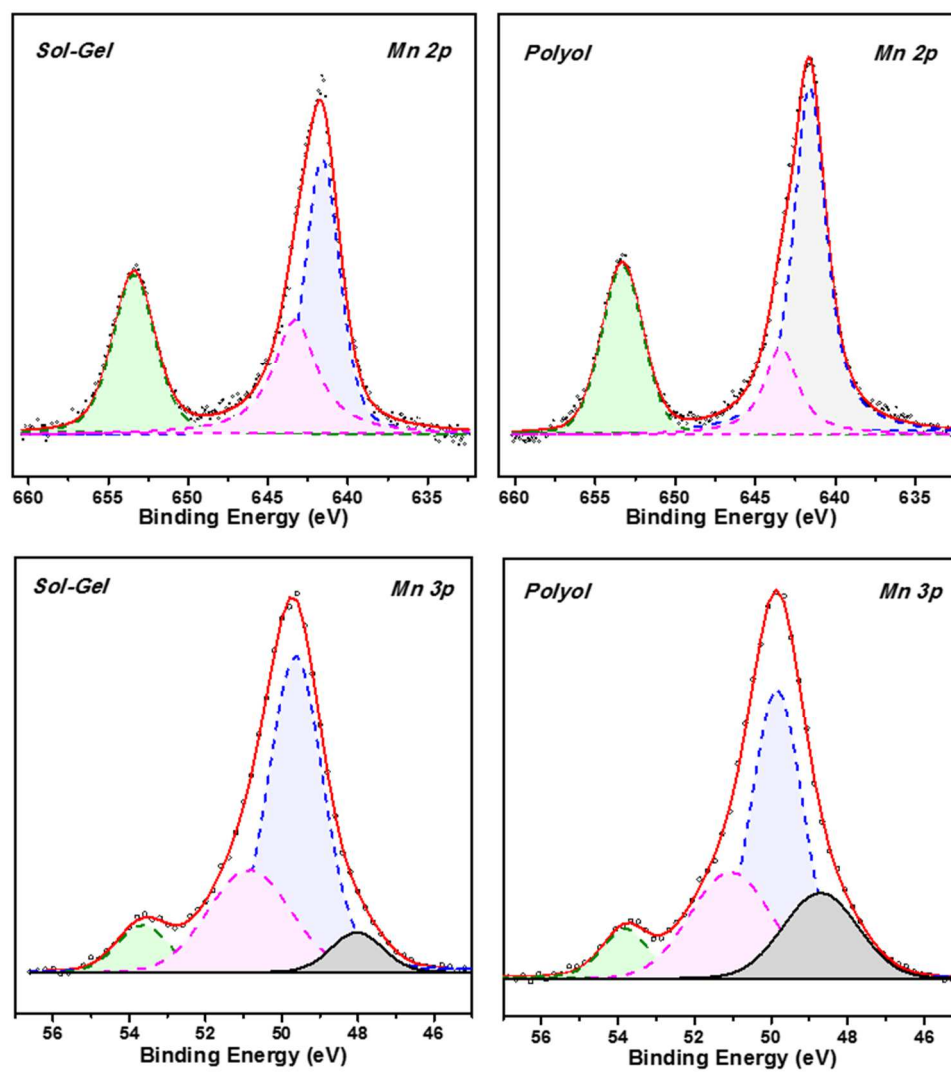
Figure 6.2. (a) EELS spectra of the O K- and Mn L-edge from the surface and bulk of LiNi$_{0.5}$Mn$_{1.5}$O$_4$ (b) Intensity ratios of L3/L2 calculated from the spectra. (c) XPS results for the Mn 2p and Mn 3p region scans from LiNi$_{0.5}$Mn$_{1.5}$O$_4$ powders via a sol-gel and polyol method, continued.

L3/L2 ratio corresponding to Mn^{4+}. On the other hand, the ratio of the surface region in $LiNi_{0.5}Mn_{1.5}O_4$ via polyol process increases more than that in $LiNi_{0.5}Mn_{1.5}O_4$ prepared by sol-gel. This indicates the valence state of the surface in $LiNi_{0.5}Mn_{1.5}O_4$ via polyol has lower valence states than that in $LiNi_{0.5}Mn_{1.5}O_4$ prepared by sol-gel. Figure 6.2(a) compares the EELS spectra of the O K-edge and the Mn L3 and L2 edges from the surface and bulk of both materials, respectively. The energy position and fine structures of Mn-L edges are identical on the spectra from the bulk region of both materials. However, those from the surface regions slightly shift to a lower energy loss, which represents a decreased valence state of manganese.[109] This is in an agreement of the Mn L3/L2 ratio result from Figure 6.2(b). It is also noticeable that fine-structure of O K-edge at the surface of the polyol powders changed. The first peak, at energy loss of ~532 eV almost disappeared on the spectrum from the surface of the polyol powders. This loss of O prepeak can be ascribed to the transition of 1 s core state to the unoccupied O-2p states hybridized with TM-3d states. Figure 6.2(c) shows the resulting x-ray photoelectron spectroscopy (XPS) spectra for the Mn2p and Mn3p region scans on two different synthetic methods (polyol vs. sol-gel). The Mn2p region scans both have a main peak at ~ 641.6 eV corresponding to Mn^{4+}. No noticeable change is observed in the Mn2p3/2 peak from pristine samples. To further explore the Mn oxidation state, the Mn3p region was investigated. Utilizing the Mn2p and Mn3p regions allow one to probe both the surface layer (Mn2p) as well as inner surface layer of the cathode material (Mn3p) by utilizing differences in the kinetic energy (Mn2p KE = 610 eV and Mn3p KE = 1204 eV) and escape depths.[105] The Mn3p region scans for the both pristine samples show a binding energy of ~ 49.8 eV, similar to Mn^{3+} in $\alpha-Mn_2O_3$ and $\beta-Mn_2O_3$. However, regarding XPS fitting/deconvolution of Mn2p scans, the peak area

at ~ 641.0 eV, due to Mn^{2+} in MnO, shows significant difference. Peak area (=peak intensity) is considered as the amount of a material is at the surface. Therefore, Mn2p scans suggest that the outer surfaces of both materials, have different oxidation state (chemistry) which is resulted from the Mn presenting in the outer layer and oxidized to more Mn^{2+}. This result is consistent with the presented EELS spectra in this work showing different valence state of Mn on the surface and bulk. The results from the XPS analysis, performed on surface and bulk region of both $LiNi_{0.5}Mn_{1.5}O_4$ materials, suggesting that Mn^{2+} is predominant only on the surface of $LiNi_{0.5}Mn_{1.5}O_4$ via polyol. It was found by Karim et al. that the final low-energy structure of the prevalent (111) surface in LMO crystallites can be attributed to charge and coordination.[110] For example, lower charged surface cations (in this case Mn^{2+}) will usually result in more stable surface facets. The EELS spectrum, which shows the decreased intensity of the O-K edge peak, also supports the Mn cation is being reduced to the lower oxidation state on the polyol surface. In addition, the oxygen loss at the polyol-synthesized surface, as shown in EELS spectrum of the O-K edge, can attribute to the undercoordinated geometries on the surface. It also causes different surface termination by undergoing significant reconstruction to minimize the total surface energy.

To study in-depth local structural variations at the surface and bulk around Mn during cycled-aging, in situ extended X-ray absorption fine structure (EXAFS) spectra for both charged/discharged materials were analyzed using transmission electron yield (TEY) and fluorescence yield (FY) modes. The absorption is measured using emitted electrons in TEY mode. TEY measurements can only probe the surface of a material (~3 nm) due to the shorter mean free path of electrons,[111-112] similar to that of the Mn3p XPS. The Fourier-transformed (FT) EXAFS spectra from both TEY and FY mode (k^3-weighted in k-space

(a)
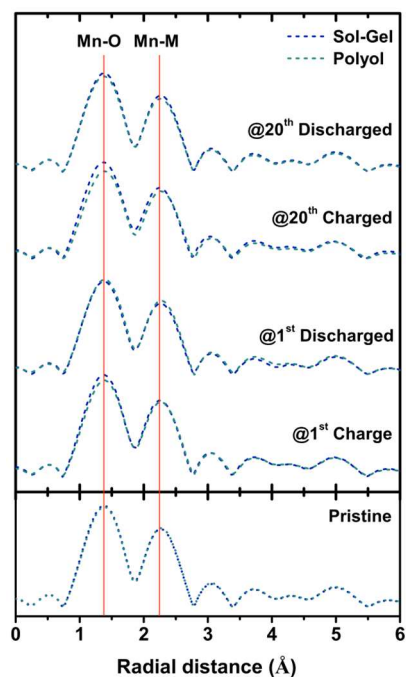
(b)
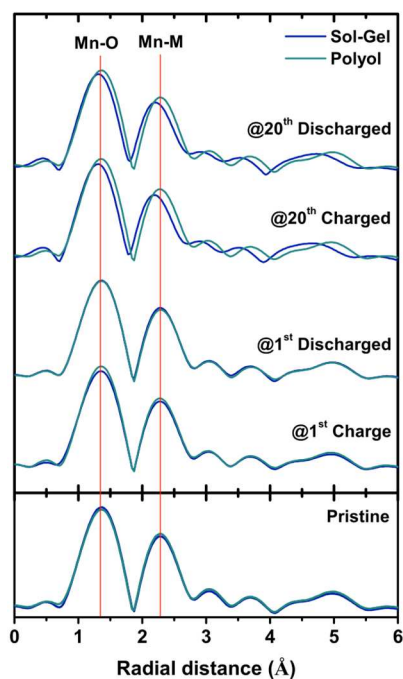
Figure 6.3. Fourier-transformed magnitude of Mn K-edge EXAFS spectra for fully charged/discharged at the 1st cycle and after 20th cycles with the pristine LiNi$_{0.5}$Mn$_{1.5}$O$_4$ spinel (bottom). (a) Fluorescence yield (FY) and (b) Total electron yield (TEY) modes

but not phase-corrected FT, causing shorter bond lengths in the plots than for the actual ones) at Mn K-edge are shown, respectively, in Figure 6.3(a) and (b). The FT magnitudes of pristine $LiNi_{0.5}Mn_{1.5}O_4$ materials via sol-gel and polyol are also plotted in the bottom panels as references. The first peak at approximately 1.3 Å in Figure 6.3 is assigned to the single scattering path from Mn to the closest oxygen atoms (i.e., the Mn-O bond). The second peak at about 2.25 Å is assigned to Mn to the nearest TM atoms (Ni and Mn) occupying the octahedral sites. The third peak at about 3.1 Å is assigned to Mn to the second nearest TM occupying the tetrahedral sites (TM_{tet}). For the Mn K-edge results shown in FY mode, there were negligible alterations in both the Mn-O and Mn-TM bond length from the pristine to 20th cycled state, indicating that Mn in both materials is stable and maintains its original structure within the bulk site. On the other hand, the spectral changes during cycled-aging in TEY mode, the shift of the Mn-TM bond length and the emergence of the Mn-TM_{tet} can be observed only on the $LiNi_{0.5}Mn_{1.5}O_4$ prepared by sol-gel. It is pointing to the formation of the Mn_3O_4 phase and the migration of Mn cations (mostly Mn^{2+}) to the surface which is well-known phase transition phenomenon in $LiNi_{0.5}Mn_{1.5}O_4$ spinel materials. The TM migration happened upon during the cycling then formed irreversible Mn_3O_4 or rocksalt-like phase transition onto the surface. However, surprisingly, $LiNi_{0.5}Mn_{1.5}O_4$ via polyol process does show structural and phase stability by looking at the spectra on both at the bulk and surface even after 20th cycled. It is worthwhile to mention that the establishing stable surface structure through polyol process is the key to prevent Mn ion dissolution and help long-term cycleability.

The local atomic-level crystal structures were further investigated via STEM. Multiple particles were selected for study and the results are consistent, therefore only

(a)

(b)
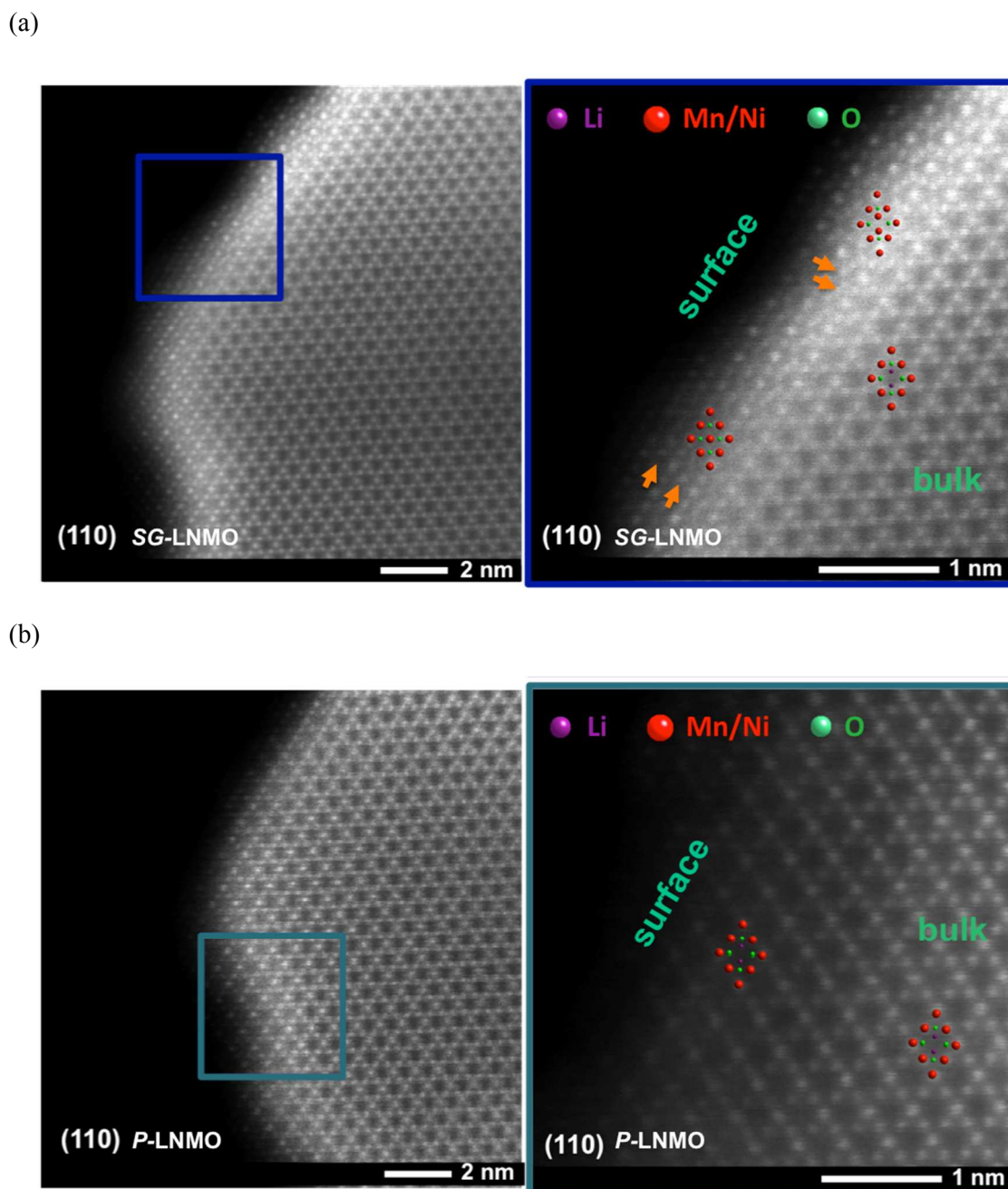
Figure 6.4. (a) HR-STEM images of the bulk and surface of 20th cycled $LiNi_{0.5}Mn_{1.5}O_4$ at low magnification and (b) high magnification taken along the [110] zone axis. The schematic crystal structures represent the Li ions (purple), transition metal ions (red) and oxygen (green)

representative data are shown in Figure 6.4. STEM images from the cycled $LiNi_{0.5}Mn_{1.5}O_4$ spinel materials (at the discharge state after 20 cycles between 3 to 4.85 V) were taken along the [110] crystallographic direction. In this direction, the position of TM heavy atomic columns can be clearly identified from a diamond configuration of contrast. The STEM images at the bulk regions of $LiNi_{0.5}Mn_{1.5}O_4$ prepared by sol-gel method showed the structure to be spinel. However, two types of local atomic-level structures different from spinel are clearly observed at the surface regions of $LiNi_{0.5}Mn_{1.5}O_4$ prepared by sol-gel (Figure 6.4(a)). Close examination of the surface regions in high magnification (Figure 6.4(b)) clearly reveals the presence of bright contrast in the tetrahedral Li sites and empty octahedral sites, the center of the diamond configuration. This contrast cannot be caused by light elements such as Li or O due to their small atomic number Z. It can only be attributed to the migration of heavy TM ions during electrochemical cycling. On the contrary, $LiNi_{0.5}Mn_{1.5}O_4$ via polyol showed only spinel structure at both the bulk and surface regions. All of them consistently demonstrate the migration of TM ions only in $LiNi_{0.5}Mn_{1.5}O_4$ prepared by sol-gel and stable spinel structure in $LiNi_{0.5}Mn_{1.5}O_4$ via polyol process, persistent with TEY and FY XAS spectra.

6.4. Conclusion

On the basis of the combined results of in situ XAS and STEM in this paper, it was found that the atomic structural transformation at the surface of the active materials is the main source of the Mn dissolution problem on the conventional spinel $LiNi_{0.5}Mn_{1.5}O_4$ materials, especially, one synthesized via sol-gel method. TM ion migration involving different phase formation at the surface plays a bridging role in accelerating Mn dissolution

during electrochemical cycling. Herein, our group developed new pathway to synthesis $LiNi_{0.5}Mn_{1.5}O_4$ spinel materials from polyol process. This material does not encounter the atomic structure transformation at the surface and an ensuing critical dissolution problem without any surface modification or post-treatment. This newly reported good electrochemical performance related to the stable surface structure will help to solve the capacity fading issues on this materials.

Chapter 6, in full, is currently being prepared for submission for publication of the material "Implementation of stable surface structures; a promising key to solve capacity fading issues for the high-voltage $LiNi_{0.5}Mn_{1.5}O_4$" Hyojung Yoon, Hyung-Man Cho, Danna Qian, Ying Shirley Meng. The dissertation author was the co-primary investigator and author of this paper. All the experiment parts were performed by the author except EELS and STEM study.

Chapter 7. Effect of Coating Materials on CuF₂ Cathode for Lithium-Ion Battery Using Pair Distribution Function (PDF) Analysis

In order to fulfill the demanding requirements for advanced battery applications, such as electric vehicles, the increase of energy density is one of the inevitable conditions. Inadequate energy density of the current intercalation materials can be overcome by using conversion materials, since all the possible oxidation states of the compound can be utilized during the its redox reaction. In this chapter, CuF_2 and NiO-coated CuF_2 are investigated to understand the mechanism and NiO coating effect with the help of pair distribution function analysis.

7.1. Introduction

Among all the known conversion materials, CuF_2 is of particular interest due to its high specific capacity (528 mA h g^{-1}) and voltage (3.55 V vs. Li/Li$^+$). The large band gap offers high operating voltages, but low electronic conductivity and poor rate performance. The large voltage hysteresis during the charge/discharge limits the overall energy efficiency. In particular, it has never been shown the reversible conversion reaction.

A study by Badway et al. on iron fluoride demonstrated enhanced electrochemical properties by fabricating the formation of carbon metal fluoride nanocomposites.[36] When this research was applied to copper, it showed an increase in theoretical capacity to 50%, however when the carbon was replaced with mixed conductors such as MoO_3, the capacity increased up to 85 %. Wang et al. suggested that origin of poor reversibility in CuF_2

conversion process was explained by the segregation of large Cu particles (5-12 nm).[21] It does not provide any pathway for local electron transport through the insulating LiF phase.

We have developed a NiO coating for the CuF_2 conversion materials, which is the first demonstration of a rechargeable CuF_2 cathode. We believe that the coating layer provides enhanced ionic/electronic conductivity as well as it confines Cu, LiF, and CuF_2 particles to facilitate the formation of a conductive nano-scale metallic network. It also reduces electrolyte decomposition and prevents copper dissolution into the electrolyte. In order to investigate the differences in the conversion reactions quantitatively, we analyzed the phases and Cu nanoparticle size at the 1st and 2nd discharged states using pair distribution function analysis.

7.2. Experimental

Commercially available CuF_2 (Alfa Aesar) powder was used for this study. NiO coated CuF_2 (NiO-CuF_2) was prepared by ball milling process of CuF_2 with acetylene black (Strem chemicals). Stoichiometric mixtures (CuF_2 : NiO = 85 : 15 wt. %) were placed inside a planetary ball mill (PM 100, Retsch) and the milling was performed for 6 h at 500 rpm under Ar atmosphere. As-prepared NiO-CuF2 and pure CuF2 were again ball-milled under the milling condition in order to get the carbon composites (NiO-CuF_2 (or CuF_2) : C = 80 : 20 wt. %)

Electrochemical discharging and charging process were performed using coin-type (2016) cells. The working electrodes were composed of NiO-CuF_2/C (or CuF_2/C), acetylene black and PVDF at a weight ratio of 70:20:10. Pure lithium metal was used as a counter electrode and polypropylene C480 (Celgard) was used as a separator. The coin

cells were assembled with the electrolyte consisting of 1 M LiPF$_6$ dissolved in ethylene carbonate (EC) and dimethylene carbonate (DMC) with a volume ratio of 1:1 (Novolyte) in an MBraun Ar-filled glovebox (H$_2$O < 0.1 ppm). Electrochemical cycling was performed using a battery cycler (Arbin) at room temperature, with a constant current density of C/35, and a cell potential range of 2.0 ~4.0 V (vs. Li/Li$^+$). For the linear potential sweep voltammogram, Cu and Ni foils were employed for the working electrodes. Other conditions were same as previous experiments. Scan rate was 1 mV s^{-1}.

High-energy total X-ray scattering data (λ = 0.2114 Å) were collected at the dedicated PDF beamline 11-ID-B at the Advanced Photon Source, Argonne National Laboratory. The raw images were integrated using the software FIT2d.[113] PDFgetX2[114] was used to correct the data for background contributions, Compton scattering and detector effects. PDFgetX2 was also employed to do Fourier transform the data to generate G(r), the PDF. Structure models were refined against the PDF data within PDFgui. The electrode samples were recovered at different states of charge by disassembling the coin cells inside the glovebox. The electrodes were washed with battery-grade DMC (Novolyte, packed and sealed in Kapton under Ar atmosphere.

7.3. Results and Discussion

Figure 7.1 shows the electrochemical voltage profiles of CuF$_2$/C and NiO-CuF$_2$ electrodes in the voltage window between 2.0 and 4.0 V (vs. Li/Li$^+$) at C/35 rate. The CuF$_2$/C electrode delivered 300 mA h g^{-1} at the 1st discharge, which is only 57 % of the theoretical specific capacity as shown in Figure 7.1(a). The plateau of conversion reaction was lower than 2.8 V (vs. Li/Li$^+$), which shows a huge difference from the theoretical redox

(a)
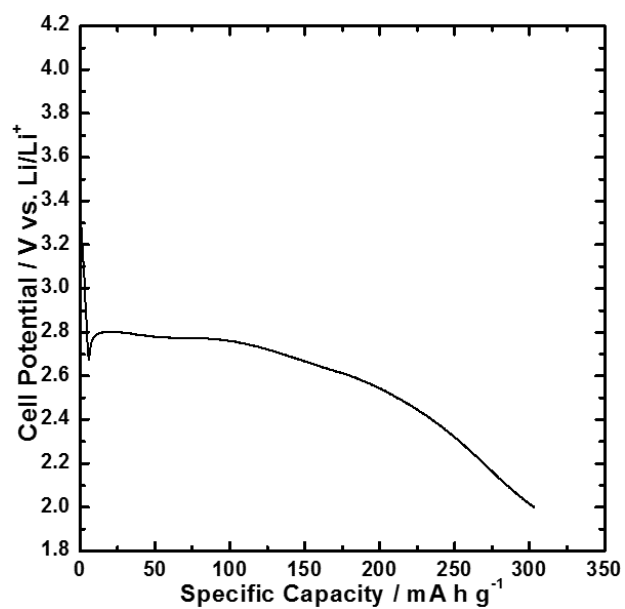
(b)
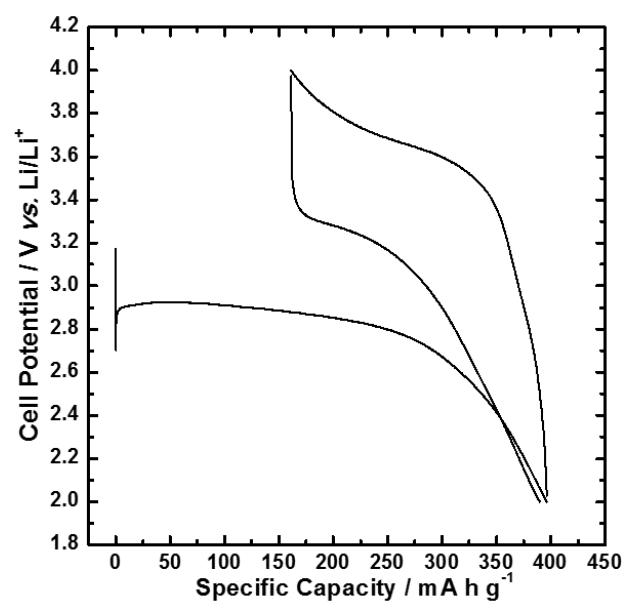
Figure 7.1. Electrochemical voltage profiles of (a) CuF$_2$ discharging and (b) NiO-CuF$_2$ discharging and charging

voltage of 3.55 V (vs. Li/Li$^+$). This poor electrochemical performance is mainly because of the large band gap and consequent poor electrical conductivity. Moreover, this CuF$_2$/C electrode did not show a reversible charging process, which was an agreement of the reported results. On the other hand, NiO coated CuF$_2$ electrode exhibits considerable improvement in the electrochemical performance in Figure 7.1(b). The 1st discharging capacity is 400 mA h g^{-1} (about 75 % of the theoretical capacity), and the discharging plateau shows over 2.9 V (vs. Li/Li$^+$), indicating that the overpotential was diminished. The large overpotential contains a significant component of polarization related to slow reaction kinetics particularly upon the lithiation (discharge) process. The remarkable improvement on this NiO-CuF$_2$ electrode is its reversibility; It shows the rechargeable reaction with the capacity of > 250 mA h g^{-1}. This is the first report of the reversible conversion reaction in CuF$_2$ materials.

After discharging CuF$_2$ material, nano-sized Cu metal particle and LiF phase can be formed. Due to limited particle size of nanomaterials, a conventional crystallographic approach using Bragg scattering cannot disclose full information of their structure.[115-116] In this work, pair distribution function analysis of X-ray total scattering data was employed in order to investigate the phase transformation in an atomic scale of CuF$_2$/C and NiO-CuF$_2$/C conversion reactions.

The experimental pairs distribution function profiles and their refinement results for 1st discharged CuF$_2$/C, and 1st discharged, 1st charged, and 2nd discharged NiO-CuF$_2$/C are shown in Figure 7.2(a), (b), (c), and (d), respectively. The phase mole fractions and the evolution of the particle sizes were evaluated from the refinement of structural models against the corresponding pair distribution functions, where a bimodal distribution of small

(a)
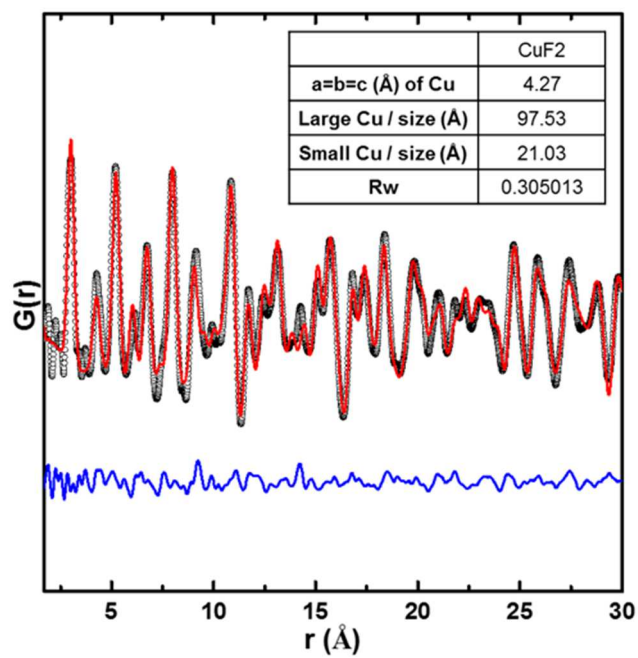
(b)
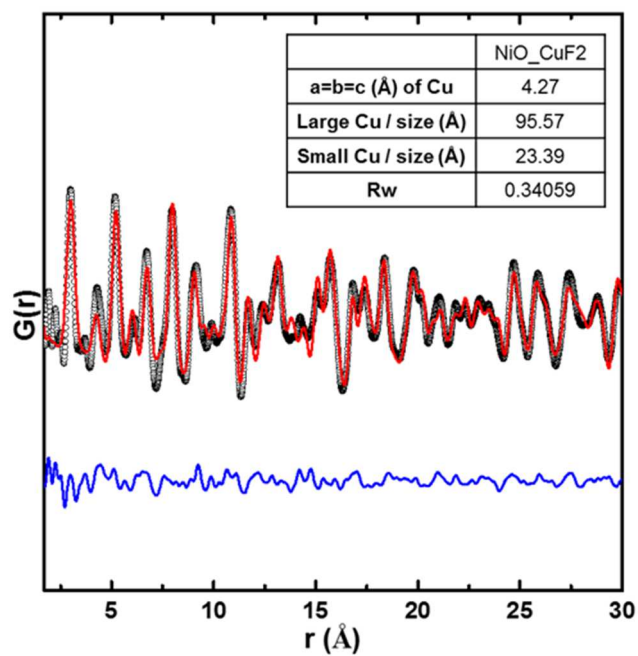
Figure 7.2. Pair distribution function (PDF) profiles of (a) discharged CuF_2, (b) 1st discharged NiO-CuF_2, (c) 1st charged NiO-CuF_2, and (d) 2nd discharged NiO-CuF_2

(c)
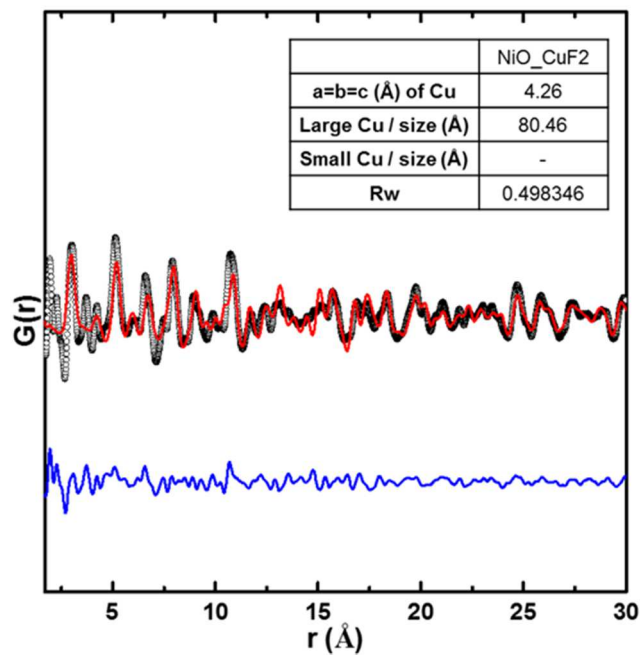
(d)
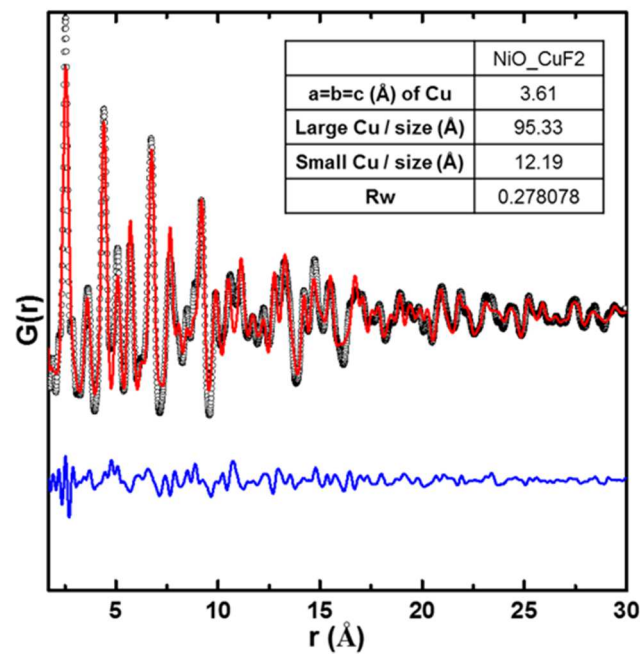
Figure 7.2. Pair distribution function (PDF) profiles of (a) discharged CuF$_2$, (b) 1st discharged NiO-CuF$_2$, (c) 1st charged NiO-CuF$_2$, and (d) 2nd discharged NiO-CuF$_2$, continued.

and large Cu particles was used to describe a non-uniform particle size for the Cu metal phase (Figure 7.3). The results show that after the 1st discharged both CuF_2/C and NiO-CuF_2/C materials consist of Cu nanoparticles with similar sizes of ca. 20 Å (= 2 nm) and ca. 95 Å (= 9.5 nm). Interestingly, in the 1st charged NiO-CuF2/C electrode, Cu metal phase of small particle size disappeared, and it was reformed with smaller particle size, ca. 10 Å (= 1 nm), in the 2nd discharged state. It can be assumed that the Cu metal phase of small particle size involves the conversion reaction. This is different from the recent report by Hua et al., which insists that small-sized Cu metal does not change during the following charging process.[117] In addition, phase distribution of large-sized Cu metal does not change, but its size reduces from ca. 95 Å to ca. 80 Å during the discharging and charging process. This represents Cu metal involves a conversion reaction. On the other hand, NiO phase does not involve the reaction, however from the electrochemical data in Figure 7.1(b), a reversible capacity is about 30 % during the charging process, and phase transformation of CuF_2 is only about 20 %. Therefore, it is noteworthy that there is still a Cu dissolution problem. In order to confirm the Cu metal dissolution potential, linear potential sweep voltammogram for Cu and Ni foils was conducted in Figure 7.4. From this result, it is clear that the CuF_2 conversion reaction potential is closed to the Cu dissolution potential.

7.4. Conclusion

The rechargeable conversion reaction of NiO-CuF_2/C electrode have been studied and compared with normal CuF_2/C electrode using pair distribution function analysis. The results indicated that a bimodal size distribution (ca. 20 Å and ca. 95 Å) of Cu nanoparticles was found in both CuF_2/C and NiO-CuF_2/C electrodes after 1st discharging. Only small

nanoparticle of ca. 20 Å, however, involved the rechargeable conversion reaction. Taking observation and analysis into account, we deduce that NiO phase can minimize the Cu ions dissolved in the electrolyte and increase the chance of reversible reaction to CuF_2. There is discrepancy on reversible capacity and the amount of phase transformation, which indicate that Cu dissolution still exists. A further surface modification, such as polymer coating, can be an appropriate solution to avoid Cu dissolution and enhance the performance of CuF_2 materials.

Chapter 7, in part, is currently being prepared for submission for publication of the material "Comprehensive insights into the conversion reaction voltage and reversibility of CuF_2 electrode in Li-ion battery". Joon Kyo Seo, Hyung-Man Cho, Mahsa Sina, Katsunori Takahara, Ying Shirley Meng. The dissertation author was the co-investigator and co-author of this material.
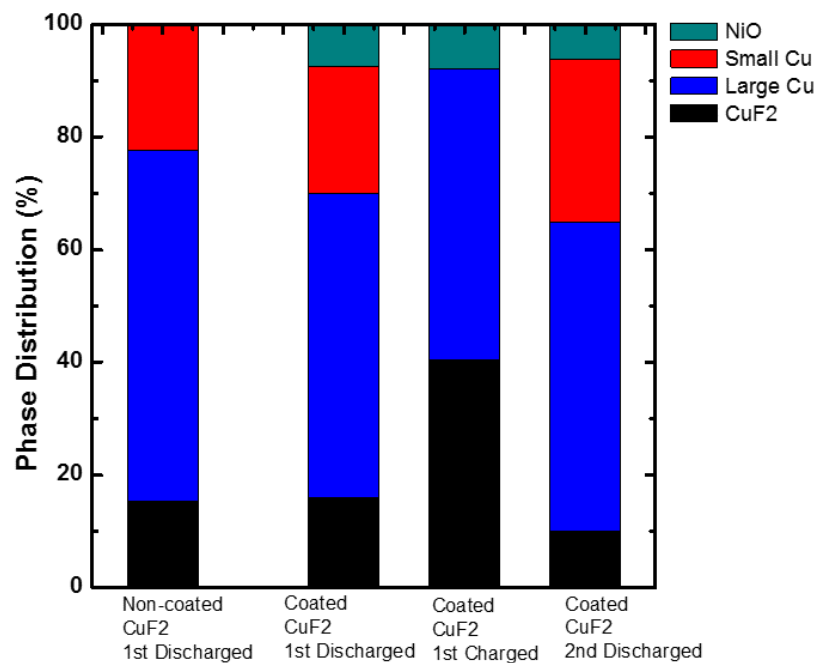
Figure 7.3. Phase distribution by full profile fits to the PDF data
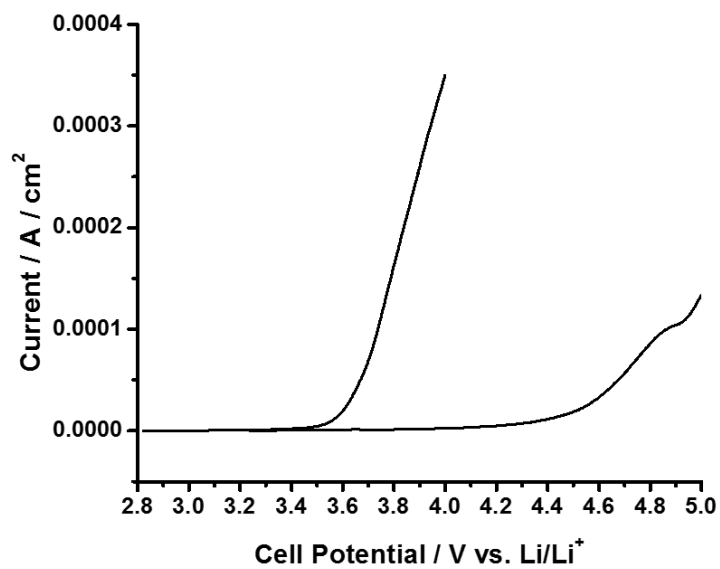
Figure 7.4. Linear potential sweep voltammogram for Cu and Ni foils

Chapter 8. Summary and Future Work

8.1. Summary

In this study, high-voltage spinel material, $LiNi_{0.5}Mn_{1.5}O_4$, for positive electrode in lithium-ion batteries, have been prepared in nanowire electrode to maximize the power density of lithium-ion batteries, and its nano-size effects on battery performance have been investigated with the help of X-ray diffraction, X-ray absorption spectroscopy, transmission electron microscopy, inductively coupled plasma optical emission spectrometry, and electrochemical impedance spectroscopy. Nanowire electrode can improve an instant discharging power density of $LiNi_{0.5}Mn_{1.5}O_4$ spinel material with a reduced charge-transfer and diffusion resistances. Since an increase in surface area of nanowires results in detrimental interfacial side reactions, however, overall electrochemical performance was degraded, such as, poor cycleability and capacity fading. Al_2O_3 ALD coating at the surface of the nanowire can provide the protective layer and overcome the unwanted reaction. On the basis of the combined results of *in situ* XAS and STEM studies, it was found that the atomic structural transformation on the surface of active materials is the main source of the Mn dissolution problem on the conventional spinel $LiNi_{0.5}Mn_{1.5}O_4$ materials. This study verified that the drawback of the nano-structured electrode could be resolved with the help of the surface modification, as well as a new synthesis method, polyol process.

The inadequate energy density of current intercalation materials can be overcome by using conversion materials, because all the possible oxidation states of compound can be utilized during its redox reaction. Among the various conversion materials, CuF_2 have

been attracting an interest since it can provide higher operating voltage, 3.55 V (vs. Li/Li$^+$). This CuF$_2$ electrode, however, cannot give the rechargeable behavior, thus its practical use was inhibited. In this study, first rechargeable performance was reported with NiO coated CuF$_2$ and its rechargeable reaction mechanism have been studied by using pair distribution function analysis. A bimodal size distribution (ca. 20 Å and ca. 95 Å) of Cu nanoparticles was found in NiO-CuF$_2$/C electrode after 1st discharging and only a small particle size of Cu metal involves the charging/discharging process. It is suggested that NiO phase can minimize Cu ions dissolved into the electrolyte and increase the chance of reversible reaction to CuF$_2$.

8.2. Future Work

It is proved that nano-size in lithium-ion battery electrode affects kinetic properties of LiNi$_{0.5}$Mn$_{1.5}$O$_4$ spinel materials. The roles of nano-size in the electrodes have been emphasized in conventional lithium-ion batteries, however these conventional electrodes based on intercalation reaction have a limit in respect to increasing the battery energy density. Its maximum energy density is not adequate to meet the requirements of advanced applications such as electric vehicles. Development of new electrochemical systems with higher energy density are desired, and next-generation batteries, for instance, lithium-air and lithium-sulfur batteries, are considered promising alternatives. It is believed that nanostructured electrodes will be highly useful improving lithium-air and lithium-sulfur batteries. Nanostructured metal oxides were utilized as catalysts in lithium-air batteries.[118-119] Ordered mesoporous carbon was employed as an effective sulfur reservoir for lithium-sulfur batteries.[120-121] However, there is still a lack of extensive investigation in

nanostructure effects on lithium-air and lithium-sulfur batteries.

CuF_2 materials, which show the conversion reaction, were studied in order to satisfy the demanding energy density of advanced applications. Even though this study presents the positive results in terms of the rechargeability, it still needs to resolve the Cu dissolution problem for practical use. A further surface modification, such as polymer coating can be an appropriate solution to avoid the Cu dissolution. On the other hand, compositional and/or structural modification at atomic scale such as doping and substitution can avoid dissolution with the redox potential change.

References

1.   Service, R. F., Getting There. *Science* **2011,** *332* (6037), 1494-1496.

2.   Rolison, D. R.; Nazar, L. F., Electrochemical energy storage to power the 21st century. *MRS Bull.* **2011,** *36* (07), 486-493.

3.   Xu, B.; Qian, D.; Wang, Z.; Meng, Y. S., Recent progress in cathode materials research for advanced lithium ion batteries. *Mater. Sci. Eng.: R: Rep.* **2012,** *73* (5–6), 51-65.

4.   Kim, J. H.; Myung, S. T.; Yoon, C. S.; Kang, S. G.; Sun, Y. K., Comparative Study of LiNi0.5Mn1.5O4-δ and LiNi0.5Mn1.5O4 Cathodes Having Two Crystallographic Structures: Fd3̄m and P4332. *Chem. Mat.* **2004,** *16* (5), 906-914.

5.   Kim, J.-H.; Yoon, C. S.; Myung, S.-T.; Prakash, J.; Sun, Y.-K., Phase Transitions in Li1 − δ Ni0.5Mn1.5 O 4 during Cycling at 5 V. *Electrochem. Solid-State Lett.* **2004,** *7* (7), A216-A220.

6.   Amdouni, N.; Zaghib, K.; Gendron, F.; Mauger, A.; Julien, C., Structure and insertion properties of disordered and ordered LiNi0.5Mn1.5O4 spinels prepared by wet chemistry. *Ionics* **2006,** *12* (2), 117-126.

7.   Ariyoshi, K.; Iwakoshi, Y.; Nakayama, N.; Ohzuku, T., Topotactic Two-Phase Reactions of Li[Ni1/2Mn3/2]O4 (P 43 3 2) in Nonaqueous Lithium Cells. *J. Electrochem. Soc.* **2004,** *151* (2), A296-A303.

8.   Lee, E.-S.; Nam, K.-W.; Hu, E.; Manthiram, A., Influence of Cation Ordering and Lattice Distortion on the Charge–Discharge Behavior of LiMn1.5Ni0.5O4 Spinel between 5.0 and 2.0 V. *Chem. Mat.* **2012,** *24* (18), 3610-3620.

9.   Zhong, Q.; Bonakdarpour, A.; Zhang, M.; Gao, Y.; Dahn, J. R., Synthesis and Electrochemistry of LiNi[sub x]Mn[sub 2 - x]O[sub 4]. *J. Electrochem. Soc.* **1997,** *144* (1), 205-213.

10.   Yang, M.-C.; Xu, B.; Cheng, J.-H.; Pan, C.-J.; Hwang, B.-J.; Meng, Y. S., Electronic, Structural, and Electrochemical Properties of LiNixCuyMn2–x–yO4 (0 < x < 0.5, 0 < y < 0.5) High-Voltage Spinel Materials. *Chem. Mat.* **2011,** *23* (11), 2832-2841.

11.   Cabana, J.; Zheng, H. H.; Shukla, A. K.; Kim, C.; Battaglia, V. S.; Kunduraci, M., Comparison of the Performance of LiNi1/2Mn3/2O4 with Different Microstructures. *J. Electrochem. Soc.* **2011,** *158* (9), A997-A1004.

12.   Cabana, J.; Casas-Cabanas, M.; Omenya, F. O.; Chernova, N. A.; Zeng, D.; Whittingham, M. S.; Grey, C. P., Composition-Structure Relationships in the Li-Ion Battery Electrode Material LiNi0.5Mn1.5O4. *Chem. Mat.* **2012,** *24* (15), 2952-2964.

13.   Xiao, J.; Chen, X.; Sushko, P. V.; Sushko, M. L.; Kovarik, L.; Feng, J.; Deng, Z.; Zheng, J.; Graff, G. L.; Nie, Z.; Choi, D.; Liu, J.; Zhang, J.-G.; Whittingham, M. S., High-

Performance LiNi0.5Mn1.5O4 Spinel Controlled by Mn3+ Concentration and Site Disorder. *Adv. Mater.* **2012,** *24* (16), 2109-2116.

14.   Chen, Z.; Qiu, S.; Cao, Y.; Ai, X.; Xie, K.; Hong, X.; Yang, H., Surface-oriented and nanoflake-stacked LiNi0.5Mn1.5O4 spinel for high-rate and long-cycle-life lithium ion batteries. *J. Mater. Chem.* **2012,** *22* (34), 17768-17772.

15.   Chemelewski, K. R.; Lee, E.-S.; Li, W.; Manthiram, A., Factors Influencing the Electrochemical Properties of High-Voltage Spinel Cathodes: Relative Impact of Morphology and Cation Ordering. *Chem. Mat.* **2013,** *25* (14), 2890-2897.

16.   Chemelewski, K. R.; Shin, D. W.; Li, W.; Manthiram, A., Octahedral and truncated high-voltage spinel cathodes: the role of morphology and surface planes in electrochemical properties. *J. Mater. Chem. A* **2013,** *1* (10), 3347-3354.

17.   Hai, B.; Shukla, A. K.; Duncan, H.; Chen, G., The effect of particle surface facets on the kinetic properties of LiMn1.5Ni0.5O4 cathode materials. *J. Mater. Chem. A* **2013,** *1* (3), 759-769.

18.   Shin, D. W.; Bridges, C. A.; Huq, A.; Paranthaman, M. P.; Manthiram, A., Role of Cation Ordering and Surface Segregation in High-Voltage Spinel LiMn1.5Ni0.5–xMxO4 (M = Cr, Fe, and Ga) Cathodes for Lithium-Ion Batteries. *Chem. Mat.* **2012,** *24* (19), 3720-3731.

19.   Cabana, J.; Monconduit, L.; Larcher, D.; Palacín, M. R., Beyond Intercalation-Based Li-Ion Batteries: The State of the Art and Challenges of Electrode Materials Reacting Through Conversion Reactions. *Adv. Mater.* **2010,** *22* (35), E170-E192.

20.   Badway, F.; Mansour, A. N.; Pereira, N.; Al-Sharab, J. F.; Cosandey, F.; Plitz, I.; Amatucci, G. G., Structure and Electrochemistry of Copper Fluoride Nanocomposites Utilizing Mixed Conducting Matrices. *Chem. Mat.* **2007,** *19* (17), 4129-4141.

21.   Wang, F.; Robert, R.; Chernova, N. A.; Pereira, N.; Omenya, F.; Badway, F.; Hua, X.; Ruotolo, M.; Zhang, R.; Wu, L.; Volkov, V.; Su, D.; Key, B.; Whittingham, M. S.; Grey, C. P.; Amatucci, G. G.; Zhu, Y.; Graetz, J., Conversion Reaction Mechanisms in Lithium Ion Batteries: Study of the Binary Metal Fluoride Electrodes. *J. Am. Chem. Soc.* **2011,** *133* (46), 18828-18836.

22.   Cho, H.-M.; Choi, W.-S.; Go, J.-Y.; Bae, S.-E.; Shin, H.-C., A study on time-dependent low temperature power performance of a lithium-ion battery. *J. Power Sources* **2012,** *198* (0), 273-280.

23.   Singer, A.; Ulvestad, A.; Cho, H.-M.; Kim, J. W.; Maser, J.; Harder, R.; Meng, Y. S.; Shpyrko, O. G., Nonequilibrium Structural Dynamics of Nanoparticles in LiNi1/2Mn3/2O4 Cathode under Operando Conditions. *Nano Lett.* **2014,** *14* (9), 5295-5300.

24.   Bruce, P. G.; Scrosati, B.; Tarascon, J.-M., Nanomaterials for Rechargeable Lithium Batteries. *Angew. Chem. Int. Ed.* **2008,** *47* (16), 2930-2946.

25. Jiang, J.; Li, Y.; Liu, J.; Huang, X.; Yuan, C.; Lou, X. W., Recent Advances in Metal Oxide-based Electrode Architecture Design for Electrochemical Energy Storage. *Adv. Mater.* **2012,** *24* (38), 5166-5180.

26. Kang, K.; Meng, Y. S.; Bréger, J.; Grey, C. P.; Ceder, G., Electrodes with High Power and High Capacity for Rechargeable Lithium Batteries. *Science* **2006,** *311* (5763), 977-980.

27. Islam, M. S.; Fisher, C. A. J., Lithium and sodium battery cathode materials: computational insights into voltage, diffusion and nanostructural properties. *Chem. Soc. Rev.* **2014,** *43* (1), 185-204.

28. Lee, K. T.; Cho, J., Roles of nanosize in lithium reactive nanomaterials for lithium ion batteries. *Nano Today* **2011,** *6* (1), 28-41.

29. Malik, R.; Zhou, F.; Ceder, G., Kinetics of non-equilibrium lithium incorporation in LiFePO4. *Nat Mater* **2011,** *10* (8), 587-590.

30. Cogswell, D. A.; Bazant, M. Z., Coherency Strain and the Kinetics of Phase Separation in LiFePO4 Nanoparticles. *ACS Nano* **2012,** *6* (3), 2215-2225.

31. Lu, X.; Zhao, L.; He, X.; Xiao, R.; Gu, L.; Hu, Y.-S.; Li, H.; Wang, Z.; Duan, X.; Chen, L.; Maier, J.; Ikuhara, Y., Lithium Storage in Li4Ti5O12 Spinel: The Full Static Picture from Electron Microscopy. *Adv. Mater.* **2012,** *24* (24), 3233-3238.

32. Manthiram, A.; Chemelewski, K.; Lee, E.-S., A perspective on the high-voltage LiMn1.5Ni0.5O4 spinel cathode for lithium-ion batteries. *Energy Environ. Sci.* **2014,** *7* (4), 1339-1350.

33. Ulvestad, A.; Singer, A.; Cho, H.-M.; Clark, J. N.; Harder, R.; Maser, J.; Meng, Y. S.; Shpyrko, O. G., Single Particle Nanomechanics in Operando Batteries via Lensless Strain Mapping. *Nano Lett.* **2014,** *14* (9), 5123-5127.

34. Nitta, N.; Wu, F.; Lee, J. T.; Yushin, G., Li-ion battery materials: present and future. *Mater. Today* **2015,** *18* (5), 252-264.

35. Yang, J.; Winter, M.; Besenhard, J. O., Small particle size multiphase Li-alloy anodes for lithium-ionbatteries. *Solid State Ion.* **1996,** *90* (1–4), 281-287.

36. Badway, F.; Cosandey, F.; Pereira, N.; Amatucci, G. G., Carbon Metal Fluoride Nanocomposites: High-Capacity Reversible Metal Fluoride Conversion Materials as Rechargeable Positive Electrodes for Li Batteries. *J. Electrochem. Soc.* **2003,** *150* (10), A1318-A1327.

37. Martin, C. R., Nanomaterials: A Membrane-Based Synthetic Approach. *Science* **1994,** *266* (5193), 1961-1966.

38. Sides, C. R.; Martin, C. R., Nanomaterials in Li-Ion Battery Electrode Design. In *Modern Aspects of Electrochemistry No.40*, White, R. E.; Vayenas, C. G.; Gamboa-Aldeco, M. E., Eds. Springer: New York, **2007**; Chapter 3, p 75.

39. Bard, A. J.; Faulkner, L. R., *Electrochemical Methods: Fundamentals and Applications*. Wiley: **2000**.

40. Barsoukov, E.; Macdonald, J. R., *Impedance spectroscopy : theory, experiment, and applications*. 2nd ed.; Wiley-Interscience: Hoboken, N.J., **2005**.

41. Cullity, B. D., *Elements of X-ray diffraction*. Addison-Wesley Pub. Co.: **1956**.

42. Proffen, T.; Billinge, S. J. L.; Egami, T.; Louca, D., Structural analysis of complex materials using the atomic pair distribution function   a practical guide. *Z. Kristallogr.* **2003,** *218* (2-2003), 132-143.

43. Page, K.; Proffen, T.; Terrones, H.; Terrones, M.; Lee, L.; Yang, Y.; Stemmer, S.; Seshadri, R.; Cheetham, A. K., Direct observation of the structure of gold nanoparticles by total scattering powder neutron diffraction. *Chem. Phys. Lett.* **2004,** *393* (4–6), 385-388.

44. Ariyoshi, K.; Makimura, Y.; Ohzuku, T., Lithium Insertion Materials Having Spinel-Framework Structure for Advanced Batteries. In *Lithium Ion Rechargeable Batteries*, Wiley-VCH Verlag GmbH & Co. KGaA: **2010**, pp 11-38.

45. Song, J.; Shin, D. W.; Lu, Y.; Amos, C. D.; Manthiram, A.; Goodenough, J. B., Role of Oxygen Vacancies on the Performance of Li[Ni0.5–xMn1.5+x]O4 (x = 0, 0.05, and 0.08) Spinel Cathodes for Lithium-Ion Batteries. *Chem. Mat.* **2012,** *24* (15), 3101-3109.

46. Wang, L.; Li, H.; Huang, X.; Baudrin, E., A comparative study of Fd-3m and P4332 "LiNi0.5Mn1.5O4". *Solid State Ion.* **2011,** *193* (1), 32-38.

47. Cho, H. M.; Park, Y. J.; Shin, H. C., Semiempirical Analysis of Time-Dependent Elementary Polarizations in Electrochemical Cells. *J. Electrochem. Soc.* **2010,** *157* (1), A8-A18.

48. Cho, H. M.; Shin, H. C., Analysis of Cell Impedance for the Design of a High-Power Lithium-Ion Battery In *Lithium batteries research, technology, and applications*, Dahlin, G. R.; Strom, K. E., Eds. Nova Science Publishers: New York, **2010**, pp 73-118.

49. Cho, H. M.; Park, Y. J.; Yeon, J. W.; Shin, H. C., In-Depth Investigation on Two- and Three-Electrode Impedance Measurements in Terms of the Effect of the Counter Electrode. *Electron. Mater. Lett.* **2009,** *5* (4), 169-178.

50. Carroll, K. J.; Yang, M.-C.; Veith, G. M.; Dudney, N. J.; Meng, Y. S., Intrinsic Surface Stability in LiMn2–xNixO4–δ (x = 0.45, 0.5) High Voltage Spinel Materials for Lithium Ion Batteries. *Electrochem. Solid-State Lett.* **2012,** *15* (5), A72-A75.

51. Patrissi, C. J.; Martin, C. R., Sol-Gel-Based Template Synthesis and Li-Insertion Rate Performance of Nanostructured Vanadium Pentoxide. *J. Electrochem. Soc.* **1999,** *146* (9), 3176-3180.

52. Sides, C. R.; Croce, F.; Young, V. Y.; Martin, C. R.; Scrosati, B., A High-Rate, Nanocomposite LiFePO[sub 4]/Carbon Cathode. *Electrochem. Solid-State Lett.* **2005,** *8* (9), A484-A487.

53. Shaju, K. M.; Bruce, P. G., Nano-LiNi0.5Mn1.5O4 spinel: a high power electrode for Li-ion batteries. *Dalton Trans.* **2008,** (40), 5471-5475.

54. Shannon, R. D., Revised effective ionic radii and systematic studies of interatomic distances in halides and chalcogenides. *Acta Crystallogr. Sect. A* **1976,** *32* (5), 751-767.

55. Pyun, S.-I.; Bae, J.-S., The ac impedance study of electrochemical lithium intercalation into porous vanadium oxide electrode. *Electrochim. Acta* **1996,** *41* (6), 919-925.

56. Levi, M. D.; Aurbach, D., Simultaneous Measurements and Modeling of the Electrochemical Impedance and the Cyclic Voltammetric Characteristics of Graphite Electrodes Doped with Lithium. *J. Phys. Chem. B* **1997,** *101* (23), 4630-4640.

57. Levi, M. D.; Salitra, G.; Markovsky, B.; Teller, H.; Aurbach, D.; Heider, U.; Heider, L., Solid-state electrochemical kinetics of Li-ion intercalation into Li1-xCoO2: Simultaneous application of electroanalytical techniques SSCV, PITT, and EIS. *J. Electrochem. Soc.* **1999,** *146* (4), 1279-1289.

58. Aurbach, D., Review of selected electrode–solution interactions which determine the performance of Li and Li ion batteries. *J. Power Sources* **2000,** *89* (2), 206-218.

59. Aurbach, D., The Role of Surface Films on Electrodes in Li-Ion Batteries. In *Advances in Lithium-Ion Batteries*, Schalkwijk, W.; Scrosati, B., Eds. Springer US: **2002**, pp 7-77.

60. Aurbach, D.; Levi, M. D.; Gamulski, K.; Markovsky, B.; Salitra, G.; Levi, E.; Heider, U.; Heider, L.; Oesten, R., Capacity fading of LixMn2O4 spinel electrodes studied by XRD and electroanalytical techniques. *J. Power Sources* **1999,** *81–82* (0), 472-479.

61. Aurbach, D.; Levi, M. D.; Levi, E.; Teller, H.; Markovsky, B.; Salitra, G.; Heider, U.; Heider, L., Common Electroanalytical Behavior of Li Intercalation Processes into Graphite and Transition Metal Oxides. *J. Electrochem. Soc.* **1998,** *145* (9), 3024-3034.

62. Shin, H.-C.; Liu, M., Preparation of Hierarchical (Nano/Meso/Macro) Porous Structures Using Electrochemical Deposition. In *Progress in Corrosion Science and Engineering II*, Pyun, S.-I.; Lee, J.-W., Eds. Springer: New York, **2012**; Chapter 4, p 297.

63. Pitchai, R.; Thavasi, V.; Mhaisalkar, S. G.; Ramakrishna, S., Nanostructured cathode materials: a key for better performance in Li-ion batteries. *J. Mater. Chem.* **2011,** *21* (30), 11040-11051.

64. Goodenough, J. B.; Kim, Y., Challenges for Rechargeable Li Batteries†. *Chem. Mat.* **2010,** *22* (3), 587-603.

65. Hagh, N. M.; Cosandey, F.; Rangan, S.; Bartynski, R.; Amatucci, G. G., Electrochemical Performance of Acid-Treated Nanostructured LiMn1.5Ni0.5O4−δ Spinel at Elevated Temperature. *J. Electrochem. Soc.* **2010,** *157* (3), A305-A319.

66. Zhong, G. B.; Wang, Y. Y.; Yu, Y. Q.; Chen, C. H., Electrochemical investigations of the LiNi0.45M0.10Mn1.45O4 (M = Fe, Co, Cr) 5V cathode materials for lithium ion batteries. *J. Power Sources* **2012,** *205* (0), 385-393.

67. Weppner, W.; Huggins, R. A., Determination of the Kinetic Parameters of Mixed-Conducting Electrodes and Application to the System Li[sub 3]Sb. *J. Electrochem. Soc.* **1977,** *124* (10), 1569-1578.

68. Markevich, E.; Levi, M. D.; Aurbach, D., Comparison between potentiostatic and galvanostatic intermittent titration techniques for determination of chemical diffusion coefficients in ion-insertion electrodes. *J. Electroanal. Chem.* **2005,** *580* (2), 231-237.

69. Lee, J.-W.; Park, S.-J.; Choi, W.-S.; Shin, H.-C., Well-defined meso- to macro-porous film of tin oxides formed by an anodization process. *Electrochim. Acta* **2011,** *56* (17), 5919-5925.

70. Jung, H.-R.; Kim, E.-J.; Park, Y. J.; Shin, H.-C., Nickel-tin foam with nanostructured walls for rechargeable lithium battery. *J. Power Sources* **2011,** *196* (11), 5122-5127.

71. Liu, H.; Cho, H.-M.; Meng, Y. S.; Li, Q., Engineering Three-Dimensionally Electrodeposited Si-on-Ni Inverse Opal Structure for High Volumetric Capacity Li-Ion Microbattery Anode. *ACS Appl. Mater. Interfaces* **2014,** *6* (12), 9842-9849.

72. Wang, L.; He, X.; Sun, W.; Wang, J.; Li, Y.; Fan, S., Crystal Orientation Tuning of LiFePO4 Nanoplates for High Rate Lithium Battery Cathode Materials. *Nano Lett.* **2012,** *12* (11), 5632-5636.

73. Wang, J.; Yang, J.; Tang, Y.; Li, R.; Liang, G.; Sham, T.-K.; Sun, X., Surface aging at olivine LiFePO4: a direct visual observation of iron dissolution and the protection role of nano-carbon coating. *J. Mater. Chem. A* **2013,** *1* (5), 1579-1586.

74. Hao, X.; Bartlett, B. M., Improving the Electrochemical Stability of the High-Voltage Li-Ion Battery Cathode LiNi0.5Mn1.5O4 by Titanate-Based Surface Modification. *J. Electrochem. Soc.* **2013,** *160* (5), A3162-A3170.

75. Cheng, H.-M.; Wang, F.-M.; Chu, J. P.; Santhanam, R.; Rick, J.; Lo, S.-C., Enhanced Cycleabity in Lithium Ion Batteries: Resulting from Atomic Layer Depostion of Al2O3 or TiO2 on LiCoO2 Electrodes. *J. Phys. Chem. C* **2012,** *116* (14), 7629-7637.

76. Deng, H.; Nie, P.; Luo, H.; Zhang, Y.; Wang, J.; Zhang, X., Highly enhanced lithium storage capability of LiNi0.5Mn1.5O4 by coating with Li2TiO3 for Li-ion batteries. *J. Mater. Chem. A* **2014,** *2* (43), 18256-18262.

77. Konishi, H.; Suzuki, K.; Taminato, S.; Kim, K.; Zheng, Y.; Kim, S.; Lim, J.; Hirayama, M.; Son, J.-Y.; Cui, Y.; Kanno, R., Effect of surface Li3PO4 coating on LiNi0.5Mn1.5O4 epitaxial thin film electrodes synthesized by pulsed laser deposition. *J. Power Sources* **2014,** *269* (0), 293-298.

78. Li, X.; Guo, W.; Liu, Y.; He, W.; Xiao, Z., Spinel LiNi0.5Mn1.5O4 as superior electrode materials for lithium-ion batteries: Ionic liquid assisted synthesis and the effect of CuO coating. *Electrochim. Acta* **2014,** *116* (0), 278-283.

79. Song, J.; Han, X.; Gaskell, K.; Xu, K.; Lee, S.; Hu, L., Enhanced electrochemical stability of high-voltage LiNi0.5Mn1.5O4 cathode by surface modification using atomic layer deposition. *J Nanopart Res* **2014,** *16* (11), 1-8.

80. Xiao, X.; Ahn, D.; Liu, Z.; Kim, J.-H.; Lu, P., Atomic layer coating to mitigate capacity fading associated with manganese dissolution in lithium ion batteries. *Electrochem. Commun.* **2013,** *32* (0), 31-34.

81. Park, J. S.; Meng, X.; Elam, J. W.; Hao, S.; Wolverton, C.; Kim, C.; Cabana, J., Ultrathin Lithium-Ion Conducting Coatings for Increased Interfacial Stability in High Voltage Lithium-Ion Batteries. *Chem. Mat.* **2014,** *26* (10), 3128-3134.

82. Zhang, Q.; Mei, J.; Wang, X.; Tang, F.; Fan, W.; Lu, W., High performance spinel LiNi0.5Mn1.5O4 cathode material by lithium polyacrylate coating for lithium ion battery. *Electrochim. Acta* **2014,** *143* (0), 265-271.

83. Gao, X.-W.; Deng, Y.-F.; Wexler, D.; Chen, G.-H.; Chou, S.-L.; Liu, H.-K.; Shi, Z.-C.; Wang, J.-Z., Improving the electrochemical performance of the LiNi0.5Mn1.5O4 spinel by polypyrrole coating as a cathode material for the lithium-ion battery. *J. Mater. Chem. A* **2015,** *3* (1), 404-411.

84. Niketic, S.; Couillard, M.; MacNeil, D.; Abu-Lebdeh, Y., Improving the performance of high voltage LiMn1.5Ni0.5O4 cathode material by carbon coating. *J. Power Sources* **2014,** *271* (0), 285-290.

85. Kim, J. W.; Travis, J. J.; Hu, E.; Nam, K.-W.; Kim, S. C.; Kang, C. S.; Woo, J.-H.; Yang, X.-Q.; George, S. M.; Oh, K. H.; Cho, S.-J.; Lee, S.-H., Unexpected high power performance of atomic layer deposition coated Li[Ni1/3Mn1/3Co1/3]O2 cathodes. *J. Power Sources* **2014,** *254* (0), 190-197.

86. Ban, C.; Xie, M.; Sun, X.; Travis, J. J.; Wang, G.; Sun, H.; Dillon, A. C.; Lian, J.; George, S. M., Atomic layer deposition of amorphous TiO 2 on graphene as an anode for Li-ion batteries. *Nanotechnology* **2013,** *24* (42), 424002.

87. Nguyen, H. T.; Zamfir, M. R.; Duong, L. D.; Lee, Y. H.; Bondavalli, P.; Pribat, D., Alumina-coated silicon-based nanowire arrays for high quality Li-ion battery anodes. *J. Mater. Chem.* **2012,** *22* (47), 24618-24626.

88. Marichy, C.; Bechelany, M.; Pinna, N., Atomic Layer Deposition of Nanostructured Materials for Energy and Environmental Applications. *Adv. Mater.* **2012,** *24* (8), 1017-1032.

89. Scott, I. D.; Jung, Y. S.; Cavanagh, A. S.; Yan, Y.; Dillon, A. C.; George, S. M.; Lee, S.-H., Ultrathin Coatings on Nano-LiCoO2 for Li-Ion Vehicular Applications. *Nano Lett.* **2010,** *11* (2), 414-418.

90. Dunn, B.; Liu, P.; Meng, S., Nanoscience and nanotechnology in next generation lithium batteries *. *Nanotechnology* **2013,** *24* (42), 420201.

91.   Cho, H.-M.; Meng, Y. S., Effect of Ni/Mn Ordering on Elementary Polarizations of LiNi0.5Mn1.5O4 Spinel and Its Nanostructured Electrode. *J. Electrochem. Soc.* **2013,** *160* (9), A1482-A1488.

92.   Liu, D.; Zhu, W.; Trottier, J.; Gagnon, C.; Barray, F.; Guerfi, A.; Mauger, A.; Groult, H.; Julien, C. M.; Goodenough, J. B.; Zaghib, K., Spinel materials for high-voltage cathodes in Li-ion batteries. *RSC Adv.* **2014,** *4* (1), 154-167.

93.   Liu, J.; Manthiram, A., Understanding the Improved Electrochemical Performances of Fe-Substituted 5 V Spinel Cathode LiMn1.5Ni0.5O4. *J. Phys. Chem. C* **2009,** *113* (33), 15073-15079.

94.   Sun, Y.; Yang, Y.; Zhan, H.; Shao, H.; Zhou, Y., Synthesis of high power type LiMn1.5Ni0.5O4 by optimizing its preparation conditions. *J. Power Sources* **2010,** *195* (13), 4322-4326.

95.   Lin, M.; Ben, L.; Sun, Y.; Wang, H.; Yang, Z.; Gu, L.; Yu, X.; Yang, X.-Q.; Zhao, H.; Yu, R.; Armand, M.; Huang, X., Insight into the Atomic Structure of High-Voltage Spinel LiNi0.5Mn1.5O4 Cathode Material in the First Cycle. *Chem. Mat.* **2014,** *27* (1), 292-303.

96.   Knez, M.; Nielsch, K.; Niinistö, L., Synthesis and Surface Engineering of Complex Nanostructures by Atomic Layer Deposition. *Adv. Mater.* **2007,** *19* (21), 3425-3438.

97.   Liu, Y.; Hudak, N. S.; Huber, D. L.; Limmer, S. J.; Sullivan, J. P.; Huang, J. Y., In Situ Transmission Electron Microscopy Observation of Pulverization of Aluminum Nanowires and Evolution of the Thin Surface Al2O3 Layers during Lithiation–Delithiation Cycles. *Nano Lett.* **2011,** *11* (10), 4188-4194.

98.   Huang, Q.-A.; Hui, R.; Wang, B.; Zhang, J., A review of AC impedance modeling and validation in SOFC diagnosis. *Electrochim. Acta* **2007,** *52* (28), 8144-8164.

99.   Schichlein, H.; Müller, A. C.; Voigts, M.; Krügel, A.; Ivers-Tiffée, E., Deconvolution of electrochemical impedance spectra for the identification of electrode reaction mechanisms in solid oxide fuel cells. *J. Appl. Electrochem.* **2002,** *32* (8), 875-882.

100.   Santhanam, R.; Rambabu, B., Research progress in high voltage spinel LiNi0.5Mn1.5O4 material. *J. Power Sources* **2010,** *195* (17), 5442-5451.

101.   Larcher, D.; Patrice, R., Preparation of Metallic Powders and Alloys in Polyol Media: A Thermodynamic Approach. *J. Solid State Chem.* **2000,** *154* (2), 405-411.

102.   Poul, L.; Ammar, S.; Jouini, N.; Fievet, F.; Villain, F., Synthesis of Inorganic Compounds (Metal, Oxide and Hydroxide) in Polyol Medium: A Versatile Route Related to the Sol-Gel Process. *J. Sol-Gel Sci. Technol.* **2003,** *26* (1-3), 261-265.

103.   Yoon, H.; Xu, A.; Sterbinsky, G. E.; Arena, D. A.; Wang, Z.; Stephens, P. W.; Meng, Y. S.; Carroll, K. J., In situ non-aqueous nucleation and growth of next generation rare-earth-free permanent magnets. *Phys. Chem. Chem. Phys.* **2015,** *17* (2), 1070-1076.

104. Wang, Z. L.; Yin, J. S.; Jiang, Y. D., EELS analysis of cation valence states and oxygen vacancies in magnetic oxides. *Micron* **2000,** *31* (5), 571-580.

105. Carroll, K. J.; Qian, D.; Fell, C.; Calvin, S.; Veith, G. M.; Chi, M.; Baggetto, L.; Meng, Y. S., Probing the electrode/electrolyte interface in the lithium excess layered oxide Li1.2Ni0.2Mn0.6O2. *Phys. Chem. Chem. Phys.* **2013,** *15* (26), 11128-11138.

106. Ravel, B.; Newville, M., ATHENA, ARTEMIS, HEPHAESTUS: data analysis for X-ray absorption spectroscopy using IFEFFIT. *J. Synchrotron Radiat.* **2005,** *12* (4), 537-541.

107. Wang, Z. L.; Yin, J. S.; Mo, W. D.; Zhang, Z. J., In-Situ Analysis of Valence Conversion in Transition Metal Oxides Using Electron Energy-Loss Spectroscopy. *J. Phys. Chem. B* **1997,** *101* (35), 6793-6798.

108. Kurata, H.; Lefèvre, E.; Colliex, C.; Brydson, R., Electron-energy-loss near-edge structures in the oxygen K-edge spectra of transition-metal oxides. *Phys. Rev. B* **1993,** *47* (20), 13763-13768.

109. Xu, B.; Fell, C. R.; Chi, M.; Meng, Y. S., Identifying surface structural changes in layered Li-excess nickel manganese oxides in high voltage lithium ion batteries: A joint experimental and theoretical study. *Energy Environ. Sci.* **2011,** *4* (6), 2223-2233.

110. Karim, A.; Fosse, S.; Persson, K. A., Surface structure and equilibrium particle shape of the LiMn2O4 spinel from first-principles calculations. *Phys. Rev. B* **2013,** *87* (7), 075322.

111. Schroeder, S. L. M., Towards a 'universal curve' for total electron-yield XAS. *Solid State Commun.* **1996,** *98* (5), 405-409.

112. Abbate, M.; Goedkoop, J. B.; de Groot, F. M. F.; Grioni, M.; Fuggle, J. C.; Hofmann, S.; Petersen, H.; Sacchi, M., Probing depth of soft x-ray absorption spectroscopy measured in total-electron-yield mode. *Surf. Interface Anal.* **1992,** *18* (1), 65-69.

113. Farrow, C. L.; Juhas, P.; Liu, J. W.; Bryndin, D.; Božin, E. S.; Bloch, J.; Proffen, T.; Billinge, S. J. L., PDFfit2 and PDFgui: computer programs for studying nanostructure in crystals. *J. Phys.: Condens. Matter* **2007,** *19* (33), 335219.

114. Qiu, X.; Thompson, J. W.; Billinge, S. J. L., PDFgetX2: a GUI-driven program to obtain the pair distribution function from X-ray powder diffraction data. *J. Appl. Crystallogr.* **2004,** *37* (4), 678.

115. Wiaderek, K. M.; Borkiewicz, O. J.; Castillo-Martínez, E.; Robert, R.; Pereira, N.; Amatucci, G. G.; Grey, C. P.; Chupas, P. J.; Chapman, K. W., Comprehensive Insights into the Structural and Chemical Changes in Mixed-Anion FeOF Electrodes by Using Operando PDF and NMR Spectroscopy. *J. Am. Chem. Soc.* **2013,** *135* (10), 4070-4078.

116. Key, B.; Morcrette, M.; Tarascon, J.-M.; Grey, C. P., Pair Distribution Function Analysis and Solid State NMR Studies of Silicon Electrodes for Lithium Ion Batteries: Understanding the (De)lithiation Mechanisms. *J. Am. Chem. Soc.* **2011,** *133* (3), 503-512.

117. Hua, X.; Robert, R.; Du, L.-S.; Wiaderek, K. M.; Leskes, M.; Chapman, K. W.; Chupas, P. J.; Grey, C. P., Comprehensive Study of the CuF2 Conversion Reaction Mechanism in a Lithium Ion Battery. *J. Phys. Chem. C* **2014,** *118* (28), 15169-15184.

118. Débart, A.; Paterson, A. J.; Bao, J.; Bruce, P. G., α-MnO2 Nanowires: A Catalyst for the O2 Electrode in Rechargeable Lithium Batteries. *Angew. Chem. Int. Ed.* **2008,** *47* (24), 4521-4524.

119. Lu, Y.-C.; Xu, Z.; Gasteiger, H. A.; Chen, S.; Hamad-Schifferli, K.; Shao-Horn, Y., Platinum−Gold Nanoparticles: A Highly Active Bifunctional Electrocatalyst for Rechargeable Lithium−Air Batteries. *J. Am. Chem. Soc.* **2010,** *132* (35), 12170-12171.

120. Ji, X.; Lee, K. T.; Nazar, L. F., A highly ordered nanostructured carbon-sulphur cathode for lithium-sulphur batteries. *Nat Mater* **2009,** *8* (6), 500-506.

121. Yang, Y.; McDowell, M. T.; Jackson, A.; Cha, J. J.; Hong, S. S.; Cui, Y., New Nanostructured Li2S/Silicon Rechargeable Battery with High Specific Energy. *Nano Lett.* **2010,** *10* (4), 1486-1491.